RESEARCH ARTICLE SUMMARY

STRUCTURAL BIOLOGY

The endoplasmic reticulum P5A-ATPase is a transmembrane helix dislocase

Michael J. McKenna*, Sue Im Sim, Alban Ordureau, Lianjie Wei, J. Wade Harper, Sichen Shao†, Eunyong Park†

INTRODUCTION: Eukaryotic cells contain membrane-bound organelles with distinct identities and functionalities that depend on protein composition. Correct localization of proteins is thus critical for organelle function and cellular homeostasis. The endoplasmic reticulum (ER) and mitochondrial outer membrane are the primary destinations for newly synthesized proteins with hydrophobic transmembrane segments (TMs). Membrane protein localization requires not only high-fidelity protein targeting but also quality control mechanisms that selectively remove mislocalized proteins. At the mitochondrial outer membrane, the ATP-dependent motor protein Msp1/ATAD1 removes some mislocalized transmembrane proteins. By contrast, although protein targeting to the ER is well studied, the mechanisms that remove mistargeted transmembrane proteins from the ER membrane are incompletely understood.

RATIONALE: As a model to study membrane protein localization, we focused on tail–anchored proteins, which contain a single C-terminal TM that is necessary and largely sufficient for organelle localization. We reasoned that factors that mediate mitochondrial tail–anchored protein localization would interact directly with nascent proteins. We used an unbiased, site-specific cross-linking and mass spectrometry approach to identify such protein TMs. This approach revealed that the ER-resident orphan P-type pump P5A-ATPase (Spf1 in yeast; ATP13A1 in humans) interacted directly with a mitochondrial tail–anchored protein. Because genetic studies have linked the P5A-ATPase to mitochondrial tail–anchored protein mislocalization, we combined biochemical and structural approaches to define the function and mechanism of the P5A-ATPase.

RESULTS: P-type ATPases form a large class of active transporters that are present in all kingdoms of life and predominantly transport ions or lipids across cellular membranes. The P5A-ATPase belongs to a eukaryotic-specific subfamily of P-type ATPases with unknown substrate specificity. We reconstituted membrane protein insertion into organelles in a cell-free system and used site-specific cross-linking to reveal that the P5A-ATPase interacts directly with the TM of a mitochondrial tail–anchored protein. Human cells lacking ATP13A1 showed mislocalization of mitochondrial tail–anchored proteins to the ER and secretory pathway. In in vitro assays, newly synthesized mitochondrial tail–anchored proteins aberrantly accumulated in ER vesicles lacking P5A-ATPase activity. This accumulation was due to the impaired extraction of misinserted mitochondrial proteins from ER membranes lacking ATP13A1. Cryo–electron microscopy structures of *Saccharomyces cerevisiae* Spf1 in different conformations at 3.3 to 3.7 Å resolutions revealed that the P5A-ATPase has an atypically large substrate-binding pocket compared with other P-type ATPases with known structures. The pocket alternately opens toward the ER lumen and cytosol while remaining accessible to the lipid bilayer through a lateral opening. Trapping putative substrates for structure determination revealed an additional membrane-spanning density at the lateral opening, which resembles an α-helical TM. Together with proteomics of wild-type and P5A-ATPase knock-out cells, our results indicate that the P5A-ATPase can dislocate moderately hydrophobic TMs with short hydrophilic lumenal domains that misinsert into the ER.

CONCLUSION: Our findings define the function of the P5A-ATPase as a dislocase of TMs at the ER membrane. This assignment establishes polypeptides as P-type ATPase transport substrates in addition to ions and lipids. Active dislocation of misinserted proteins from the ER by the P5A-ATPase also represents a previously unknown cellular safeguarding and quality control mechanism that helps maintain ER and mitochondrial homeostasis, possibly explaining the pleiotropic phenotypes linked to P5A-ATPase dysfunction. ■

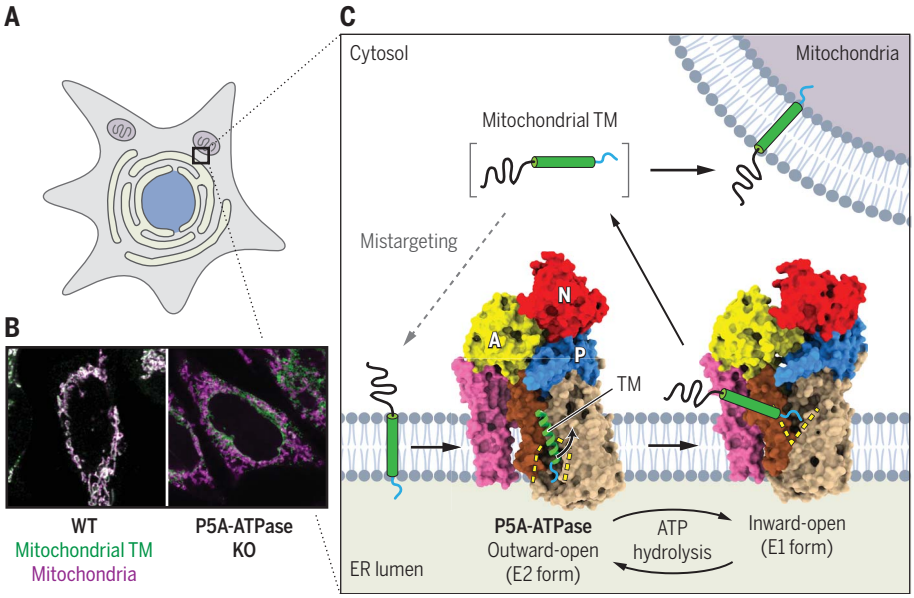

P5A-ATPase dislocates mistargeted TMs from the ER. (**A**) Diagram of a eukaryotic cell showing the nucleus (blue), ER (pale green), and mitochondria (pale purple). (**B**) Immunofluorescence images showing mislocalization of a mitochondrial tail–anchored protein containing the mitochondrial TM OMP25 (green) in P5A-ATPase knock-out cells. A mitochondrial marker (TOM20) is shown in purple. (**C**) Model for P5A-ATPase–mediated removal of mistargeted TMs from the ER membrane based on cryo–electron microscopy structures showing different conformations of the yeast P5A-ATPase (Spf1; surface representations) and the position of a substrate TM (green ribbon) bound to the outward-open form.

The list of author affiliations is available in the full article online.
*These authors contributed equally to this work.
†Corresponding author. E-mail: sichen_shao@hms.harvard.edu (S.S.); eunyong_park@berkeley.edu (E.P.)
Cite this article as M. J. McKenna *et al.*, *Science* 369, eabc5809 (2020). DOI: 10.1126/science.abc5809

S READ THE FULL ARTICLE AT
https://doi.org/10.1126/science.abc5809

RESEARCH ARTICLE

STRUCTURAL BIOLOGY

The endoplasmic reticulum P5A-ATPase is a transmembrane helix dislocase

Michael J. McKenna[1]*, Sue Im Sim[2]*, Alban Ordureau[1], Lianjie Wei[1]†, J. Wade Harper[1], Sichen Shao[1]‡, Eunyong Park[2,3]‡

Organelle identity depends on protein composition. How mistargeted proteins are selectively recognized and removed from organelles is incompletely understood. Here, we found that the orphan P5A–adenosine triphosphatase (ATPase) transporter ATP13A1 (Spf1 in yeast) directly interacted with the transmembrane segment (TM) of mitochondrial tail–anchored proteins. P5A-ATPase activity mediated the extraction of mistargeted proteins from the endoplasmic reticulum (ER). Cryo–electron microscopy structures of *Saccharomyces cerevisiae* Spf1 revealed a large, membrane-accessible substrate-binding pocket that alternately faced the ER lumen and cytosol and an endogenous substrate resembling an α-helical TM. Our results indicate that the P5A-ATPase could dislocate misinserted hydrophobic helices flanked by short basic segments from the ER. TM dislocation by the P5A-ATPase establishes an additional class of P-type ATPase substrates and may correct mistakes in protein targeting or topogenesis.

More than one-third of the proteome in eukaryotes consists of membrane and secretory proteins with diverse hydrophobic sequences that must insert correctly into the appropriate cellular membrane. Protein mistargeting causes organelle dysfunction and cellular and organismal stress (*1*, *2*), underscoring the importance of quality control (QC) mechanisms that remove mislocalized proteins. Defined by a single C-terminal transmembrane segment (TM), tail-anchored (TA) proteins pose a distinct sorting challenge because they rely exclusively on post-translational mechanisms to localize to the endoplasmic reticulum (ER), mitochondria, or peroxisomes. Although TA protein targeting to the ER is well studied (*3*), how cells remove mistargeted TA proteins from the ER and properly localize non-ER TA proteins is poorly understood.

A yeast genetic screen for mutants that disrupt mitochondrial TA protein localization identified only *SPF1*, the deletion of which results in mitochondrial TA protein accumulation at the ER (*4*). *SPF1* encodes the ER-resident orphan P5A–adenosine triphosphatase (ATPase), a conserved subtype of the eukaryotic-specific P5 subfamily of P-type ATPases. P-type ATPases are a major class of active transporters found in all organisms that pump substrates across membranes through conformational changes driven by phosphorylation and dephosphorylation of a conserved aspartate (*5*–*7*). Among the five subfamilies categorized by sequence similarity, the functions of P1- to P3-ATPases as cation transporters and P4-ATPases as lipid flippases are well defined. In addition, ATP13A2, one of four mammalian P5B-ATPases, was recently proposed to be a lysosomal polyamine transporter (*8*). Otherwise, little is known about the substrates and biological functions of P5-ATPases.

Humans and yeast each have a single P5A-ATPase, ATP13A1 and Spf1, respectively, which likely perform a conserved task based on functional complementation (*9*, *10*). In addition to disrupting TA protein localization and turnover (*4*, *11*), mutating *SPF1* causes a wide spectrum of phenotypes, including induction of the ER unfolded protein response, defects in lipid and sterol homeostasis, and dysregulated protein N-glycosylation, topogenesis, and turnover (*10*, *12*–*20*). It has been speculated that these pleiotropic phenotypes may be explained by the P5A-ATPase functioning as a manganese or calcium transporter or as a lipid flippase (*13*–*15*, *18*, *21*). However, direct evidence supporting any of these functions is lacking, and the identity of physiological P5A-ATPase substrates remains elusive. Here, using cell-free reconstitutions, high-resolution cryo–electron microscopy (cryo-EM), and proteomics, we found that the P5A-ATPase could dislocate moderately hydrophobic terminal transmembrane helices from the ER membrane, a mechanism required to ensure correct mitochondrial TA protein localization.

The P5A-ATPase interact directly with TMs

We used an unbiased strategy to identify factors that interacted directly with a model TA protein containing the mitochondrial OMP25 TM during reconstituted targeting reactions (Fig. 1A). We incorporated the ultraviolet (UV) light–activated cross-linker p-benzoyl-L-phenylalanine (Bpa) into the TM [referred to as TA(Bpa)] and purified recombinant, FLAG-tagged TA(Bpa) in complex with calmodulin (CaM), a calcium-dependent TM chaperone (fig. S1A) (*22*, *23*). We confirmed that FLAG-TA(Bpa) released from CaM by EGTA formed UV-dependent cross-links to the TM chaperone SGTA (*24*) (Fig. 1B and fig. S1C). When we released FLAG-TA(Bpa) in the presence of crude yeast membranes that could reconstitute TM insertion (fig. S1B), we observed cross-links to various proteins. Because photo-cross-linking generates covalent adducts, we expected this approach to enrich for otherwise transient interactions made by substrates undergoing targeting or QC. Indeed, tandem mass tag mass spectrometry (TMT-MS) analysis of UV-dependent membrane interactors of FLAG-TA(Bpa) identified known mitochondrial protein receptors and QC factors (Fig. 1C, fig. S1D, and data S1) (*25*–*27*). Unexpectedly, the ER-resident P5A-ATPase Spf1 was a prominent UV-dependent interactor of FLAG-TA(Bpa) (Fig. 1, C and D).

Although Spf1 has been linked to mitochondrial TA protein mislocalization (*4*, *11*), a direct interaction has not been reported. To confirm the interaction between the P5A-ATPase and TA proteins, we translated radiolabeled TA(Bpa) in vitro and performed site-specific cross-linking with crude yeast membranes or human ER-derived rough microsomes (RMs) containing FLAG-tagged Spf1 or ATP13A1, respectively. UV-dependent TA protein cross-links to each P5A-ATPase were detected after denaturing immunoprecipitations (Fig. 1E and fig. S2). Cross-linking was specific to Bpa positioned within the TM, but not the cytosolic domain, and was enhanced by flanking C-terminal sequences that contain basic residues (Fig. 1E), a common feature of mitochondrial TA proteins. Thus, the P5A-ATPase interacts directly with TMs.

ATP13A1 mediates ATP-dependent TM dislocation

To investigate whether P5A-ATPase activity affected TA protein localization to the ER, we performed in vitro insertion reactions of radiolabeled TA protein with RMs isolated from wild-type (WT) or ATP13A1 knock-out (KO) cells without or with reexpression of ATP13A1 (fig. S3A). TA protein containing the OMP25 TM preferentially accumulated in RMs lacking WT ATP13A1 activity (fig. S3, B to D). Two possibilities may explain this result: deleting ATP13A1 may enhance TM insertion (*4*) or it may impair TM extraction. To distinguish between these scenarios, we uncoupled OMP25 TM insertion and extraction by reisolating RMs

[1]Department of Cell Biology, Blavatnik Institute, Harvard Medical School, Boston, MA 02115, USA. [2]Department of Molecular and Cell Biology, University of California, Berkeley, CA 94720, USA. [3]California Institute for Quantitative Biosciences, University of California, Berkeley, CA 94720, USA.
*These authors contributed equally to this work.
†Present address: Biochemistry, Biophysics, and Structural Biology Program, Division of Biology and Biomedical Sciences, Washington University in St. Louis, St. Louis, MO 63110, USA.
‡Corresponding author. E-mail: sichen_shao@hms.harvard.edu (S.S.); eunyong_park@berkeley.edu (E.P.)

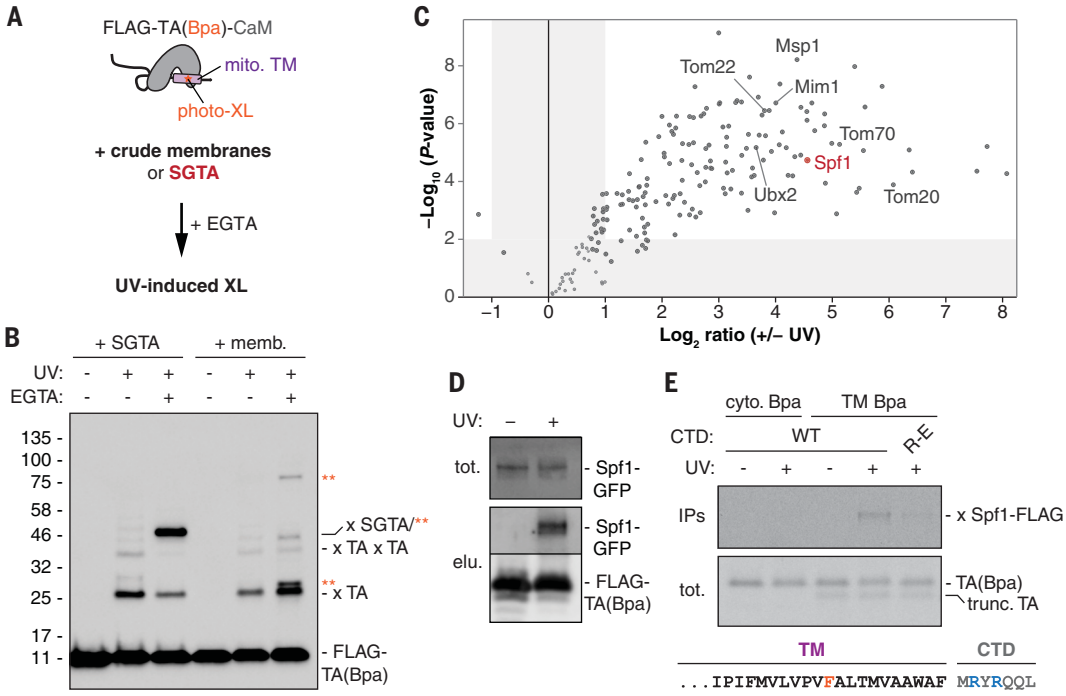

Fig. 1. The P5A-ATPase directly interacts with the TM of TA proteins. (**A**) Scheme to identify direct interactors of a mitochondrial TA protein. Recombinant FLAG-tagged TA protein with the OMP25 TM containing the UV-reactive cross-linker (photo-XL) Bpa was purified in complex with CaM [FLAG-TA(Bpa)-CaM]. EGTA dissociates FLAG-TA(Bpa) from CaM, permitting TM insertion into organelles in a crude membrane fraction or association with purified SGTA. Exposure to UV light induces site-specific covalent cross-links. (**B**) Anti-FLAG blots of reactions as in (A). Unmodified FLAG-TA(Bpa) and FLAG-TA(Bpa) cross-links of oligomers (x TA) and to SGTA (x SGTA) or membrane-specific proteins (orange asterisks) are indicated. (**C**) Six replicates of reactions as in (A) without or with UV irradiation were affinity purified and analyzed by TMT-MS. Volcano plot shows relation of the *P* value and $\log_2$ enrichment of proteins by UV irradiation. (**D**) Five percent input (tot.) of reactions as in (A) with organelles containing Spf1-GFP were purified by FLAG-TA(Bpa) (elu.) and immunoblotted for GFP to show UV-dependent Spf1 interaction. (**E**) Autoradiography of total (tot.) and denaturing anti-FLAG immunoprecipitations (IPs; top) of photo-cross-linking reactions of IVT-radiolabeled untagged TA(Bpa) with organelles containing Spf1-FLAG. OMP25 TM and C-terminal domain (CTD) sequence is below. Bpa is positioned in the cytosolic (cyto.) domain (lanes 1 and 2) or the OMP25 TM (lanes 3 to 5). R-E, TA(Bpa) in which the arginines in the OMP25 CTD are mutated to glutamates; trunc. TA, truncated translation products that do not incorporate Bpa.

after short insertion reactions for extraction assays with an energy-regenerating system and excess SGTA to sequester dislocated TMs (Fig. 2A) (*28*). WT RMs displayed higher extraction activity than KO RMs based on the amount of TA protein dislocated into the soluble fraction and bound to SGTA (Fig. 2, B and C, and fig. S4A). TM removal required ATP (fig. S4B), and the impaired dislocation activity of KO RMs was rescued by WT ATP13A1, but not D533A ATP13A1, a catalytically inactive variant in which the conserved phosphorylation site required for transport is mutated. Thus, ATP13A1 mediates ATP-dependent removal of a mitochondrial TM from the ER.

ATP13A1 minimizes TA protein mislocalization

We next investigated how ATP13A1 affects TA protein localization in human cells. In WT cells, FLAG-tagged mitochondrial TA protein reporters containing either the OMP25 or BAK1 TM (referred to as OMP25 or BAK1, respectively) localized to mitochondria as expected (Fig. 2, D and E, and fig. S5, A and B). Knocking out ATP13A1 resulted in substrate-specific changes in TA protein levels: OMP25 levels decreased and BAK1 levels increased (fig. S5, C and D). Both mitochondrial TA proteins displayed increased mislocalization to the ER and other secretory pathway organelles in ATP13A1 KO cells (Fig. 2D and figs. S5 and S6), consistent with *spf1*Δ yeast phenotypes (*4*, *11*). Localization of TA proteins with ER-targeted TMs was not affected by ATP13A1 KO (fig. S6). Reexpressing WT ATP13A1, but not D533A ATP13A1, in KO cells restored localization and expression levels of both OMP25 and BAK1 (Fig. 2, D and E, and fig. S5). Thus, ATP13A1 is required for proper mitochondrial TA protein localization.

To confirm that mitochondrial TA protein mislocalization in ATP13A1 KO cells was due to impaired TM removal from the ER rather than altered insertion efficiencies, we assayed the targeting of in vitro–translated (IVT) OMP25 to organelles of semipermeabilized cells over short time periods to minimize downstream processes (fig. S7A). OMP25 localized similarly to mitochondria in both WT and KO semipermeabilized cells (fig. S7, B and C), indicating that ATP13A1 was not required for initial TA protein targeting. Nonetheless, at steady state, mitochondrial TA proteins were not only mislocalized, but were also apparently depleted from mitochondria in ATP13A1 KO cells (Fig. 2D and figs. S5A and S7C). Because targeting to mitochondria was not affected, we reasoned that this observation may have resulted from other mechanisms. In particular, the AAA-ATPase Msp1 (ATAD1 in humans) can extract TMs from the outer mitochondrial membrane (*26*, *28*, *29*). Knocking down ATAD1 in ATP13A1 KO cells significantly restored mitochondrial localization of both BAK1 and OMP25 (fig. S8, A to C). These results support a model in which ATAD1 and ATP13A1 each facilitates TM removal from mitochondria and the ER, respectively, to contribute to TA protein localization at steady state (fig. S8D). Impairing ATP13A1 would result in the ER acting as a "sink" that accumulates misinserted TMs because of the disruption of a major mechanism for removing them. In the absence of ATP13A1, misinserted TA proteins appear to undergo alternative substrate-specific processes that may include vesicular trafficking and lysosomal or ER-associated degradation (*11*, *30*).

Features of ATP13A1-dependent proteins

The observation that reexpressing WT ATP13A1 in KO cells restored mitochondrial TA protein reporter levels suggested that some endogenous proteins that require ATP13A1 function could be identified by quantitative proteomics. To investigate this, we analyzed lysates of WT, ATP13A1 KO, and rescue cells using TMT-MS (fig. S9A and data S2). We identified 34 proteins with decreased abundance in ATP13A1 KO cells, the abundance of which was specifically rescued by acutely reexpressing WT

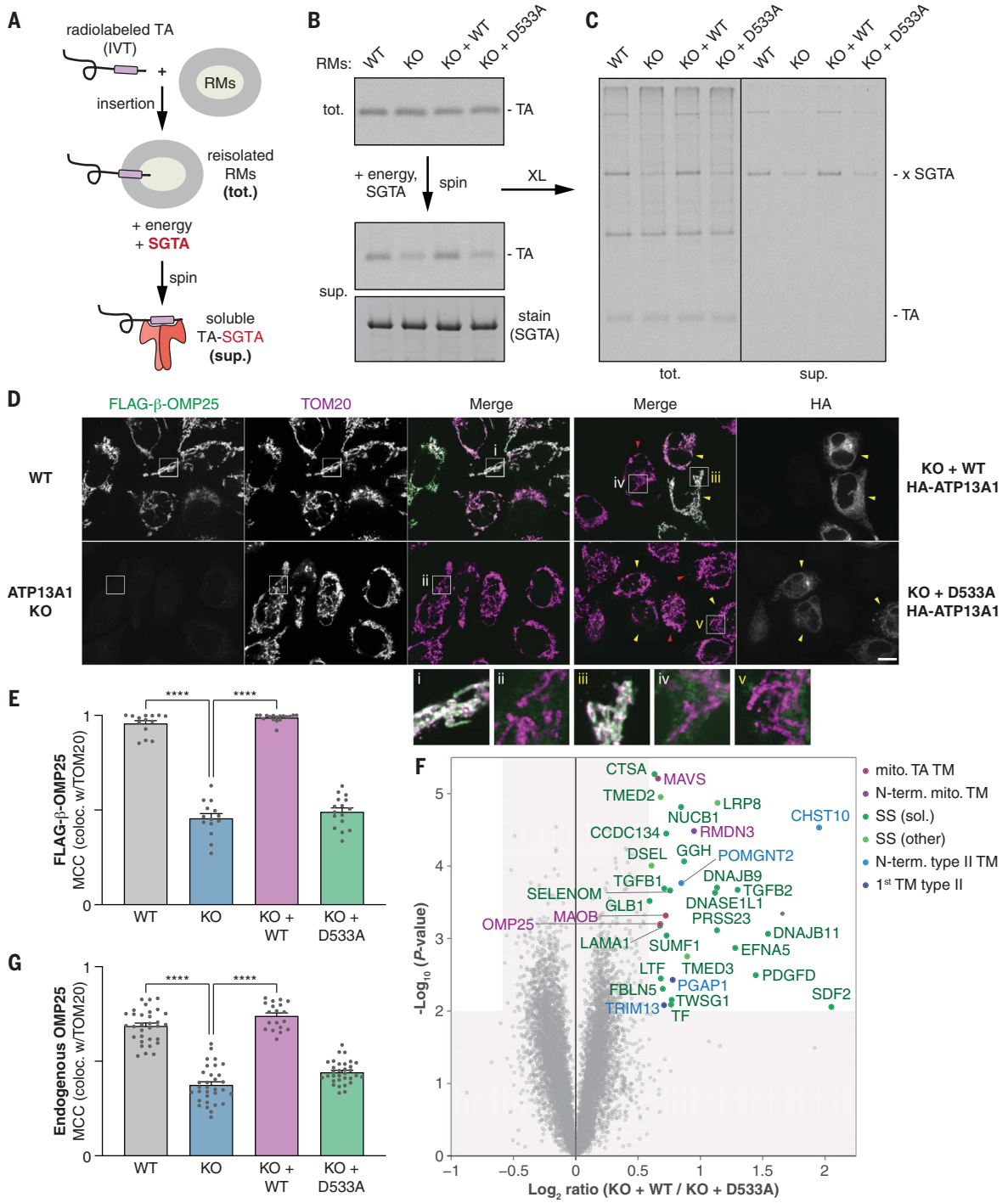

Fig. 2. ATP13A1 mediates TM removal from the ER. (**A**) Scheme to reconstitute TA protein dislocation from ER-derived RMs. IVT-radiolabeled TA protein is incubated with RMs from WT, ATP13A1 KO, or KO Flp-In T-REx 293 cells stably reexpressing WT or D533A ATP13A1. RMs containing inserted TA protein (tot.) are reisolated and incubated with an energy-regenerating system and the cytosolic TM chaperone SGTA. TA proteins dislocated from RMs are separated by centrifugation (sup.). (**B**) SDS-PAGE and autoradiography of tot. and extracted (sup.) TA protein containing the OMP25 TM with the indicated RMs. Equal recovery of SGTA (Coomassie) and TA protein cross-links to SGTA (x SGTA) are indicated. (**C**) As in (B), after cross-linking with 250 μM BMH. (**D**) IF of endogenous TOM20 (purple; mitochondrial marker) and FLAG-tagged TA protein containing the OMP25 TM (FLAG-β-OMP25; green) stably expressed in (left) WT, ATP13A1 KO, or (right) KO Flp-In T-REx HeLa cells transfected with WT or D533A HA-tagged ATP13A1 (yellow arrowheads, transfected cells; red arrowheads, untransfected cells; also see fig. S5E). Scale bar, 10 μm. Panels below show high-magnification views of boxed regions; intensity of FLAG-β-OMP25 is enhanced in ii, iv, and v. (**E**) Mean ± SEM and individual MCC values of FLAG-β-OMP25 colocalization with TOM20. ****$P < 0.0001$. (**F**) Volcano plot showing relation of the P value and $\log_2$ enrichment of proteins in ATP13A1 KO Flp-In T-REx HeLa cells reexpressing WT versus D533A FLAG-ATP13A1. Significantly enriched proteins are classified on the basis of expected cellular localization and TM topology. mito., mitochondrial; N-term., N-terminal; SS, signal sequence; sol., soluble protein after SS cleavage. (**G**) Mean ± SEM and individual MCC of endogenous OMP25 colocalization with TOM20 in the indicated cells.

ATP13A1, but not D533A ATP13A1 (Fig. 2F and figs. S9B and S10, A to D). Except for one, all of these candidates were mitochondria- or ER-targeted proteins.

Endogenous OMP25 and two additional mitochondrial TA proteins, MAVS and MAOB, were among these candidates, consistent with the decrease in OMP25 reporter levels in ATP13A1 KO cells that was rescued by WT ATP13A1 (fig. S5E). Another identified mitochondrial protein, RMDN3, has a single N-terminal TM that inserts in the N_{lumen}/C_{cyto} orientation. These candidates all have a TM flanked by a short, positively charged lumenal segment (fig. S10A). Immunofluorescence (IF) verified mislocalization of endogenous OMP25 and RMDN3 in ATP13A1 KO cells, which was specifically rescued by reexpressing WT ATP13A1 (Fig. 2G and fig. S10, E and F).

The remaining ATP13A1-dependent proteins contain an N-terminal ER-targeting signal sequence or type II TM, which should adopt an N_{cyto}/C_{lumen} topology (fig. S10B) (*31*). Proteins without an N-terminal hydrophobic helix were not enriched, arguing against a general defect in ER protein maturation. Although highly diverse, signal sequences and type II TMs are generally less hydrophobic than TMs of the opposite topology and often have positively charged N-termini (*32*). The N-termini of candidate signal sequences also appear enriched in prolines (fig. S10, B and G). These biophysical features resemble mitochondrial TA proteins and raise the possibility that ATP13A1 may mediate the removal of these terminal hydrophobic helices if they are inserted in the wrong orientation (N_{lumen}/C_{cyto}) (fig. S10, B and H). Together, our data support a QC function for P5A-ATPases in removing misinserted terminal hydrophobic helices from the ER.

Cryo-EM structure of apo Spf1

The P5A-ATPase is an orphan transporter, and our results suggesting a role in TM dislocation were puzzling because P-type ATPases are generally assumed to transport cations or lipids. To understand the substrate selectivity of this family of transporters, we determined the structure of the P5A-ATPase Spf1 from *Saccharomyces cerevisiae* using single-particle cryo-EM (Fig. 3, A and B, and table S1). We attached a green fluorescent protein (GFP) tag to the 3′ end of the chromosomal *SPF1* gene and extracted endogenous Spf1 from yeast membranes with a dodecyl maltoside (DDM)/cholesteryl hemisuccinate (CHS) mixture. Spf1 purified using anti-GFP nanobody affinity resin eluted as a single peak in size-exclusion chromatography (fig. S11, A and B). Cryo-EM images of apo Spf1 purified without any nucleotide or phosphate analogs displayed well-dispersed particles (fig. S11C). Two-dimensional (2D) image classification was used to remove empty micelles and some poor-quality particles (fig. S11, D and E), resulting in 216,994 particles that showed 2D projections of Spf1 from various angles with clear protein features (fig. S11E). Ab initio reconstruction and 3D classification indicated that most Spf1 molecules were in a single conformation (fig. S11D). Approximately 60% of particles from the 2D classification were used to reconstruct the final apo map at 3.5-Å resolution (Fig. 3A, movie S1, and fig. S11, D to G). Many side chains were clearly visible,

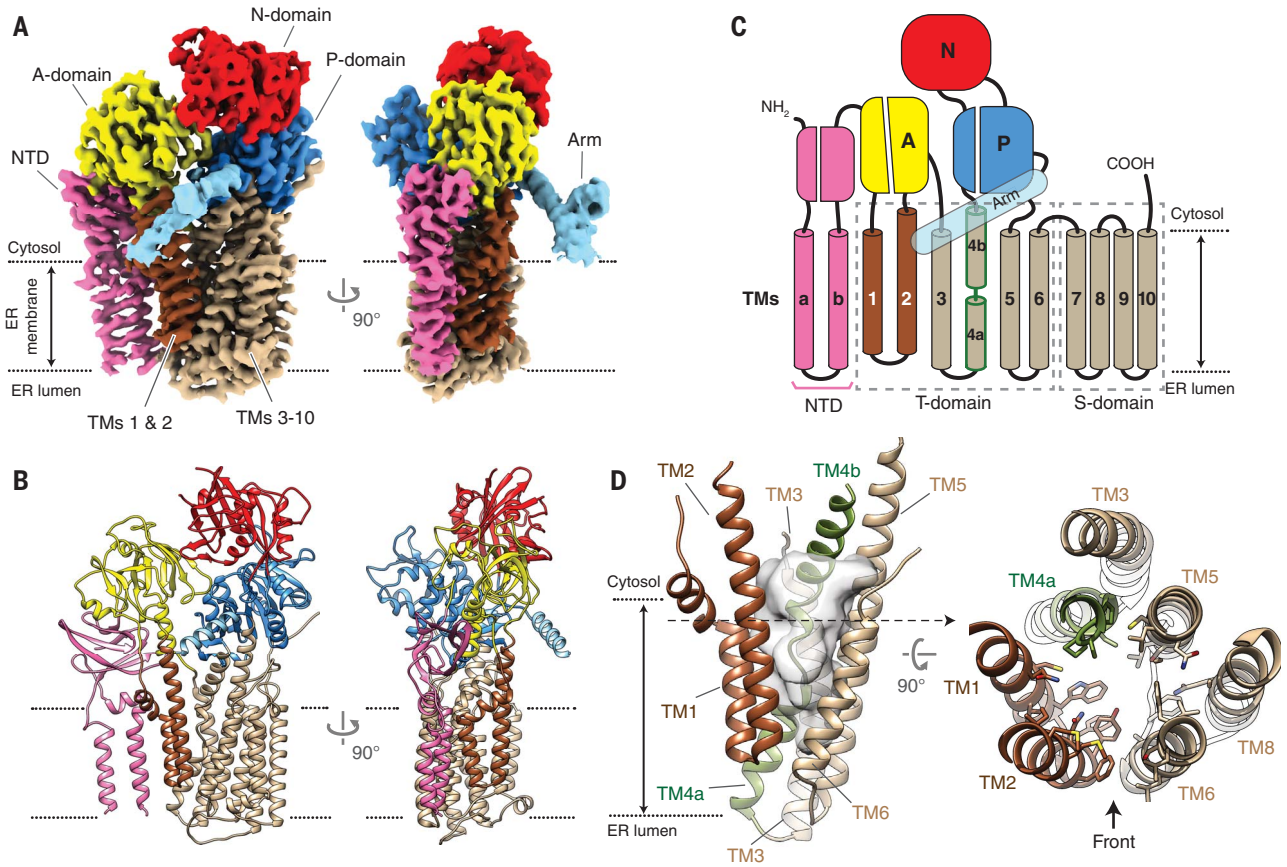

Fig. 3. Structure of apo Spf1 in an inward-open conformation. (**A** and **B**) 3.5-Å-resolution cryo-EM reconstruction (A) and atomic model (B) of the apo Spf1. Note the V-shaped opening of the substrate-binding pocket between TMs 1 and 2 (brown) and TMs 3 to 10 (tan). Dotted lines show the approximate boundaries of the ER membrane. (**C**) Domain architecture of Spf1. Note that the helix of TM4 (outlined in green) is unraveled halfway by a conserved PP(E/D)LP motif. (**D**) Views into the substrate-binding pocket. Left is a front view. For clarity, only TMs 1 to 6 are shown. The solvent-accessible volume (~3500 $Å^3$) is shown in semitransparent gray. Right panel is a view from the cytosol (TM8 is also shown). Side chains lining the cavity are shown in a stick representation.

enabling de novo building of an atomic model (fig. S12).

The apo Spf1 structure showed all core domains of P-type ATPases, namely the cytosolic A (actuator), P (phosphorylation), and N (nucleotide binding) domains and the T (transport) domain formed by TMs 1 to 6 (Fig. 3, A to C, and fig. S13). In addition, as is common in P2- to P5-type ATPases, Spf1 contains an S (support) domain (TMs 7 to 10) that tightly packs against TM5 and TM6. The structure also showed two features specific to the P5A-ATPase: an N-terminal domain (NTD) preceding the A domain and an "arm"-like elongated domain protruding between the P domain and TM5. The NTD contains a seven-stranded β-barrel in the cytosol, which is tightly bound to the A domain, and two additional TMs (TMa and TMb), which appear to be only loosely associated with TMs 1 and 2 through lipid and/or detergent molecules (fig. S14A). The arm domain extends from the P domain with a conserved α-helix and positions its distal portion upon the detergent micelle (Fig. 3A and fig. S14B). An atomic model for this region could not be built because of poor local resolution, but the micelle around the contact was noticeably pulled up toward the arm domain (fig. S14B), suggesting that the arm domain might affect local membrane structure.

Apo Spf1 has a large inward-open substrate-binding pocket

In all P-type ATPases, the substrate-binding site is formed mainly by TM2, TM4, and TM6 of the T domain at the point where the TM4 helix is disrupted [in Spf1, at the PP(E/D)LP motif between TM4a and TM4b]. Apo Spf1 also shows a prominent pocket for substrate binding in this site, but with an unusually large V-shaped cavity compared with other P-type ATPases (Fig. 3D and fig. S15). The pocket is blocked on the ER lumenal side and open toward the cytosol. Thus, the apo structure represents an inward-open conformation of the transporter. The inner surface is lined with a mixture of hydrophilic and hydrophobic side chains (fig. S15, A and C) and exhibits negative electrostatic potential (fig. S16A) that is contributed collectively by D215, E232, D434, E446, and E450. These acidic amino acids are highly conserved in P5A-ATPases across species but not in the closest subfamily of P5B-ATPases (fig. S16B).

One noticeable feature of the putative substrate-binding pocket is that it is open both to the cytosol and laterally toward the lipid phase in the cytosolic leaflet of the ER membrane between TM2 and TM6 (Fig. 3D and fig. S15A). In P2-ATPase cation pumps, such as the sarcoplasmic/endoplasmic reticulum Ca^{2+}-ATPase (SERCA) and Na^{+},K^{+}-ATPase, the T domain forms a small ion-binding cavity that is shielded away from the membrane (*33*–*37*). In P4-ATPase lipid flippases, the equivalent pocket, which is also small and binds to a phospholipid head group, is exposed only to the lipid phase (*38*–*40*). The unusual size and topology of the substrate pocket suggests that the P5A-ATPase has fundamentally different substrate specificities than other P-type ATPases with known structures. The structure did not reveal any sites in the pocket of Spf1 that could specifically coordinate a metal ion, arguing against the idea that the P5A-ATPase transports cations (*10*, *18*).

Structure of Spf1 in an outward-open conformation

P-type ATPases undergo a series of conformational changes with ATP binding, phosphorylation of a conserved aspartate (D487 in Spf1, D533 in ATP13A1), and subsequent dephosphorylation in a scheme known as the Post-Albers cycle (i.e., E1 → E1-ATP → E1P-ADP → E1P → E2P → E2-Pi → E1; fig. S17A). Transitions between the E1 and E2 states result in large conformational changes in the T domain that mediate substrate transport. Because the apo structure of Spf1 represents only the E1 form, we sought to elucidate different conformational states by adding nucleotide or phosphate analogs to purified Spf1. To this end, we obtained structures of Spf1 in complex with β,γ-methyleneadenosine 5′-triphosphate (AMP-PCP), AlF_4^-, and BeF_3^-, at overall resolutions of 3.7, 3.4, and 3.3 Å, respectively (fig. S18). AMP-PCP, a nonhydrolyzable ATP analog, locks the enzyme in an ATP-bound state, and the phosphate analogs AlF_4^- and BeF_3^- form a stable complex with the side-chain carboxylate of D487 to mimic a phosphorylated aspartate (*37*). All three structures show clear EM density for these inhibitors bound at the phosphorylation site (fig. S19, A to C). On the basis of the arrangement of the A, P, and N domains and comparison with other P-type ATPase structures (*37*, *39*), we assigned the AMP-PCP, AlF_4^-, and BeF_3^- structures as the E1-ATP, E1P, and E2P states, respectively. The AMP-PCP– or AlF_4^--bound Spf1 structures were essentially identical to the apo structure (root mean square deviations of 0.56 and 0.48 Å, respectively; fig. S19, D and E). Only a slight (7°) inward rotation was seen with the N domain of AMP-PCP–bound Spf1 as AMP-PCP bridges the interface of the N and P domains. The T domain maintained the inward-open conformation in both the AMP-PCP– and AlF_4^--bound structures.

By contrast, the BeF_3^--bound E2P structure showed a substantially different conformation (Fig. 4, A and B; movie S2; and fig. S19, F and G). Similar to other P-type ATPases, the N domain of Spf1 undergoes a large (~50°) outward rotation with respect to the P domain during the E1P to E2P transition. This allows the A domain, which contains a conserved (S/T)GES motif for dephosphorylation, to access the phosphorylation site through an ~24° inward rotation of the A domain and NTD toward the N-P interface. Because TM1 and TM2 are linked to the A domain, this motion substantially restructures the substrate-binding pocket. TM2 and TM6, which contact each other on the ER lumenal side in a V-shaped arrangement in the E1 states, spread out into a parallel arrangement, and the cytosolic segment of TM4 (denoted TM4b) moves in between TM2 and TM6 toward the lipid phase by a tilting motion (Fig. 4D and movie S3). Consequently, the inward-open V-shaped substrate pocket transforms into an outward-open, inverted U–shaped pocket (Fig. 4, C and D, and fig. S15B). During this E1 to E2 transition, the lateral opening to the lipid phase is maintained but shifts from the cytosolic to the lumenal leaflet of the ER membrane (movie S3). The surface of the pocket maintains a negative electrostatic potential (Fig. 4C), suggesting that substrates likely contain positive charges in addition to a hydrophobic component, which would interact with the acyl chains of lipids at the lateral opening. These features are consistent with the TMs of mitochondrial TA proteins and the terminal hydrophobic helices of ATP13A1-dependent proteins identified in our proteomics analyses (Fig. 2F).

Visualization of a putative Spf1 substrate

Finally, we sought to visualize substrate-engaged Spf1. Although we did not observe substrate density in the structures obtained with Spf1 purified as described above, we reasoned that endogenous substrates may copurify with Spf1 trapped in the outward-open E2P conformation. Accordingly, we repeated the extraction and purification of Spf1 with BeF_3^- included in all buffers. The resulting 3.3-Å-resolution structure (fig. S18, J to L, P) was essentially identical to the E2P structure but with a prominent difference: an additional elongated density of a putative substrate traversing the lateral opening of the substrate pocket (Fig. 4E and fig. S20A).

The putative substrate density spans almost the entire membrane and closely resembles an α-helical TM that can accommodate a 20-residue-long polyalanine model (Fig. 4, E and F). The large cylindrical shape is incompatible with detergents, lipids, and sterols (fig. S20B). In the cytosolic leaflet of the membrane, the density is exposed to the lipid phase and may interact with hydrophobic amino acids of TM2 (F223, M227, M231), TM4b (M449, M453), and the conserved PP(E/D)LP motif (P445) between TM4a and TM4b. In the lumenal leaflet, the density is directed to the inverted U–shaped pocket. This density likely represents an average of multiple different copurified substrates, possibly explaining the lower resolution compared with Spf1. Altogether,

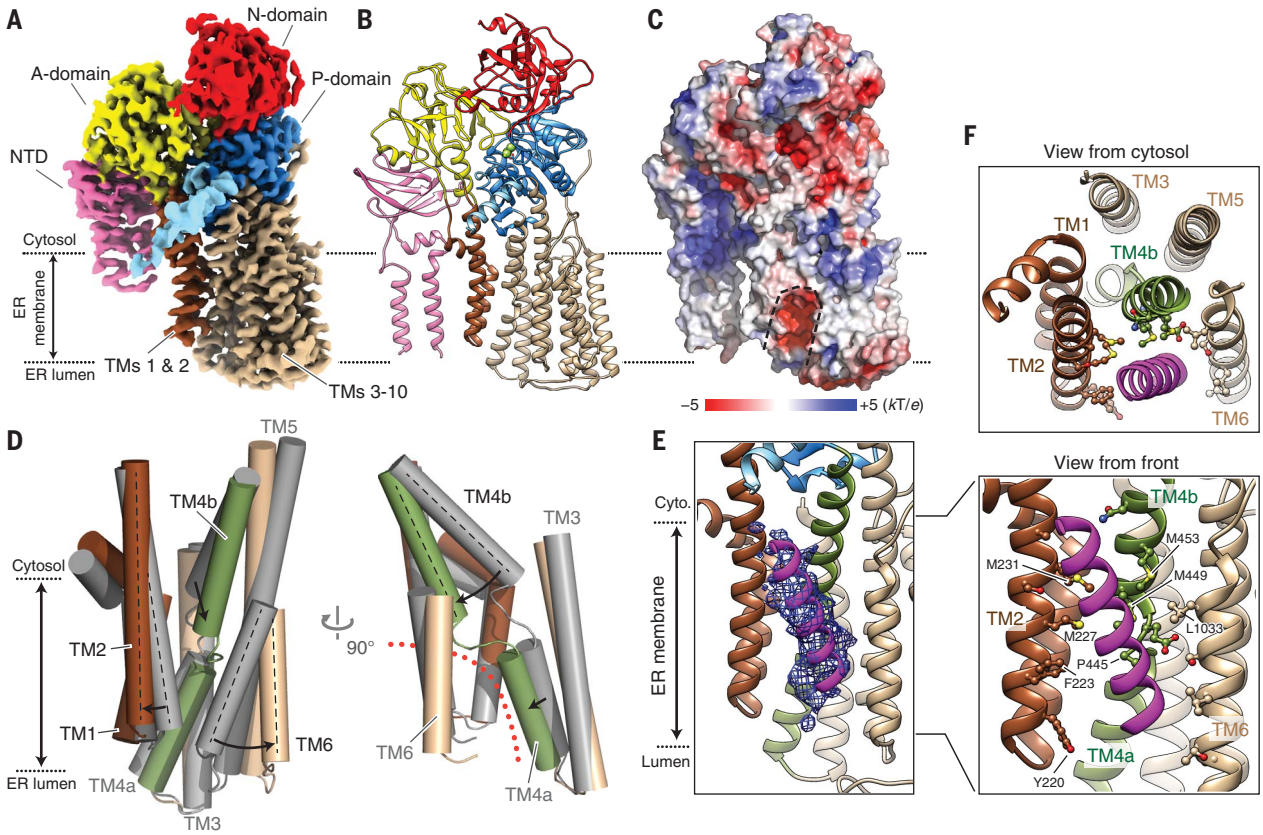

Fig. 4. Structure of Spf1 in an outward-open conformation. (**A** and **B**) 3.3-Å-resolution cryo-EM reconstruction (A) and atomic model (B) of the BeF_3-bound Spf1. Shown are the front views. We note that, unlike the inward-open structure, TMa and TMb are flexible in this conformation. TMa and TMb were modeled as polyalanine helices on the basis of the apo structure. (**C**) Heatmap of surface electrostatics. The substrate-binding cavity is outlined with a dashed line. (**D**) Conformational changes of TMs 1 to 6 from the inward-open (apo; gray) to the outward-open (BeF_3-bound; colored) states. Left is a front view and right is a side view. The outward-open substrate-binding pocket is indicated by an orange dotted line. (**E**) Density of copurified putative substrate (magenta mesh; 5-Å low-pass filtered) fitted with a polyalanine helix model (also see fig. S20A). (**F**) As in (E) but with amino acid side chains of Spf1 facing the substrate density shown in a ball-and-stick representation. Top is a cytosolic view and bottom is a front view.

our structural and functional data indicate that the P5A-ATPase dislocate misinserted TMs from the ER membrane.

Discussion

Our results assign transmembrane helices as the substrates of the ER-resident P5A-ATPase, thereby defining an additional P-type ATPase function of transporting polypeptides out of lipid bilayers. Until recently, P-type ATPases were thought to be exclusively cation or lipid pumps. Together with the report that the P5B-ATPase ATP13A2 transports polyamines (*8*), our study reveals that P-type ATPases mediate transport of unexpectedly diverse substrates. Although the T domains of all P-type ATPases display a similar overall arrangement of TMs 1 to 6, our structures demonstrate that they can form fundamentally different substrate-binding sites. The large substrate-binding pocket of Spf1, with an opening that not only alternately faces the cytosol and the ER lumen but also remains laterally accessible from the membrane, is distinctive among P-type ATPases characterized to date. We propose that the P5A-ATPase uses this specialized pocket to extract mistargeted or misinserted TMs with a short flanking lumenal hydrophilic segment from the ER (Fig. 5). In this working model, we hypothesize that the substrate TM largely remains in the lipid phase, whereas the lumenal segment is flipped across the membrane by the outward- to inward-open transition of the large cavity in the T domain. Moderate hydrophobicity characteristic of signal sequences and mitochondrial TMs may lower the energetic barrier for dislocation. Positive charges in the lumenal segment may be the preferred clients, whereas large lumenal segments are likely excluded because of the limited space in the pocket.

TM dislocation by the P5A-ATPase also reveals a previously unidentified protein QC and safeguarding mechanism at the ER. Active transport by the P5A-ATPase is required to dislocate mitochondrial TMs that mistarget to the ER. P5A-ATPase function at the ER appears similar to Msp1 at the outer mitochondria membrane; although structurally unrelated, both use ATP as an energy source to dislocate TMs, possibly providing opportunities for reinsertion into the correct membrane. This idea is consistent with emerging observations that ER and mitochondrial factors cooperate to degrade aberrant TM-containing proteins (*11*, *30*) and to ensure high-fidelity mitochondrial protein import, as in the 'ER-SURF' pathway (*41*). The P5A-ATPase may also dislocate ER-targeted N-terminal hydrophobic helices such as signal sequences that erroneously insert in the N_{lumen}/C_{cyto} orientation, although the exact basis of these substrates' dependence on the P5A-ATPase remains unclear. Biophysical features of P5A-ATPase–dependent clients resemble substrates of the ER membrane protein complex (EMC), which inserts moderately hydrophobic TA proteins and terminal TMs in the N_{lumen}/C_{cyto} orientation (*23*, *42*). EMC and the P5A-ATPase may thus have mechanistically opposing activities at the ER. Disruption of EMC also causes a wide range of ER-related dysfunctions

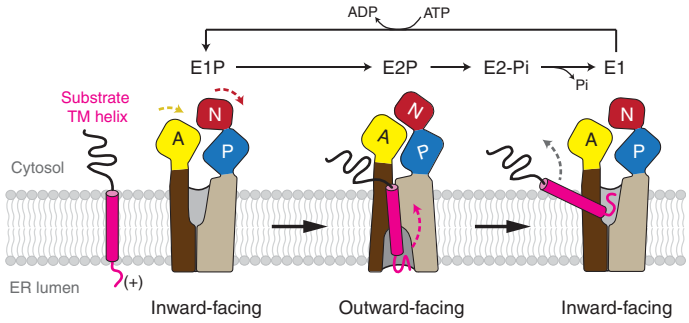

Fig. 5. Proposed model for TM dislocation by the P5A-ATPase. The P5A-ATPase likely alternates between two conformations, inward-open E1 and outward-open E2 states. During the E1P-to-E2P transition, the N domain rotates (red) and the A domain (yellow) moves closer to the N-P interface, causing conversion of the inward-open substrate-binding pocket of the transmembrane domain (brown and tan) to the outward-open conformation. In this model, a substrate TM helix (magenta) with a short, preferentially positively charged lumenal segment would bind to the outward-open pocket and the E2P-to-E1 transition would flip the TM by a switch from the outward-open to inward-open conformation. For simplicity, some intermediate steps of the Post-Albers cycle are not shown.

(*17*, *43*), similar to the pleiotropic phenotypes associated with P5A-ATPase mutants. Thus, cells appear to spread the burden of managing very diverse TMs by using an arsenal of different machineries, each with varying substrate selectivity, that collaborate to fine-tune TM localization and topology.

Materials and Methods

Plasmids and antibodies

To express recombinant TA protein in complex with CaM (fig. S1A), the open reading frame of a model TA protein containing the cytosolic domain of SEC61β and OMP25 TM as described in (*44*) was appended after a 3C protease cleavage site to the coding sequence of pGEX-CaM (*22*). N-terminal FLAG tags and amber codons were introduced using conventional molecular biology techniques. pGEX-SGTA (*24*), pEVOL-Bpa for expressing amber codon suppression components in bacteria (*45*), and plasmids for expressing recombinant Bpa-RS and for suppressor tRNA transcription (*46*) have been described previously.

SP64-based plasmids used to generate in vitro transcription templates were as previously described (*47*). TM substitutions and introduction of amber stop codons for Bpa incorporation (e.g., Fig. 1E) were accomplished using conventional Gibson assembly and Phusion mutagenesis approaches. Model TA protein-coding sequences were transferred to pcDNA5/FRT/TO vectors for stable incorporation into Flp-In T-REx HeLa cells (a gift from B. Raught) behind a doxycycline-inducible cytomegalovirus (CMV) promoter (e.g., Fig. 2, D and E). TM sequences were exchanged using Gibson assembly.

ATP13A1 cDNA (Harvard plasmID no. HsCD00082872) was cloned into pcDNA5/FRT/TO behind an N-terminal 3xFLAG tag by restriction enzyme digestion and Gibson assembly. Sequence encoding the N-terminal 132 amino acids of ATP13A1 not present in the cDNA construct and the D533A mutations was introduced by Gibson assembly. To modulate induced expression levels (fig. S9A), the Promega-series CMV*d1* truncation was generated in pcDNA5/FRT/TO expression vectors using conventional molecular biology techniques. ATP13A1 coding sequences were transferred from pcDNA5 to pcDNA3.1-based vectors behind 3xFLAG and 3xHA tags for transient transfection (e.g., Fig. 2D) by restriction enzyme digestion and T4 ligation. pOG44 (Thermo Fisher Scientific V600520) and pX459 (*48*) are as described previously. Guide RNA sequences (GAG CAC CGT CCC ATA CCC GG, ACG CGC TCA CTG TCC TCT CG) were cloned into pX459 for generating KO cells using Gibson assembly.

Homemade rabbit polyclonal antibodies against TRAPα [1:5000 for immunoblotting (IB); 1:300 for IF], GFP (1:5000 for IB), and 3F4 (1:350 for IP) were gifts from the Hegde laboratory. Antibodies against TOM20 (Abcam ab186735) (1:5000 for IB, 1:300 for IF), TOM20 (Santa Cruz Biotechnology sc-17764; RRID:AB_628381; 1:50 for IF), ATP13A1 (Proteintech 16244-1-AP; RRID:AB_2290293; 1:5000 for IB), FLAG M2 (Sigma-Aldrich F1804; RRID:AB_262044; 1:5000 for IB; 1:500 for IF), CNX (Enzo Life Sciences ADI-SPA-865; RRID:AB_10618434; 1:5000 for IB), Por1 (Abcam ab110326; RRID:AB_10865182; 1:2500 for IB), ATAD1 (Abcam ab94583; RRID:AB_10672816; 1:1000 for IB), DNAJB11 (Proteintech 15484-1-AP; RRID:AB_2094400; 1:2000 for IB), MAVS (Cell Signaling Technology 3993; RRID:AB_823565; 1:1000 for IB); OMP25 (Abcam ab224217; 1:50 for IF); OMP25 (Proteintech 15666-1-AP; RRID:AB_2201149; 1:1000 for IB); RMDN3 (Thermo Fisher Scientific PA5-52680; RRID:AB_2646594; 1:1000 for IB; 1:100 for IF) are commercially available. For immunoblotting, horseradish peroxidase–conjugated anti-mouse (Jackson ImmunoResearch Laboratories 115-035-003; RRID:AB_10015289) and anti-rabbit (Jackson ImmunoResearch Laboratories 111-035-003; RRID:AB_2313567) antibodies were used at 1:5000. For IF, Alexa Fluor 488–conjugated goat anti-mouse IgG (Jackson ImmunoResearch Laboratories 115-545-003; RRID:AB_2338840), Alexa Fluor 564–conjugated goat anti-rabbit IgG secondary antibodies (Jackson ImmunoResearch Laboratories 111-585-003; RRID:AB_2338059), and DyLight 680-conjugated anti-hemagglutinin (HA) antibody (Thermo Fisher Scientific 26183-D680; RRID:AB_2533054) are commercially available.

Yeast strains

BY4741 and Spf1-GFP (e.g., Fig. 1D) yeast strains used for membrane preparations and cross-linking analyses (Fig. 1 and fig. S1) were obtained from the Finley laboratory (Harvard Medical School). To tag endogenous Spf1 with a 3xFLAG tag (e.g., Fig. 1E), a DNA fragment containing coding sequence for a linker (GSGGRIPGLINM), 3xFLAG, and a hygromycin resistance marker flanked by 50 to 60 bp homologous to the 3′ regions of *SFP1*, was generated by polymerase chain reaction (PCR) using the pFA-6a-3xFLAG-Hyg plasmid (a gift from P. Feng, Harvard Medical School) as a template and a pair of primers (forward: 5′-caaa cc atc aga cat ttc tgt gca aca ggt caa gat tgc ctc taa agg atc cgg agg acG GAT CCC CGG GTT AAT TAA-3′; reverse: 5′- ggg taa tat aag tat ata aat aca aaa agg ggt act aca taa aag att taG AAT TCG AGC TCG TTT AAA CTG-3′; lowercase and uppercase, specific to the chromosomal and template sequences, respectively). DNA was introduced to BY4741 by a standard lithium acetate transformation protocol before selection with 100 μg/ml hygromycin in yeast extract, peptone, and dextrose (YPD) agar. Successful FLAG tagging and protein size was confirmed by immunoblotting and Sanger sequencing.

To enable affinity purification of endogenous Spf1 from *S. cerevisiae*, a cleavable GFP tag was introduced to the 3′ end of the *SPF1*-coding sequence of the WT strain BY4741. First, a DNA fragment containing a coding sequence for GFP and a nourseothricin resistance marker, which is flanked by ~60-bp sequences homologous to the 3′ regions of *SFP1*, was generated by PCR using the pSK-B399 plasmid (a gift from S. Klinge, Rockefeller University) as a template and a pair of primers (forward: 5′-c ttc atg gac gac aaa cca tca gac att tct gtg caa cag gtc aag att gcc tct aaa GGG GCA ACT GGT GGT AG-3′; reverse: 5′-a ctt aga agc tgt ttt aca aat aat aca gca ctt tca taa actt aac aat aca ccc CGG CGT TAG TAT CGA ATC G-3′; lowercase and uppercase, specific to the chromosomal and template sequences, respectively).

The DNA segment also contains a 31-amino-acid-long protease-cleavable linker [GATGGSTAGGATTASGTG ENLYFQG TASGGG; underlined, a Tobacco etch virus (TEV) protease cleavage site] between the last codon of *SPF1* and the first codon of GFP. DNA was then introduced to BY4741 by a standard lithium acetate transformation protocol. Transformants were isolated from a YPD agar medium (1% yeast extract, 2% peptone, 2% glucose, and 2% Bacto Agar) containing 100 μg/ml nourseothricin. Correct chromosomal integration was confirmed by PCR and Sanger sequencing.

Protein purification for biochemical assays

To purify TA(Bpa) in complex with CaM, BL21(DE3) cells were cotransformed with pGEX-CaM-FLAG-OMP25(amb) and pEVOL-Bpa and grown in Luria broth under appropriate antibiotic selection to an optical density 600 nm (OD_{600}) of 0.6. The cultures were then supplemented with 1 mM Bpa (Bachem 4017646) and induced with 1% arabinose and 0.2 mM isopropyl-β-D-thiogalactopyranoside for 6 hours at 25°C. Cells were harvested and resuspended in ice-cold lysis buffer [1× phosphate-buffered saline (PBS), 0.5 mM $CaCl_2$, 1 mM dithiothreitol (DTT), 1× protease inhibitor cocktail (PIC); Sigma-Aldrich 5056489001] and lysed by passing through a microfluidizer two times. Soluble material after centrifugation at 34,541*g* for 20 min in a SS34 rotor (Sorvall) was applied to 1 ml of packed glutathione Sepharose (GE Life Sciences 17075601) resin equilibrated in lysis buffer per liter of culture. Columns were washed with 10 column volumes of lysis buffer and eluted with 50 mM Tris (pH 8), 25 mM reduced glutathione, and 0.5 mM $CaCl_2$. Peak elution fractions were pooled and dialyzed against 50 mM Hepes (pH 7.4), 150 mM KOAc, 2 mM $Mg(OAc)_2$, 10% glycerol, 1 mM DTT, and 0.5 mM $CaCl_2$ for 2 hours before the addition of 1:100 w/w GST-3C protease and dialysis against fresh buffer for 12 to 16 hours. Dialyzed material was passed over glutathione Sepharose column to subtract cleaved GST and GST-3C before being aliquoted and frozen in liquid nitrogen. SGTA, GST-3C protease, and Bpa-RS were expressed in BL21(DE3) *Escherichia coli* and purified as described previously (*24*, *46*).

Preparation of yeast membranes

Yeast strains were grown in YPG to an OD_{600} of 2, harvested, washed in distilled water, resuspended in 100 mM Tris-H_2SO_4 (pH 9.4) with 10 mM DTT, and incubated at 30°C for 20 min. Cells were then washed in zymolyase buffer [20 mM potassium phosphate (pH 7.4), 1.2 M sorbitol], resuspended in zymolyase buffer containing 3 mg of zymolyase per gram of cells and incubated at 30°C for 30 min. After another wash in zymolyase buffer, cells were lysed in ice-cold homogenization buffer [10 mM Tris-HCl (pH 7.4), 0.6 M sorbitol, 1 mM EDTA, 1 mM phenylmethylsulfonyl fluoride (PMSF), 0.2% bovine serum albumin (BSA)] using a prechilled glass-Teflon Dounce homogenizer. One volume of homogenization buffer was added and the mixture was centrifuged at 1500*g* for 5 min. The supernatant was centrifuged at 4000*g* for 5 min and again at 12,000*g* for 15 min. The pellet from the 12,000*g* spin was resuspended in SEM buffer [20 mM MOPS-KOH (pH 7.2), 250 mM sucrose] and layered on top of a step gradient of 60%, 32%, 23%, and 15% sucrose in 10 mM MOPS-KOH (pH 7.2). Crude membranes were centrifuged at 134,000*g* for 1 hour in a SW 40Ti rotor, and mitochondria-enriched membranes were collected from the 32%/60% sucrose boundary. The membranes were adjusted to 20 to 25 mg/ml protein as measured after solubilization in 1% sodium dodecyl sulfate (SDS), aliquoted, and frozen in liquid nitrogen. ER-enriched membranes were obtained by centrifuging the post-12,000*g* supernatant at 234,787*g* for 45 min in a type 45 Ti rotor. The pellet was resuspended in RM buffer [50 mM Hepes (pH 7.5), 100 mM KOAc, 2.5 mM $Mg(OAc)_2$, 14% glycerol, 1 mM DTT, 1× PIC], adjusted to ~50 mg/ml protein, aliquoted, and flash-frozen in liquid nitrogen. Note that all membrane fractions showed cross-linking to Spf1 caused by residual ER contamination in the mitochondria-enriched membrane fractions.

Photo-cross-linking of recombinant TA with yeast membranes

Reactions were performed in import buffer [50 mM Hepes (pH 7.5), 100 mM KOAc, 2.5 mM $Mg(OAc)_2$, 0.5 mM $CaCl_2$] containing 7.5 to 20 μg/ml FLAG-TA(Bpa) in complex with CaM and 5 mg/ml mitochondria-enriched membranes. FLAG-TA(Bpa) was released from CaM by addition of 2 mM EGTA, and the samples were transferred to a prechilled 96-well plate ~10 cm under a UVP B-100 series lamp for 10 min. Ten volumes of IP buffer [50 mM Hepes (pH 7.5), 100 mM KOAc, 2.5 mM $Mg(OAc)_2$, 1% Triton X-100, 1× PIC] were added to each well, and the samples were incubated on ice for 10 min to solubilize membranes and centrifuged at 21,000*g* for 5 min. The supernatant was added to M2 anti-FLAG affinity resin (Sigma-Aldrich A2220) and mixed at 4°C for 2 hours. M2 FLAG beads were washed twice with IP buffer, twice with IP buffer + 0.5 M NaCl, and another two times with IP buffer. Elutions were performed with 0.15 mg/ml 3x FLAG peptide in IP buffer at 30°C for 20 min. Samples for TMT-MS analysis were treated with 10 mM DTT at 55°C for 30 min, followed by 50 mM chloroacetamide at 25°C in the dark for 20 min. For immunoblotting, elutions were precipitated by the addition of one-fifth the elution volume of trichloroacetic acid, incubated on ice for 15 min, and centrifuged at 21,000*g* for 1 min. The pellet was washed twice with ice-cold acetone and resuspended in protein sample buffer.

Generation of KO and stable inducible cell lines

All cell lines were maintained in Dulbecco's modified Eagle's medium (DMEM) with high glucose, GlutaMAX, and sodium pyruvate (Thermo Fisher 10569) with 10% fetal bovine serum (FBS) at 37°C and 5% CO_2. Parent HEK293T, Flp-In T-REx 293, and HeLa T-REx cell lines were authenticated by short tandem repeat analysis. ATP13A1 KO cell lines were generated by transfecting Flp-In T-REx HeLa (Fig. 2D and figs. S5 to S9) or Flp-In T-REx 293 (Fig. 2, A to C, and figs. S3 and S4) cells with pX459 plasmids containing target guide RNAs using Lipofectamine 2000 or TransIT293 (Mirus Bio), respectively, according to the manufacturer's instructions. After 24 hours, transfected cells were selected with 2 mg/ml puromycin for 48 hours. Single clones were isolated and KOs validated by immunoblotting and amplicon sequencing.

To establish stable doxycycline-inducible cell lines expressing either FLAG-tagged tail-anchored proteins or FLAG-tagged ATP13A1, WT or ATP13A1 KO Flp-In T-REx HeLa or 293 cells were cotransfected with a 1:1 ratio of pOG44 and pcDNA5/FRT/TO vector containing the desired insert using Lipofectamine 2000/Lipofectamine 3000 or TransIT293 (Mirus Bio), respectively. After 24 hours, cells were selected with 10 μg/ml blasticidin and 150 to 300 μg/ml hygromycin for at least 2 weeks, and expression was validated by induction with 10 ng/ml doxycycline for 24 to 48 hours and immunoblotting.

Isolation of RMs

RMs were isolated from WT, ATP13A1 KO, and ATP13A1 KO Flp-In T-REx 293 cells stably reexpressing FLAG-tagged WT or D533A ATP13A1 essentially as described previously (*42*). Cells were cultured for at least two passages in antibiotic-free medium. Reexpression of approximately endogenous levels of FLAG-ATP13A1 in the rescue lines (fig. S3A) was achieved by trace levels of tetracycline present in the FBS in the culture medium, and no additional doxycycline was added. Cells were harvested and washed twice in cold PBS and centrifuged at 500*g* for 5 min. The cell pellet was resuspended in three volumes of 10 mM Hepes (pH 7.4), 250 mM sucrose, 2 mM $MgCl_2$, and 1× PIC, and lysed by 25 to 30 passages through a 27-gauge needle. Lysates were centrifuged twice at 3800*g* for 30 min, and the supernatant was centrifuged at 75,000*g* for 1 hour at 4°C in a TLA-55 or TLA-100.3 rotor. The RM pellet was resuspended in 10 mM Hepes (pH 7.4), 250 mM sucrose, 1 mM $MgCl_2$, 0.5 mM DTT, adjusted and normalized to an

absorbance at 280 nm (A_{280}) value of 30 to 60 as measured after solubilization in 1% SDS, and used directly for insertion and extraction assays.

In vitro translation, insertion, extraction, and photo-cross-linking

For most in vitro transcription reactions, linear DNA templates were generated by PCR of SP64-based vectors using primers annealing slightly upstream of the SP6 promoter and ~200 bp downstream of the open reading frame. Linear DNA templates for transcribing different C-terminal domain sequences (Fig. 1E) were generated using reverse primers containing the desired C-terminal sequence and 16 bp downstream of the TGA stop codon as follows: TGA GAA TTC CTA ATC ATG TC. DNA templates for testing type II constructs (fig. S10H) were generated by PCR directly from gBlocks (IDT) containing the SP6 promoter, the desired protein-coding sequence, and 16 bp downstream of the stop codon as above. In vitro transcription reactions were performed with SP6 polymerase as described previously (*47*) for 1 hour at 37°C and used directly for in vitro translation. Suppressor tRNA (e.g., Fig. 1E) was transcribed from BstN1-lineared plasmid with T7 polymerase at 37°C for 1 hour and isolated by phenol: chloroform extraction. Translation reactions were performed as described previously (*47*) at 32°C for 20 to 30 min. For photo-cross-linking, translation reactions were supplemented with an amber suppression system (*46*) composed of 5 μM in vitro–transcribed suppressor tRNA, 0.5 mM Bpa, and 0.25 μM Bpa-RS. Reactions for targeting assays (fig. S7) included 40 μM cold methionine in place of ^{35}S-methionine. Translation reactions of TA proteins were stopped by the addition of 50 μg/ml RNaseA before the addition of yeast membranes (final concentration of 2 to 5 mg/ml) (e.g., Fig. 1E) or 1:10 v/v RMs (e.g., Fig. 2, A to C). Translation reactions of type II substrates (fig. S10H) included human cell RMs (hRMs).

Insertion reactions with yeast membranes were at 25°C for 20 min. For UV-activated cross-linking, insertion reactions were diluted 10-fold in PSB [50 mM Hepes (pH 7.5), 100 mM KOAc, 2.5 mM $Mg(OAc)_2$] and placed ~10 cm under a UVP B-100 series lamp for 10 min in a prechilled ice block. SDS was added to a final concentration of 1% and samples were heated to 65°C for 5 min. Ten volumes of IP buffer and 10 μl of packed M2 anti-FLAG resin were added, and samples were incubated at 4°C for 1 hour. M2 beads were washed four times in IP buffer before the addition of protein sample buffer. For carbonate extractions (fig. S1B), membranes from 4 μl of insertion reactions were pelleted by centrifugation over a 15% sucrose cushion in PSB at 10,000 g for 10 min at 4°C, resuspended in 150 μl 100 mM $NaCO_3$ (pH 11.3), and incubated on ice for 15 min. Samples were centrifuged at 131,440*g* for 15 min in a TLA100 rotor and the pellets resuspended in protein sample buffer.

Insertion reactions of TA proteins with hRMs were at 32°C for 20 min (Fig. 2B, tot.) or 45 min (fig. S3, B to D). For photo-cross-linking (e.g., Fig. 1E), reactions were diluted 5-fold with PSB, UV irradiated, and immunoprecipitated as described above. Cotranslational insertion reactions (fig. S10H) were subjected to denaturing IPs with α3F4 antibodies and protein A resin (CaptivA). Carbonate extractions (fig. S3D) were performed by the addition of 100 reaction volumes of cold 100 mM $NaCO_3$ (pH 11.5), incubation on ice for 25 min, followed by centrifugation at 250,000*g* for 30 min in a TLA100.3 rotor. Pellets were directly resuspended in protein sample buffer for SDS-PAGE and autoradiography analysis. For analysis of insertion efficiency (fig. S3, B and C) and extraction reactions (Fig. 2, B and C, and fig. S4), RMs were pelleted by centrifugation over four reaction volumes of a 20% sucrose cushion in PSB at 186,000*g* for 20 min at 4°C in a TLA-55 rotor and resuspended in half the initial reaction volume of PSB. Extraction reactions contained ~20 mg/ml RMs (estimated on the basis of total protein concentration), 1 mg/ml SGTA, and either an energy-regenerating system (1 mM ATP, 1 mM GTP, 1.2 mM creatine phosphate, 20 μg/ml creatine kinase) or 1 mM ATP, 1 mM AMP-PCP, or 0.1 U/μl apyrase as indicated, and incubated at 32°C for 30 min. Samples were directly analyzed before or after centrifugation over a 20% sucrose cushion at 186,000*g* for 20 min. Chemical cross-linking (Fig. 2C) was with 250 μM BMH (Thermo Fisher Scientific 22330) at 4°C for 1 hour and directly quenched with protein sample buffer.

IF assays

Flp-In T-REx HeLa cells were cultured either on 13-mm coverslips or in glass-bottomed 24- or 48-well plates (Mattek). For assays with cell lines harboring inducible substrates (Fig. 2D and figs. S5 to S8) and analysis of endogenous substrates (Fig. 2G and fig. S10, E and F), TA protein or Flag-ATP13A1 expression was induced with 100 ng/ml doxycycline for 24 hours. For rescue assays with stable reporters, cells in a 24-well glass-bottomed plate were transiently transfected with 200 ng of pcDNA3 containing HA-tagged WT or D533A ATP13A1 using Lipofectamine 3000 according to the manufacturer's instructions 48 hours before analysis. For targeting assays (fig. S7), Flp-In T-REx HeLa cells in a 48-well glass-bottomed dish were washed twice with PSB and incubated with 200 μg/ml digitonin in PSB for 10 min at 4°C. The cells were washed once with PSB before being incubated with 25 μl of in vitro translation reaction mixture of FLAG-β-OMP25 at 32°C for 15 min.

For imaging, all cells were washed twice in PBS and fixed in 4% formaldehyde in PBS for 15 min. Cells were washed once in PBS, permeabilized with 0.1% Triton X-100 in PBS for 5 min, and then incubated at room temperature with blocking solution (10% FBS in PBS) for 1 hour, followed by primary antibodies in 10% FBS/PBS 1 hour. After three washes in PBS, cells were incubated with 1:500 fluorophore-conjugated secondary antibodies in 10% FBS/PBS for 1 hour and washed three times in PBS before imaging. For ATP13A1 transfection rescue experiments, cells were incubated with 1:100 DyLight 680-conjugated anti-HA antibody (Thermo Fisher Scientific 26183-D680) in 10% FBS/PBS for 1 hour at room temperature or overnight at 4°C and washed three times with PBS. Next, 13 mm coverslips were placed onto SlowFade Gold Antifade Mountant (Thermo Fisher Scientific S36936) and sealed using nail polish. Cells in 24- or 48-well plates were imaged directly in PBS.

All images were collected with a Yokagawa CSU-X1 spinning-disk confocal microscope with Spectral Applied Research Aurora Borealis modification on a Nikon Ti motorized inverted microscope equipped with Plan Apo 100×/1.4 numerical aperture oil-immersion objective. Fluorescence was excited with solid-state lasers at 488 nm (100 mW), 561 nm (100 mW), and 642 nm (100 mW) and collected using ET525/50m, ET620/60m, or ET700/75m emission filters, respectively. Images were acquired with a Hamamatsu ORCA-ER cooled CCD camera. *Z*-series optical sections were collected with a step size of 0.5 μm and single sections were selected from approximately the center of the cell. Brightness and contrast were adjusted identically for compared image sets using Fiji software.

Background subtraction of IF images was performed using the robust Otsu thresholding method (*49*). A region of interest (ROI) was drawn around each cell in the FLAG channel, and colocalization was assessed in 3D using the ImageJ Coloc2 plugin with a point spread function of 2 and 25 randomizations. Manders' colocalization coefficients (MCCs) (*50*) (e.g., Fig. 2E) indicate the contribution of FLAG signal above 0 that overlaps with mitochondria normalized to the total FLAG signal within the ROI. Pearson's correlation coefficients (PCCs) are shown for correlation of FLAG signal with the signal of the ER marker TRAPα (fig. S6) because of the influence of unreliable thresholding of the diffuse ER signal on MCC values. Nonetheless, both MCC1 and MCC2 values with various thresholding techniques support the trends shown in fig. S6, where SEC61β is unaffected, but mitochondrial TA protein colocalization with the ER marker increases in ATP13A1 KO cells. For rescue experiments by transient

transfection (Fig. 2, D and E, and fig. S5, A and B), HA staining was used to identify transfected cells; nontransfected cells were not analyzed. The numbers of cells and fields of views (in parentheses) analyzed were as follows: Fig. 2E, OMP25 WT, n = 14 cells (4 fields of view), KO, n = 14 (3), KO + WT, n = 17 (5), KO + D533A, n = 16 (4); fig. S5, BAK1 WT, n = 18 (5), KO, n = 18 (6), KO + WT, n = 35 (10), KO + D533A, n = 22 (9); fig. S6, SEC61β WT, n = 10 (3), SEC61β KO, n = 9 (3), BAK1 WT, n = 8 (3), BAK1 KO, n = 12 (3), OMP25 WT, n = 9 (3), OMP25 KO, n = 7 (3); fig. S8C, BAK1 WT cont., n = 16 (3), WT KD, n = 15 (5), KO cont., n = 25 (5), KO KD, n = 47 (10); fig. S8C, OMP25 WT cont., n = 11 (3), WT KD, n = 15 (3), KO cont., n = 14 (4), KO KD, n = 44 (10); Fig. 2G, endogenous OMP25 WT, n = 32 (10), KO, n = 32 (10), KO + WT, n = 19 (8), KO + D533A, n = 32 (10); and fig. S10F, endogenous RMDN3 WT, n = 30 (7), KO, n = 25 (7), KO + WT, n = 23 (10), KO + D533A, n = 25 (8).

To compare the level of IVT or stably expressed tail-anchored protein localized to mitochondria (fig. S7C), FLAG signal within mitochondrial ROIs was quantified from five (WT + IVT), four (KO + IVT; WT steady state), or three (KO steady state) different fields of view. Results were analyzed and plotted using GraphPad Prism software, and statistical significance was tested with unpaired two-tailed Student's t tests.

Miscellaneous biochemistry and analyses

SDS-PAGE was with 8%, 10%, or 12% Tris-tricine polyacrylamide gels with the Bio-Rad mini-gel electrophoresis system. Transfers to 0.2 μm nitrocellulose membranes and immunoblotting were performed using conventional techniques in 5% milk or BSA in PBS + 0.1% Tween and imaged on a BioRad ChemiDoc Touch or by exposure to XAR film. Transfers in 25 mM potassium phosphate (fig. S1C) (*51*) were at 15 V for 12 hours at 4°C. For autoradiography, gels were dried on filter paper before phosphor imaging or exposure to MR film. Quantification of autoradiography signal was done using phosphor imaging and ImageQuant software (GE Healthcare) or by scanning film and with ImageJ software (NIH). Native size fractionations on 200-μl 5 to 25% sucrose gradients (fig. S1A) were performed by centrifugation at 55,000 rpm for 2 hours 25 min in a TLS-55 rotor followed by manually collecting 11 fractions as described previously (*24*, *52*).

Classification of candidates identified by quantitative proteomics was initially analyzed by Gene Ontology (GO) enrichment terms and then by manually curating specific annotations in UniProt. Signal sequences were retrieved from UniProt or, for unclearly annotated candidates, predicted using SignalP-5.0. Experimentally validated eukaryotic signal sequences were extracted from SPdb (*53*), and proline content within the first 10 amino acids (fig. S10G) was analyzed using the Biostrings R package and R scripts. RNA extraction and quantitative real-time reverse transcription–PCR analyses (fig. S10D) were performed by Syd Labs, Inc. from frozen cell pellets using the following primers: MAVS forward, CAT GCT GGG CAG GTC AGT TA; MAVS reverse, TCA AAG CTA CCC TGG AAC GG; OMP25 forward, ACC CTC CAC CCC TGC TAT TC; OMP25 reverse, GGT TTG GGG TGG GTA TCA GTC; ATP13A1 forward, GTT CGT CGG CTT CAT TGT GG; ATP13A1 reverse, TGG GAC GCA TTC TGG ATC TC; SRP14 forward, ATT GGT CTG TGC TGC ATG GT; and SRP14 reverse, TGG GTT GGG AAA GGA ATA AAG AG. SRP14 and ATP13A1 were used as normalization and positive controls.

Purification of S. cerevisiae Spf1 for cryo-EM analysis

Yeast cells, in which endogenous Spf1 is tagged with C-terminal TEV-GFP, were grown in YPD medium (1% yeast extract, 2% peptone, and 2% glucose) in shaker flasks at 30°C to an OD_{600} of 2 to 4. Cells were harvested by centrifugation, frozen in liquid nitrogen, and stored at −80°C until use. Cells were lysed by cryomilling and resuspended in buffer containing 50 mM Tris (pH 7.5), 200 mM NaCl, 1 mM EDTA, 1 mM DTT, 10% glycerol, 5 μg/ml aprotinin, 5 μg/ml leupeptin, 1 μg/ml pepstatin A, and 2 mM PMSF. All subsequent steps were performed at 4°C. To purify apo Spf1, 1% n-dodecyl-β-D-maltopyranoside (DDM; Anatrace) and 0.2% cholesteryl hemisuccinate (CHS; Anatrace) were directly added to the cell lysate. After 3 hours of solubilization, the lysate was clarified by ultracentrifugation (Beckman Type 45 Ti rotor) at 120,000g for 1 hour, and the supernatant was mixed with Sepharose beads conjugated with anti-GFP nanobody for 2.5 hours. The beads were washed with ~30 column volumes of a wash buffer (buffer W) containing 20 mM Tris (pH 7.5), 100 mM NaCl, 1 mM EDTA, 1 mM DTT, 0.04% DDM, and 0.008% CHS. Spf1 was eluted by incubating the beads with ~10 μg/ml TEV protease (in buffer W) for ~14 hours. The eluate was concentrated and injected into a Superose 6 Increase column (GE Life Sciences) equilibrated with buffer W. Peak fractions were pooled and concentrated to ~5 mg/ml before cryo-EM grid preparation. For Spf1 bound to AMP-PCP, AlF_4, and BeF_3, the running buffer for size-exclusion chromatography additionally contained 10 mM $MgCl_2$, and the purified Spf1 was incubated with 2 mM of AMP-PCP, AlF_4, or BeF_3 for 1 hour at 4°C before grid preparation.

For the substrate-bound structure, the purification procedure was modified as follows. After cryomilling, unbroken cells and large debris were removed by centrifugation at 4000g for 10 min. Membranes were pelleted by ultracentrifugation (Beckman Type 45 Ti rotor) at 120,000g for 1.5 hours and resuspended in buffer containing 50 mM Tris (pH 7.5), 200 mM NaCl, 1 mM EDTA, 1 mM DTT, 10% glycerol, 2 mM BeF_3, 10 mM $MgCl_2$, 5 μg/ml aprotinin, 5 μg/ml leupeptin, 1 μg/ml pepstatin A, and 2 mM PMSF. The membranes were then solubilized with 1% DDM and 0.2% CHS for 2.5 hours. After clarification by ultracentrifugation, the lysate was incubated with anti-GFP nanobody beads for 3 hours. The beads were then washed with ~30 column volumes of buffer W additionally containing 10 mM $MgCl_2$ and 2 mM BeF_3. After eluting with the TEV protease, purified Spf1 was injected into a Superose 6 column equilibrated with the same wash buffer. Peak fractions were pooled, concentrated to ~5 mg/ml, and immediately used for cryo-EM grid preparation.

Cryo-EM grid preparation and data acquisition

To prepare cryo-EM grids, gold Quantifoil R 1.2/1.3 Holey Carbon Grids were treated with glow discharge for 35 s using a PELCO easiGlow system (0.39 mBar air, 25 mA). Then, 3 μl of the Spf1 sample were applied to a grid. The grid was blotted for 2 to 3 s with grade 1 Whatman filter paper and plunge-frozen in liquid nitrogen–cooled liquid ethane using Vitrobot Mark IV (FEI) operated at 4°C and 100% humidity.

The apo and AlF_4 datasets were collected on a Talos Arctica electron microscope (FEI) operated at an acceleration voltage of 200 kV, and the other datasets were collected on a Titan Krios electron microscope (FEI) operated at an acceleration voltage of 300 kV and equipped with a Gatan GIF Quantum LS image filter (a slit width of 20 eV) (table S1). Dose-fractionated images (~50 to 60 electrons per $Å^2$ over 42 frames) were recorded on a K3 direct electron detector (Gatan) operated in the superresolution mode using SerialEM software (*54*). The physical pixel size was 1.14 Å for apo, 0.90 Å for AlF_4, and 1.19 Å for the other datasets. Target defocus values were from −1.0 to −2.4 μm.

Cryo-EM structure determination

The single-particle analysis procedures are described in figs. S11D and S17, B and C, and table S1. First, tile-based motion correction of movies (using 7 by 5 tiles), contrast transfer function (CTF) estimation, and automatic particle picking were performed using Warp (*55*). During this process, the corrected movies were 2× frame binned by averaging each two frames, resulting in a total of 21 frames per movie. Micrographs that were not suitable for image analysis (mostly those containing crystalline ice) were removed by manual inspection. All subsequent image processing was performed using cryoSPARC v2 (*56*) with the particles and 2×-binned movies imported from Warp.

Except for the substrate-bound Spf1 dataset, the particles were polished by per-particle motion correction on the 2×-binned movies (57). The dimensions of extracted particle images were 256 pixels (320 pixels for the AlF_4 dataset). The particle images were then subjected to reference-free 2D classification. Most particles discarded by the 2D classification were empty detergent micelle particles. For the AlF_4 and BeF_3 datasets, the first 2D classification was performed before the particle polishing and another 2D classification after the polishing.

These particles were used for generation of three (for apo, AMP-PCP, and AlF_4) or five (for BeF_3- and substrate-bound Spf1) initial models (ab initio reconstruction), followed by one or two rounds of 3D classification (heterogeneous refinement). For the apo, AMP-PCP, and AlF_4 datasets, only one class (containing ~55 to 80% particles from the 2D classification) showed features of Spf1, which was used for 3D refinement. In the case of the BeF_3 dataset (without substrate), a minor class of the apo-like inward-open structure (23% particles) in addition to the major class of the outward-open structure (57% particles) was found in the 3D classification. In the case of the substrate-bound structure, three out of five classes (total 87% particles) showed equally clear Spf1 features with the outward-open conformation, whereas the two other minor classes showed little or no protein densities. All three good classes also showed a clear additional TM helix-like density of a putative endogenous substrate. Because substrate occupancy is likely partial, we subjected particles to a second round of 3D classification using two reference models, one of the three substrate-bound classes containing the substrate density and a class without a substrate (from the outward-open BeF_3-bound structure without a substrate). This resulted in two classes with a stronger (class A) and weaker (class B) substrate density, and particles from class A were used for 3D refinement. Particles from selected classes were refined to the final maps by CTF refinement and nonuniform refinement. The overall resolution was estimated on the basis of gold-standard Fourier shell correlation of independently refined half maps and the 0.143 cutoff criterion. Local resolution was estimated in cryoSPARC using default parameters (figs. S12A and S18, M to P). Unless indicated otherwise, the maps shown in figures were sharpened with B factors estimated in the nonuniform refinement and low-pass filtered at their resolution.

The initial atomic model was built de novo into the sharpened, low-pass–filtered combined map of the apo Spf1 using Coot (58). Models for the other structures were built using Coot after rigid-body fitting of individual domains (or groups of TMs) of the apo Spf1 structure into corresponding maps. The following segments were not modeled because they were invisible or poorly resolved in the density maps: N to 3, 45 to 54 (a loop between TMa and TMb), 646 to 652 (a loop in the N domain), 853 to 957 (the arm domain), and 1212 to C. In addition, the segments 562 to 571 (a part of the N domain), 842 to 852 (the arm domain), and 958 to 962 (the connection from the arm domain to the P domain) were modeled with alanine because we could not unambiguously register amino acids. Model refinement was done in real space using Phenix 1.16 (59), with the refinement resolution limit set to the overall resolution of the map. MolProbity (60) and EMRinger (61) in the Phenix package was used for structural validation (table S1). Protein electrostatics were calculated using the Adaptive Poisson-Boltzmann Solver (62, 63) with default parameters built in PyMOL v2.3 (with monovalent ion concentrations of 0.15 M each). Cavities were detected by Hollow (64). UCSF Chimera (65), Chimera X (66), and PyMOL (Schrödinger) were used to prepare the structural figures in the paper.

Sample preparation and digestion for MS

Protein extracts were subjected to disulfide bond reduction with 5 mM tris(2-carboxyethyl) phosphine (TCEP; room temperature, 10 min) and alkylation with 25 mM chloroacetamide (room temperature, 20 min) followed by methanol-chloroform precipitation (Fig. 2F and fig. S9) or trichloroacetic acid precipitation (Fig. 1C), before protease digestion. Samples were resuspended in 100 mM EPPS (pH 8.5) containing 0.1% RapiGest and digested at 37°C for 2 hours with LysC protease at a 200:1 protein-to-protease ratio. Trypsin was then added at a 100:1 protein-to-protease ratio, and the reaction was incubated for 6 hours at 37°C. TMT labeling of each sample was performed by adding indicated amount of the 20 ng/μl stock of TMT or TMTpro reagent along with acetonitrile to achieve a final acetonitrile concentration of ~30% (v/v). Typically, 5 μl of TMTpro reagent was added for 50 μg of protein input (Fig. 2F and fig. S9) and 3 μl of TMT reagent for affinity purification samples (Fig. 1C). After incubation at room temperature for 1 hour, labeling efficiency of a small aliquot was tested, and the reaction was then quenched with hydroxylamine to a final concentration of 0.5% (v/v) for 15 min. The TMT-labeled samples were pooled together at a 1:1 ratio. The sample was vacuum centrifuged to near dryness, resuspended in 5% formic acid for 15 min, centrifuged at 10,000*g* for 5 min at room temperature, and subjected to C18 solid-phase extraction (Sep-Pak, Waters).

For whole-proteome samples (Fig. 2F and fig. S9), dried TMT-labeled sample was resuspended in 100 μl of 10 mM NH_4HCO_3 (pH 8.0) and fractionated using basic pH reverse-phase high-performance liquid chromatography (HPLC) (67). Briefly, samples were offline fractionated over a 90-min run into 96 fractions by high pH reverse-phase HPLC (Agilent Technologies LC1260) through an aeris peptide xb-c18 column (Phenomenex; 250 mm × 3.6 mm) with mobile phase A containing 5% acetonitrile and 10 mM NH_4HCO_3 in liquid chromatography (LC)–MS grade H_2O, and mobile phase B containing 90% acetonitrile and 10 mM NH_4HCO_3 in LC-MS grade H_2O (both pH 8.0). The 96 resulting fractions were then pooled in a noncontinuous manner into 24 fractions [as outlined in supplementary figure 5 of (67)]. Fractions were vacuum centrifuged to near dryness. Each consolidated fraction was desalted by StageTip, dried again by vacuum centrifugation, and reconstituted in 5% acetonitrile (ACN), 1% formic acid (FA) for LC-MS/MS processing.

LC-MS/MS

For UV-cross-linking samples (Fig. 1C), MS data were collected using an Orbitrap Fusion Lumos mass spectrometer (Thermo Fisher Scientific) coupled to a Proxeon EASY-nLC1200 LC pump (Thermo Fisher Scientific). Peptides were separated on a 100-μm-inner-diameter microcapillary column packed in-house with ~35 cm of Accucore150 resin (2.6 μm, 150 Å, Thermo Fisher Scientific) with a gradient consisting of 5 to 22% (0 to 100 min), 22 to 28% (100 to 110 min) (ACN, 0.1% FA) over a total 120-min run at ~500 nl/min. Each analysis used the Multi-Notch MS^3-based TMT method (68) to reduce ion interference compared with MS^2 quantification, combined with newly implemented Real Time Search analysis software (69, 70). The scan sequence began with an MS^1 spectrum (Orbitrap analysis; resolution 120,000 at 200 Th; mass range 400 to 1400 m/z; automatic gain control (AGC) target 1×10^6; maximum injection time 240 ms). Precursors for MS^2 analysis were selected using a 3 s TopSpeed method. MS^2 analysis consisted of collision-induced dissociation [quadrupole ion trap analysis; rapid scan rate; AGC 2.5×10^4; isolation window 0.7 Th; normalized collision energy (NCE) 35; maximum injection time 60 ms]. Monoisotopic peak assignment was used, and previously interrogated precursors were excluded using a dynamic window (120 s ± 7 ppm). After acquisition of each MS^2 spectrum, a synchronous-precursor-selection (SPS) API-MS^3 scan was collected on the top 10 most intense ions b or y ions matched by the online search algorithm in the associated MS^2 spectrum (69, 70). MS^3 precursors were fragmented by high-energy collision-induced dissociation (HCD) and analyzed using the Orbitrap (NCE 65; AGC 2.5×10^5; maximum injection time 200 ms, resolution was 50,000 at 200 Th). Previously identified peptides corresponding to human SEC61B where included in a targeted mass list and given priority for MS^2 and SPS-MS^3.

For whole-cell proteome analysis (Fig. 2F and fig. S9), MS data were collected using an

Orbitrap Fusion Lumos mass spectrometer combined with a high-field asymmetric waveform ion mobility spectrometry (FAIMS) Pro interface, coupled to a Proxeon EASY-nLC1200 LC pump (Thermo Fisher Scientific). Peptides were separated on a 100-μm-inner-diameter microcapillary column packed in house with ~35 cm of Accucore150 resin (2.6 μm, 150 Å, Thermo Fisher Scientific) with a gradient consisting of 5 to 15% (0 to 70 min), 15 to 23% (70 to 85min) (ACN, 0.1% FA) over a total 95-min run at ~500 nl/min. For analysis, we loaded one-third of each fraction onto the column. To reduce ion interference compared with MS^2 quantification, each analysis used the Multi-Notch MS^3-based TMT method (*68*), combined with newly implemented Real Time Search analysis software (*69*, *70*) and the FAIMS Pro Interface. The scan sequence began with an MS^1 spectrum (Orbitrap analysis; resolution 120,000 at 200 Th; mass range 400 to 1600 m/z; AGC target 8×10^5; maximum injection time 50 ms). Precursors for MS^2 analysis were selected using a cycle type of 1.25 s/CV method [FAIMS CV = −40/−60/−80 previously optimized for TMT multiplexed samples (*71*)]. MS^2 analysis consisted of collision-induced dissociation (quadrupole ion trap analysis; rapid scan rate; AGC 1.0×10^4; isolation window 0.7 Th; NCE 35; maximum injection time 35 ms). Monoisotopic peak assignment and a precursor fit filter were used (70% for a fit window of 0.7 Th), and previously interrogated precursors were excluded using a dynamic window (120 s ± 10 ppm). After acquisition of each MS^2 spectrum, an SPS API-MS^3 scan was collected on the top 10 most intense ions b or y ions matched by the online search algorithm in the associated MS^2 spectrum (*69*, *70*). MS^3 precursors were fragmented by HCD and analyzed using the Orbitrap (NCE 45; AGC 2.5×10^5; maximum injection time 200 ms, resolution was 50,000 at 200 Th).

Proteomics data analysis

Mass spectra were processed using a Comet-based (v2018.01 rev.2) in-house software pipeline (*72*, *73*) or Sequest-HT (for Fig. 1C) using Proteome Discoverer (v2.3.0.420; Thermo Fisher Scientific).

The identification of UV-cross-linked proteins (Fig. 1C) was performed using the SEQUEST-HT engine (Proteome Discoverer v2.3.0.420; Thermo Fisher Scientific) against the UniProt *S. cerevisiae* (S288c) Reference Proteome (07/2017), as well as an in-house curated list of contaminants and the human SEC61B sequence, using the following parameters (after recalibration): a tolerance level of 10 ppm for MS^1 and 0.7 Da for MS^2 and false discovery rate (FDR) of the Percolator decoy database search was set to 1%. Trypsin and LysC were used as the digestion enzymes, two missed cleavages were allowed, and the minimal peptide length was set to seven amino acids. TMT tags on lysine residues and peptide N termini (+229.163 Da) and carbamidomethylation of cysteine residues (+57.021 Da) were set as static modifications, and oxidation of methionine residues (+15.995 Da) was set as a variable modification. For TMT-based reporter ion quantitation, we extracted (integration tolerance of 0.003 Da) the summed signal-to-noise ratio (S:N) for each TMT channel and found the closest matching centroid to the expected mass of the TMT reporter ion. For protein-level comparisons, peptide-spectrum matches (PSMs) were identified, quantified, and collapsed to a 1% peptide FDR, and then collapsed further to a final protein-level FDR of 1%. Moreover, protein assembly was guided by principles of parsimony to produce the smallest set of proteins necessary to account for all observed peptides. Proteins were quantified by summing reporter ion counts across all matching PSMs for specific peptides only. PSMs with poor quality, MS^3 spectra with TMT reporter summed S:Ns that were less than 10 per channel, isolation specificity ≤0.2, or had less than 70% of correctly selected SPS ions were excluded from quantification.

For whole-proteome analysis (Fig. 2F and fig. S9), spectra were converted to mzXML using a modified version of ReAdW.exe. Database searching included all canonical entries from the human Reference Proteome UniProt database (SwissProt 2019-01), as well as an in-house curated list of contaminants. This database was concatenated with one composed of all protein sequences in the reversed order. Trypsin was used as the digestion enzyme, two missed cleavages were allowed, and the minimal peptide length was set to seven amino acids. Searches were performed using a 20-ppm precursor ion tolerance for total protein-level analysis. The recommended product ion parameters for ion trap ms/ms were used (1.0005 tolerance, 0.4 offset (mono masses), theoretical_fragment_ions = 1). TMTpro tags on lysine residues and peptide N termini (+304.2071 Da) and carbamidomethylation of cysteine residues (+57.021 Da) were set as static modifications, whereas oxidation of methionine residues (+15.995 Da) was set as a variable modification. PSMs were adjusted to a 1% FDR, and PSM filtering was performed using a linear discriminant analysis, as described previously (*73*), while considering the following parameters: Comet Log Expect and Diff Seq. Delta Log Expect, missed cleavages, peptide length, charge state, and precursor mass accuracy. For TMT-based reporter ion quantitation, we extracted the summed S:N ratio for each TMT channel and found the closest matching centroid to the expected mass of the TMT reporter ion (integration tolerance of 0.003 Da). For protein-level comparisons, PSMs were identified, quantified, and collapsed to a 1% peptide FDR, and then collapsed further to a final protein-level FDR of 1%. Moreover, protein assembly was guided by principles of parsimony to produce the smallest set of proteins necessary to account for all observed peptides. Proteins were quantified by summing reporter ion counts across all matching PSMs using in-house software, as described previously (*73*). PSMs with poor quality, MS_3 spectra with more than 6 TMTpro reporter ion channels missing, or isolation specificity <0.6, or with TMT reporter summed S:Ns <200 or with no MS_3 spectra were excluded from quantification.

Protein quantification values were exported for further analysis in Microsoft Excel and Perseus (*74*), and statistical test and parameters used are indicated in the corresponding datasets (data S1 and S2). Briefly, Welch's *t* test analysis was performed to compare two datasets using the s0 parameter (in essence, a minimal fold change cutoff) and correction for multiple comparisons was achieved by the permutation-based FDR method, both functions that are built in in Perseus software. For whole-cell proteome (Fig. 2F and fig. S9) analysis, each reporter ion channel was summed across all quantified proteins and normalized assuming equal protein loading of all 16 samples. For affinity-purified samples (Fig. 1C), normalization based on SEC61B (total TMT sum S:N) was performed.

REFERENCES AND NOTES

1. E. A. Costa, K. Subramanian, J. Nunnari, J. S. Weissman, Defining the physiological role of SRP in protein-targeting efficiency and specificity. *Science* **359**, 689–692 (2018). doi: 10.1126/science.aar3607; pmid: 29348368
2. M. Gamerdinger, M. A. Hanebuth, T. Frickey, E. Deuerling, The principle of antagonism ensures protein targeting specificity at the endoplasmic reticulum. *Science* **348**, 201–207 (2015). doi: 10.1126/science.aaa5335; pmid: 25859040
3. U. S. Chio, H. Cho, S. O. Shan, Mechanisms of tail-anchored membrane protein targeting and insertion. *Annu. Rev. Cell Dev. Biol.* **33**, 417–438 (2017). doi: 10.1146/annurev-cellbio-100616-060839; pmid: 28992441
4. K. Krumpe *et al.*, Ergosterol content specifies targeting of tail-anchored proteins to mitochondrial outer membranes. *Mol. Biol. Cell* **23**, 3927–3935 (2012). doi: 10.1091/mbc.e11-12-0994; pmid: 22918956
5. M. Dyla, M. Kjaergaard, H. Poulsen, P. Nissen, Structure and mechanism of P-type ATPase ion pumps. *Annu. Rev. Biochem.* **89**, 583–603 (2019). doi: 10.1146/annurev-biochem-010611-112801; pmid: 31874046
6. J. P. Andersen *et al.*, P4-ATPases as phospholipid flippases: Structure, function, and enigmas. *Front. Physiol.* **7**, 275 (2016). doi: 10.3389/fphys.2016.00275; pmid: 27458383
7. D. M. Sørensen, M. J. Buch-Pedersen, M. G. Palmgren, Structural divergence between the two subgroups of P5 ATPases. *Biochim. Biophys. Acta* **1797**, 846–855 (2010). doi: 10.1016/j.bbabio.2010.04.010; pmid: 20416272
8. S. van Veen *et al.*, ATP13A2 deficiency disrupts lysosomal polyamine export. *Nature* **578**, 419–424 (2020). doi: 10.1038/s41586-020-1968-7; pmid: 31996848
9. D. M. Sørensen *et al.*, Parkinson disease related ATP13A2 evolved early in animal evolution. *PLOS ONE* **13**, e0193228 (2018). doi: 10.1371/journal.pone.0193228; pmid: 29505581
10. S. R. Cronin, R. Rao, R. Y. Hampton, Cod1p/Spf1p is a P-type ATPase involved in ER function and Ca2+ homeostasis. *J. Cell Biol.* **157**, 1017–1028 (2002). doi: 10.1083/jcb.200203052; pmid: 12058017

11. V. Dederer *et al*., Cooperation of mitochondrial and ER factors in quality control of tail-anchored proteins. *eLife* **8**, e45506 (2019). doi: 10.7554/eLife.45506; pmid: 31172943
12. C. Suzuki, Y. I. Shimma, P-type ATPase spf1 mutants show a novel resistance mechanism for the killer toxin SMKT. *Mol. Microbiol.* **32**, 813–823 (1999). doi: 10.1046/j.1365-2958.1999.01400.x; pmid: 10361284
13. D. M. Sørensen *et al*., The P5A ATPase Spf1p is stimulated by phosphatidylinositol 4-phosphate and influences cellular sterol homeostasis. *Mol. Biol. Cell* **30**, 1069–1084 (2019). doi: 10.1091/mbc.E18-06-0365; pmid: 30785834
14. S. R. Cronin, A. Khoury, D. K. Ferry, R. Y. Hampton, Regulation of HMG-CoA reductase degradation requires the P-type ATPase Cod1p/Spf1p. *J. Cell Biol.* **148**, 915–924 (2000). doi: 10.1083/jcb.148.5.915; pmid: 10704442
15. S. Vashist, C. G. Frank, C. A. Jakob, D. T. Ng, Two distinctly localized p-type ATPases collaborate to maintain organelle homeostasis required for glycoprotein processing and quality control. *Mol. Biol. Cell* **13**, 3955–3966 (2002). doi: 10.1091/mbc.02-06-0090; pmid: 12429838
16. A. Ando, C. Suzuki, Cooperative function of the CHD5-like protein Mdm39p with a P-type ATPase Spf1p in the maintenance of ER homeostasis in *Saccharomyces cerevisiae*. *Mol. Genet. Genomics* **273**, 497–506 (2005). doi: 10.1007/s00438-005-1153-6; pmid: 15909163
17. M. C. Jonikas *et al*., Comprehensive characterization of genes required for protein folding in the endoplasmic reticulum. *Science* **323**, 1693–1697 (2009). doi: 10.1126/science.1167983; pmid: 19325107
18. Y. Cohen *et al*., The yeast p5 type ATPase, spf1, regulates manganese transport into the endoplasmic reticulum. *PLOS ONE* **8**, e85519 (2013). doi: 10.1371/journal.pone.0085519; pmid: 24392018
19. C. Suzuki, Immunochemical and mutational analyses of P-type ATPase Spf1p involved in the yeast secretory pathway. *Biosci. Biotechnol. Biochem.* **65**, 2405–2411 (2001). doi: 10.1271/bbb.65.2405; pmid: 11791712
20. D. J. Tipper, C. A. Harley, Yeast genes controlling responses to topogenic signals in a model transmembrane protein. *Mol. Biol. Cell* **13**, 1158–1174 (2002). doi: 10.1091/mbc.01-10-0488; pmid: 11950929
21. D. M. Sørensen, H. W. Holen, T. Holemans, P. Vangheluwe, M. G. Palmgren, Towards defining the substrate of orphan P5A-ATPases. *Biochim. Biophys. Acta* **1850**, 524–535 (2015). doi: 10.1016/j.bbagen.2014.05.008; pmid: 24836520
22. S. Shao, R. S. Hegde, A calmodulin-dependent translocation pathway for small secretory proteins. *Cell* **147**, 1576–1588 (2011). doi: 10.1016/j.cell.2011.11.048; pmid: 22196732
23. A. Guna, N. Volkmar, J. C. Christianson, R. S. Hegde, The ER membrane protein complex is a transmembrane domain insertase. *Science* **359**, 470–473 (2018). doi: 10.1126/science.aao3099; pmid: 29242231
24. S. Shao, M. C. Rodrigo-Brenni, M. H. Kivlen, R. S. Hegde, Mechanistic basis for a molecular triage reaction. *Science* **355**, 298–302 (2017). doi: 10.1126/science.aah6130; pmid: 28104892
25. N. Wiedemann, N. Pfanner, Mitochondrial machineries for protein import and assembly. *Annu. Rev. Biochem.* **86**, 685–714 (2017). doi: 10.1146/annurev-biochem-060815-014352; pmid: 28301740
26. Y. C. Chen *et al*., Msp1/ATAD1 maintains mitochondrial function by facilitating the degradation of mislocalized tail-anchored proteins. *EMBO J.* **33**, 1548–1564 (2014). doi: 10.15252/embj.201487943; pmid: 24843043
27. C. U. Mårtensson *et al*., Mitochondrial protein translocation-associated degradation. *Nature* **569**, 679–683 (2019). doi: 10.1038/s41586-019-1227-y; pmid: 31118508
28. M. L. Wohlever, A. Mateja, P. T. McGilvray, K. J. Day, R. J. Keenan, Msp1 is a membrane protein dislocase for tail-anchored proteins. *Mol. Cell* **67**, 194–202.e6 (2017). doi: 10.1016/j.molcel.2017.06.019; pmid: 28712723
29. V. Okreglak, P. Walter, The conserved AAA-ATPase Msp1 confers organelle specificity to tail-anchored proteins. *Proc. Natl. Acad. Sci. U.S.A.* **111**, 8019–8024 (2014). doi: 10.1073/pnas.1405755111; pmid: 24821790
30. S. Matsumoto *et al*., Msp1 clears mistargeted proteins by facilitating their transfer from mitochondria to the ER. *Mol. Cell* **76**, 191–205.e10 (2019). doi: 10.1016/j.molcel.2019.07.006; pmid: 31445887
31. E. Park, T. A. Rapoport, Mechanisms of Sec61/SecY-mediated protein translocation across membranes. *Annu. Rev. Biophys.* **41**, 21–40 (2012). doi: 10.1146/annurev-biophys-050511-102312; pmid: 22224601
32. R. S. Hegde, H. D. Bernstein, The surprising complexity of signal sequences. *Trends Biochem. Sci.* **31**, 563–571 (2006). doi: 10.1016/j.tibs.2006.08.004; pmid: 16919958
33. C. Toyoshima, M. Nakasako, H. Nomura, H. Ogawa, Crystal structure of the calcium pump of sarcoplasmic reticulum at 2.6 A resolution. *Nature* **405**, 647–655 (2000). doi: 10.1038/35015017; pmid: 10864315
34. T. L. Sørensen, J. V. Møller, P. Nissen, Phosphoryl transfer and calcium ion occlusion in the calcium pump. *Science* **304**, 1672–1675 (2004). doi: 10.1126/science.1099366; pmid: 15192230
35. J. P. Morth *et al*., Crystal structure of the sodium-potassium pump. *Nature* **450**, 1043–1049 (2007). doi: 10.1038/nature06419; pmid: 18075585
36. K. Abe, K. Irie, H. Nakanishi, H. Suzuki, Y. Fujiyoshi, Crystal structures of the gastric proton pump. *Nature* **556**, 214–218 (2018). doi: 10.1038/s41586-018-0003-8; pmid: 29618813
37. M. Bublitz, H. Poulsen, J. P. Morth, P. Nissen, In and out of the cation pumps: P-type ATPase structure revisited. *Curr. Opin. Struct. Biol.* **20**, 431–439 (2010). doi: 10.1016/j.sbi.2010.06.007; pmid: 20634056
38. M. Timcenko *et al*., Structure and autoregulation of a P4-ATPase lipid flippase. *Nature* **571**, 366–370 (2019). doi: 10.1038/s41586-019-1344-7; pmid: 31243363
39. M. Hiraizumi, K. Yamashita, T. Nishizawa, O. Nureki, Cryo-EM structures capture the transport cycle of the P4-ATPase flippase. *Science* **365**, 1149–1155 (2019). doi: 10.1126/science.aay3353; pmid: 31416931
40. L. Bai *et al*., Autoinhibition and activation mechanisms of the eukaryotic lipid flippase Drs2p-Cdc50p. *Nat. Commun.* **10**, 4142 (2019). doi: 10.1038/s41467-019-12191-9; pmid: 31515475
41. K. G. Hansen *et al*., An ER surface retrieval pathway safeguards the import of mitochondrial membrane proteins in yeast. *Science* **361**, 1118–1122 (2018). doi: 10.1126/science.aar8174; pmid: 30213914
42. P. J. Chitwood, S. Juszkiewicz, A. Guna, S. Shao, R. S. Hegde, EMC is required to initiate accurate membrane protein topogenesis. *Cell* **175**, 1507–1519.e16 (2018). doi: 10.1016/j.cell.2018.10.009; pmid: 30415835
43. N. Volkmar, J. C. Christianson, Squaring the EMC: How promoting membrane protein biogenesis impacts cellular functions and organismal homeostasis. *J. Cell Sci.* **133**, jcs243519 (2020). doi: 10.1242/jcs.243519; pmid: 32332093
44. E. Itakura *et al*., Ubiquilins chaperone and triage mitochondrial membrane proteins for degradation. *Mol. Cell* **63**, 21–33 (2016). doi: 10.1016/j.molcel.2016.05.020; pmid: 27345149
45. J. W. Chin, A. B. Martin, D. S. King, L. Wang, P. G. Schultz, Addition of a photocrosslinking amino acid to the genetic code of *Escherichia coli*. *Proc. Natl. Acad. Sci. U.S.A.* **99**, 11020–11024 (2002). doi: 10.1073/pnas.172226299; pmid: 12154230
46. Z. Lin *et al*., TTC5 mediates autoregulation of tubulin via mRNA degradation. *Science* **367**, 100–104 (2020). doi: 10.1126/science.aaz4352; pmid: 31727855
47. Q. Feng, S. Shao, In vitro reconstitution of translational arrest pathways. *Methods* **137**, 20–36 (2018). doi: 10.1016/j.ymeth.2017.12.018; pmid: 29277545
48. F. A. Ran *et al*., Genome engineering using the CRISPR-Cas9 system. *Nat. Protoc.* **8**, 2281–2308 (2013). doi: 10.1038/nprot.2013.143; pmid: 24157548
49. N. Otsu, A threshold selection method from gray-level histograms. *IEEE Trans. Syst. Man Cybern.* **9**, 62–66 (1979). doi: 10.1109/TSMC.1979.4310076
50. E. M. M. Manders, F. J. Verbeek, J. A. Aten, Measurement of co-localization of objects in dual-colour confocal images. *J. Microsc.* **169**, 375–382 (1993). doi: 10.1111/j.1365-2818.1993.tb03313.x
51. M. T. Hincke, Conditions for improved adsorption of calmodulin to nitrocellulose: Detection by 45Ca binding. *Electrophoresis* **9**, 303–306 (1988). doi: 10.1002/elps.1150090704; pmid: 3234368
52. M. C. J. Yip *et al*., Mechanism for recycling tRNAs on stalled ribosomes. *Nat. Struct. Mol. Biol.* **26**, 343–349 (2019). doi: 10.1038/s41594-019-0211-4; pmid: 31011209
53. K. H. Choo, T. W. Tan, S. Ranganathan, SPdb: A signal peptide database. *BMC Bioinformatics* **6**, 249 (2005). doi: 10.1186/1471-2105-6-249; pmid: 16221310
54. D. N. Mastronarde, Automated electron microscope tomography using robust prediction of specimen movements. *J. Struct. Biol.* **152**, 36–51 (2005). doi: 10.1016/j.jsb.2005.07.007; pmid: 16182563
55. D. Tegunov, P. Cramer, Real-time cryo-electron microscopy data preprocessing with Warp. *Nat. Methods* **16**, 1146–1152 (2019). doi: 10.1038/s41592-019-0580-y; pmid: 31591575
56. A. Punjani, J. L. Rubinstein, D. J. Fleet, M. A. Brubaker, cryoSPARC: Algorithms for rapid unsupervised cryo-EM structure determination. *Nat. Methods* **14**, 290–296 (2017). doi: 10.1038/nmeth.4169; pmid: 28165473
57. J. L. Rubinstein, M. A. Brubaker, Alignment of cryo-EM movies of individual particles by optimization of image translations. *J. Struct. Biol.* **192**, 188–195 (2015). doi: 10.1016/j.jsb.2015.08.007; pmid: 26296328
58. P. Emsley, B. Lohkamp, W. G. Scott, K. Cowtan, Features and development of Coot. *Acta Crystallogr. D Biol. Crystallogr.* **66**, 486–501 (2010). doi: 10.1107/S0907444910007493; pmid: 20383002
59. P. V. Afonine *et al*., Real-space refinement in PHENIX for cryo-EM and crystallography. *Acta Crystallogr. D Struct. Biol.* **74**, 531–544 (2018). doi: 10.1107/S2059798318006551; pmid: 29872004
60. V. B. Chen *et al*., MolProbity: All-atom structure validation for macromolecular crystallography. *Acta Crystallogr. D Biol. Crystallogr.* **66**, 12–21 (2010). doi: 10.1107/S0907444909042073; pmid: 20057044
61. B. A. Barad *et al*., EMRinger: Side chain-directed model and map validation for 3D cryo-electron microscopy. *Nat. Methods* **12**, 943–946 (2015). doi: 10.1038/nmeth.3541; pmid: 26280328
62. N. A. Baker, D. Sept, S. Joseph, M. J. Holst, J. A. McCammon, Electrostatics of nanosystems: Application to microtubules and the ribosome. *Proc. Natl. Acad. Sci. U.S.A.* **98**, 10037–10041 (2001). doi: 10.1073/pnas.181342398; pmid: 11517324
63. T. J. Dolinsky, J. E. Nielsen, J. A. McCammon, N. A. Baker, PDB2PQR: An automated pipeline for the setup of Poisson-Boltzmann electrostatics calculations. *Nucleic Acids Res.* **32** (Web Server), W665-7 (2004). doi: 10.1093/nar/gkh381; pmid: 15215472
64. B. K. Ho, F. Gruswitz, HOLLOW: Generating accurate representations of channel and interior surfaces in molecular structures. *BMC Struct. Biol.* **8**, 49 (2008). doi: 10.1186/1472-6807-8-49; pmid: 19014592
65. E. F. Pettersen *et al*., UCSF Chimera: A visualization system for exploratory research and analysis. *J. Comput. Chem.* **25**, 1605–1612 (2004). doi: 10.1002/jcc.20084; pmid: 15264254
66. T. D. Goddard *et al*., UCSF ChimeraX: Meeting modern challenges in visualization and analysis. *Protein Sci.* **27**, 14–25 (2018). doi: 10.1002/pro.3235; pmid: 28710774
67. J. A. Paulo *et al*., Quantitative mass spectrometry-based multiplexing compares the abundance of 5000 S. cerevisiae proteins across 10 carbon sources. *J. Proteomics* **148**, 85–93 (2016). doi: 10.1016/j.jprot.2016.07.005; pmid: 27432472
68. G. C. McAlister *et al*., MultiNotch MS3 enables accurate, sensitive, and multiplexed detection of differential expression across cancer cell line proteomes. *Anal. Chem.* **86**, 7150–7158 (2014). doi: 10.1021/ac502040v; pmid: 24927332
69. B. K. Erickson *et al*., Active instrument engagement combined with a real-time database search for improved performance of sample multiplexing workflows. *J. Proteome Res.* **18**, 1299–1306 (2019). doi: 10.1021/acs.jproteome.8b00899; pmid: 30658528
70. D. K. Schweppe *et al*., Full-featured, real-time database searching platform enables fast and accurate multiplexed quantitative proteomics. *J. Proteome Res.* **19**, 2026–2034 (2020). doi: 10.1021/acs.jproteome.9b00860; pmid: 32126768
71. D. K. Schweppe *et al*., Characterization and optimization of multiplexed quantitative analyses using high-field asymmetric-waveform ion mobility mass spectrometry. *Anal. Chem.* **91**, 4010–4016 (2019). doi: 10.1021/acs.analchem.8b05399; pmid: 30672687
72. J. K. Eng, T. A. Jahan, M. R. Hoopmann, Comet: An open-source MS/MS sequence database search tool. *Proteomics* **13**, 22–24 (2013). doi: 10.1002/pmic.201200439; pmid: 23148064
73. E. L. Huttlin *et al*., A tissue-specific atlas of mouse protein phosphorylation and expression. *Cell* **143**, 1174–1189 (2010). doi: 10.1016/j.cell.2010.12.001; pmid: 21183079
74. S. Tyanova *et al*., The Perseus computational platform for comprehensive analysis of (prote)omics data. *Nat. Methods* **13**, 731–740 (2016). doi: 10.1038/nmeth.3901; pmid: 27348712

ACKNOWLEDGMENTS

We thank D. Toso and J. Remis for electron microscope operational support; the Nikon Imaging Center at HMS for training and

support; C. Yapp at the Image and Data Analysis (IDAC) core at HMS and M. Hoyer for help with colocalization analysis; M. C. J. Yip for help generating reagents; the R. S. Hegde laboratory for mammalian Bpa suppression constructs; S. Klinge for the yeast integration plasmid; S. Elsasser, K. Y. S. Hung, and the D. Finley laboratory for advice and yeast strains; J. A. Paulo for proteomics support; T. A. Rapoport and R. S. Hegde for critical reading of the manuscript; and Shao and Park laboratory members for discussions. **Funding:** This work was supported by the American Heart Association (grant no. 19POST34400009 to M.J.M.), the CRSP of HMS Department of Cell Biology (L.W.), NIH grant nos. R37NS083524 and RO1NS110395 (J.W.H), NIH grant no. DP2GM137415 (S.S.), the Smith Family Foundation (S.S.), a Packard fellowship (S.S.), and the Vallee Scholars Program (S.S., E.P.). **Author contributions:** S.I.S. prepared cryo-EM samples; S.I.S. and E.P. collected and analyzed cryo-EM data; E.P. built atomic models of Spf1; M.J.M. and S.S. performed biochemical experiments; M.J.M., L.W., and S.S. generated cell lines; M.J.M. performed all IF experiments; A.O. performed all TMT-MS analysis under the supervision of J.W.H.; and S.S. and E.P. supervised the project and wrote the paper with input from all authors. **Competing interests:** J.W.H. is a founder and advisory board member for Caraway Therapeutics, an adviser for X-Chem Inc., a reviewing editor for Elife, and an associate editor for *Science Advances*. **Data and materials availability:** EM maps and models are available through EM Data Bank (EMDB) and the Protein Data Bank (PDB) under the following accession codes: EMD-22260 and PDB ID 6XMP for apo Spf1; EMD-22261 and 6XMQ for AMP-PCP–bound Spf1; EMD-22262 and 6XMS for AlF_4-bound Spf1; EMD-22263 and 6XMT for BeF_3-bound Spf1; and EMD-22264 and 6XMU for BeF_3/endogenous substrate-bound Spf1. Renewable yeast strains, cell lines, and biochemical reagents are available by contacting E.P. or S.S.

SUPPLEMENTARY MATERIALS

science.sciencemag.org/content/369/6511/eabc5809/suppl/DC1
Figs. S1 to S20
Table S1
Movies S1 to S3
Data S1 to S2
MDAR Reproducibility Checklist

View/request a protocol for this paper from *Bio-protocol*.

1 May 2020; accepted 28 July 2020
10.1126/science.abc5809

Science

The endoplasmic reticulum P5A-ATPase is a transmembrane helix dislocase

Michael J. McKenna, Sue Im Sim, Alban Ordureau, Lianjie Wei, J. Wade Harper, Sichen Shao and Eunyong Park

Science **369** (6511), eabc5809.
DOI: 10.1126/science.abc5809

Dissecting membrane dislocation

Mistargeting and misinsertion of membrane proteins causes proteostasis stress and dysfunction of intracellular organelles, which can lead to disease. McKenna *et al.* found that a conserved orphan P-type adenosine triphosphatase (ATPase) transporter removes misinserted transmembrane segments from the endoplasmic reticulum (ER). Functional reconstitutions and cryo–electron microscopy structures show how this ATPase selectively extracts mitochondrial proteins that are mistargeted to the ER and transmembrane segments that are inserted in the wrong orientation. This work identifies polypeptides as a new class of P-type ATPase substrates and defines a new protein quality-control mechanism at the ER.

Science, this issue p. eabc5809

Science (print ISSN 0036-8075; online ISSN 1095-9203) is published by the American Association for the Advancement of Science, 1200 New York Avenue NW, Washington, DC 20005. The title *Science* is a registered trademark of AAAS.

science.sciencemag.org/content/369/6511/eabc5809/suppl/DC1

Supplementary Materials for

The endoplasmic reticulum P5A-ATPase is a transmembrane helix dislocase

Michael J. McKenna*, Sue Im Sim*, Alban Ordureau, Lianjie Wei, J. Wade Harper, Sichen Shao†, Eunyong Park†

*These authors contributed equally to this work.
†Corresponding author. E-mail: sichen_shao@hms.harvard.edu (S.S.); eunyong_park@berkeley.edu (E.P.)

Published 25 September 2020, *Science* **369**, eabc5809 (2020)
DOI: 10.1126/science.abc5809

This PDF file includes:

Figs. S1 to S20
Table S1
Captions for Movies S1 to S3
Captions for Data S1 and S2

Other Supplementary Material for this manuscript includes the following:
(available at science.sciencemag.org/content/369/6511/eabc5809/suppl/DC1) [for online-only papers]

Movies S1 to S3 (mp4 files)
Data S1 and S2 (Excel files)
MDAR Reproducibility Checklist (PDF)

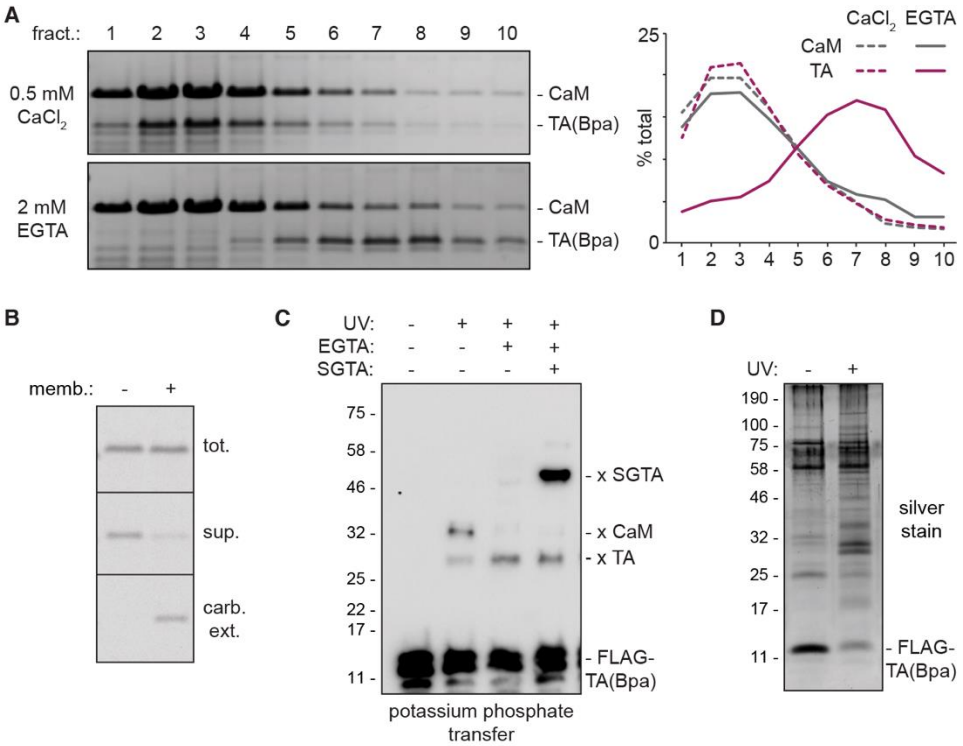

Fig. S1. Validation of components to identify direct interactors of mitochondrial TA proteins.

(**A**) Recombinant TA protein containing Bpa in the OMP25 TM [TA(Bpa)] was purified in complex with calmodulin (CaM) in the presence of 0.5 mM $CaCl_2$. The complexes were maintained in 0.5 mM $CaCl_2$ (top) or adjusted to 2 mM EGTA (bottom) and fractionated by native size on a 5-25% sucrose gradient. Individual fractions collected from the top of the gradient were analyzed by SDS-PAGE and Coomassie staining. Distributions of CaM (gray) and TA(Bpa) (purple) with $CaCl_2$ (dotted lines) or EGTA (solid lines) were quantified and plotted (right). EGTA dissociates TA(Bpa) from CaM, leading to TA(Bpa) aggregates that migrate deeper into the gradient. (**B**) *In vitro* translated radiolabeled TA protein containing the OMP25 TM was post-translationally incubated with crude yeast membranes. Reactions were analyzed by autoradiography directly (tot.), after centrifugation to isolate soluble proteins (sup.), or after carbonate extraction (carb. ext.) to detect membrane-inserted TA protein. (**C**) Reactions as in Fig. 1B with SGTA were analyzed by immunoblotting for FLAG-TA(Bpa) after a wet transfer in 25 mM potassium phosphate buffer, which enhances the transfer of CaM to nitrocellulose membranes. UV-dependent FLAG-TA(Bpa) crosslinks to CaM (x CaM) and SGTA (x SGTA) are indicated. (**D**) Silver staining of representative affinity purified FLAG-TA(Bpa) released in the presence of yeast membranes before (left lane) and after (right lane) UV irradiation.

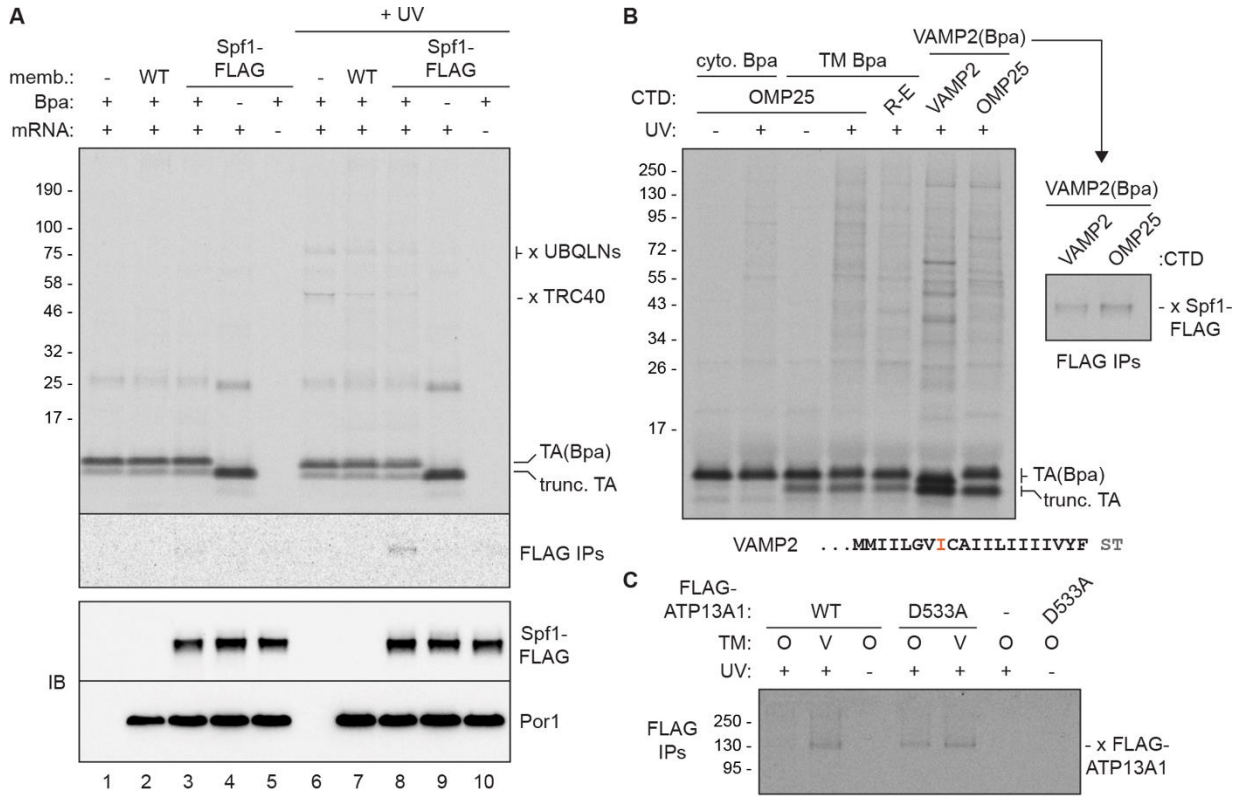

Fig. S2. Validation of P5A-ATPase interaction with TA proteins.

(**A**) *In vitro* translation reactions of radiolabeled TA(Bpa) without or with TA-encoding mRNA or Bpa incorporation factors were incubated with crude yeast membranes (memb.) containing untagged (WT) or FLAG-tagged Spf1. Reactions before (lanes 1-5) and after UV exposure (lanes 6-10) were subject to denaturing immunoprecipitations for TA(Bpa) (top) or Spf1-FLAG (middle) and analyzed by autoradiography. Bottom panel shows immunoblots (IB) of Spf1-FLAG and Por1. Full-length TA(Bpa), truncated (trunc.) non-suppressed TA protein, and known cytosolic crosslinking partners of TA proteins (x TRC40, x UBQLNs - ubiquilins) are indicated. TA crosslinking to Spf1-FLAG is detected only with Bpa incorporation, UV irradiation, and when Spf1 is FLAG-tagged (lane 8). (**B**) Darker exposure of totals gel in Fig. 1E showing UV-dependent interactions. Crosslinking of Spf1-FLAG to the ER-targeted VAMP2 TM is enhanced by the OMP25 C-terminal domain (CTD) containing positively charged residues (right). TM (black), Bpa placement (orange) and CTD (gray) sequence of VAMP2 is below. The more hydrophobic VAMP2 TM engages ATP13A1 but is not extracted (see fig. S3B), which may partially explain stronger crosslinking to Spf1. (**C**) Photocrosslinking and denaturing FLAG IPs of radiolabeled TA protein with the OMP25 (O) or VAMP2 (V) TM and OMP25 CTD incubated with ER-derived rough microsomes (RMs) from HEK293T cells overexpressing wildtype (WT) or catalytically inactive (D533A) FLAG-tagged ATP13A1. Crosslinking to FLAG-ATP13A1 is UV-dependent and stronger with D533A FLAG-ATP13A1, indicating that the interaction is stabilized when ATP13A1 transport function is inactive.

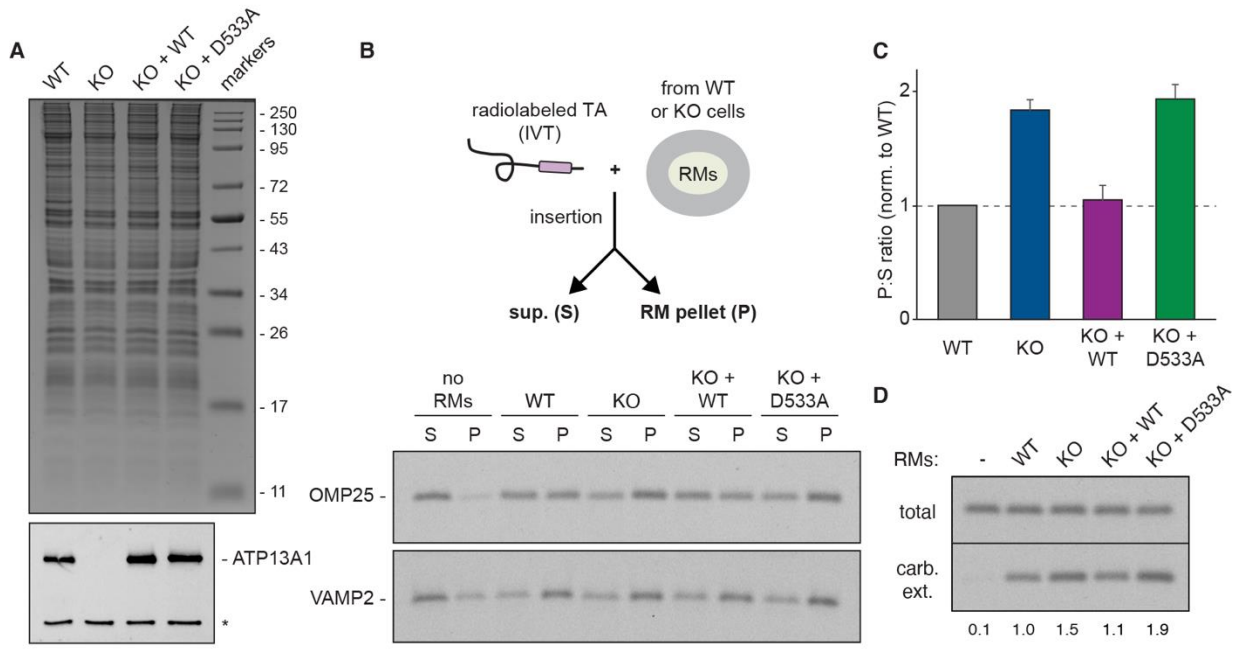

Fig. S3. Cell-free assays of TM insertion into ER with and without ATP13A1.

(**A**) Coomassie stain (top) and ATP13A1 immunoblots (bottom) of rough microsomes (RMs) isolated from wildtype (WT), ATP13A1 knockout (KO), or KO Flp-In T-REx 293 cells stably re-expressing WT or D533A FLAG-tagged ATP13A1. FLAG-ATP13A1 expression behind an inducible promoter was maintained by low tetracycline levels present in the culture media. Asterisk denotes background band. (**B**) Scheme (top) and autoradiography (bottom) of insertion reactions of *in vitro* translated (IVT) radiolabeled TA protein containing the mitochondrial OMP25 (top panel) or ER-targeted VAMP2 (bottom panel) TM with the indicated RMs. Centrifugation separates the soluble cytosolic supernatant (sup.; S) and RM pellet (P) fractions. Note that the ratio of OMP25, but not of VAMP2, in S vs. P fractions changes depending on the presence of wildtype ATP13A1 activity. **(C)** Mean + s.e.m of the P:S ratio of OMP25 intensity normalized to WT RMs for 3 independent experiments as in (B). OMP25 preferentially accumulates in RMs lacking functional ATP13A1. (**D**) Reactions (total) of OMP25 as in (B) were subjected to carbonate extraction to detect membrane-inserted TMs. Pelleted TA protein signal after carbonate extraction (carb. ext.) normalized to WT RM values are below.

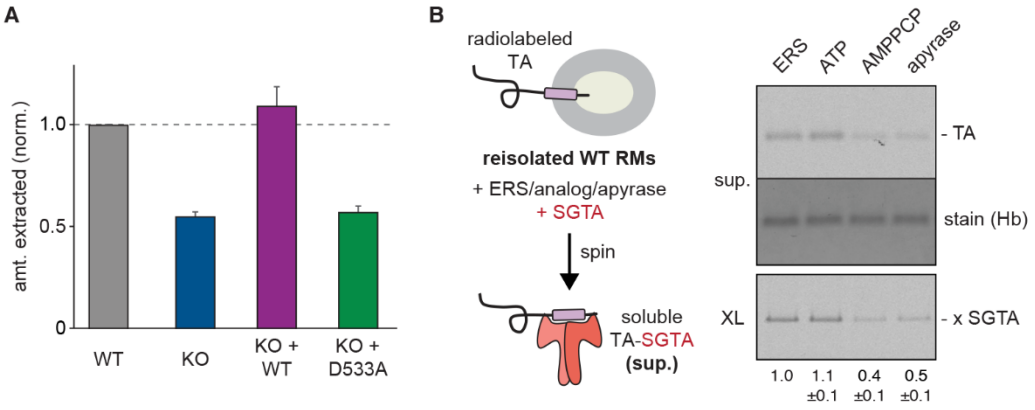

Fig. S4. Cell-free assays of ATP13A1 function in TM extraction.

(A) Mean + s.e.m. of the intensity of soluble OMP25 in 3 independent extraction assays as in Fig. 2B normalized to wildtype (WT) RM values. (**B**) Scheme (left) and autoradiography (right) of extraction assays of radiolabeled OMP25 from WT RMs with the TM chaperone SGTA and either an energy regenerating system (ERS), 1 mM ATP, 1 mM AMP-PCP, or 0.1 U/µL apyrase. Reactions were centrifuged over a 20% sucrose cushion to separate soluble extracted TA protein (sup.; top), followed by BMH crosslinking (XL; bottom) to detect TA protein crosslinks to SGTA (x SGTA). Residual hemoglobin (Hb) from the translation extract is a loading and recovery control. Mean +/- s.e.m. values of the intensity of soluble OMP25 normalized to the reaction containing ERS for 3 independent experiments are below. Note that AMP-PCP and apyrase inhibits TA protein dislocation.

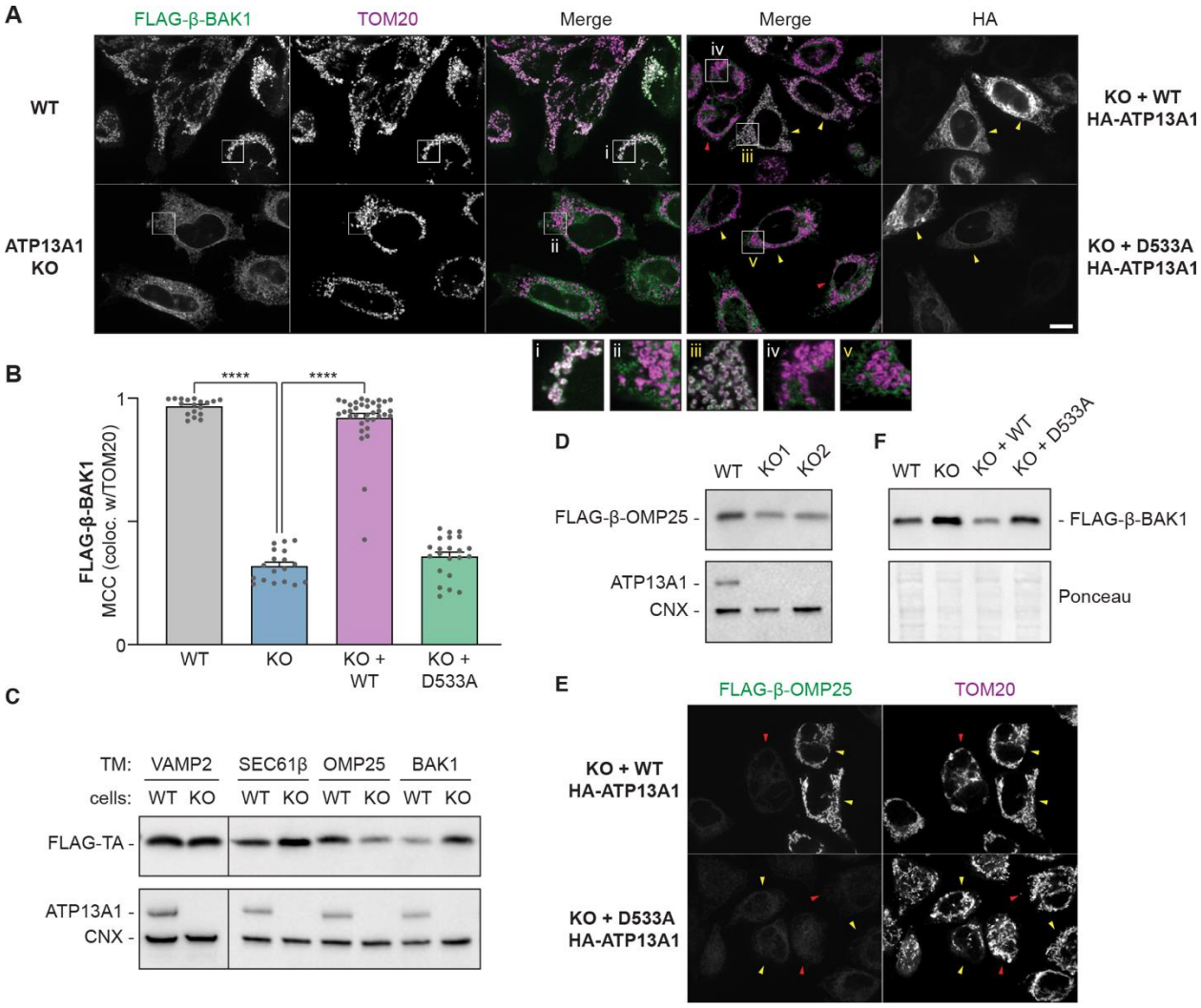

Fig. S5. Mitochondrial TA protein localization and levels in ATP13A1 knockout cells.

(**A**) Immunofluorescence of FLAG-β-BAK1 (green), the mitochondrial marker TOM20 (purple), and HA-tagged ATP13A1 in wildtype (WT) or ATP13A1 knockout (KO) Flp-In T-REx HeLa cells without (left) or with transfection of WT or D533A HA-ATP13A1 (right). Mislocalization of BAK1 in ATP13A1 KO cells is rescued by WT but not D533A HA-ATP13A1 (yellow arrowheads). Red arrowheads indicate untransfected cells. Scale bar, 10 µm. High magnification views of corresponding boxed regions are below. **(B)** Mean + s.e.m. and individual Manders' colocalization coefficient (MCC) values of FLAG-β-BAK1 colocalization with TOM20 in the indicated cells. **** $p<0.0001$. (**C** and **D**) Immunoblotting for FLAG-tagged TA protein reporters with the indicated TM expressed in WT or ATP13A1 KO cells (top). Blots for ATP13A1 and calnexin (CNX) delineate KO cells and loading controls. Note that OMP25 levels decrease, while BAK1 levels increase, in ATP13A1 KO cells. **(E)** Single channel FLAG-β-OMP25 and TOM20 immunofluorescence images of rescue experiments in Fig. 2D. **(F)** Immunoblotting (top) and Ponceau staining (bottom) of WT or ATP13A1 KO cells stably expressing FLAG-β-BAK1 without or with transfection of WT or D533A HA-ATP13A1.

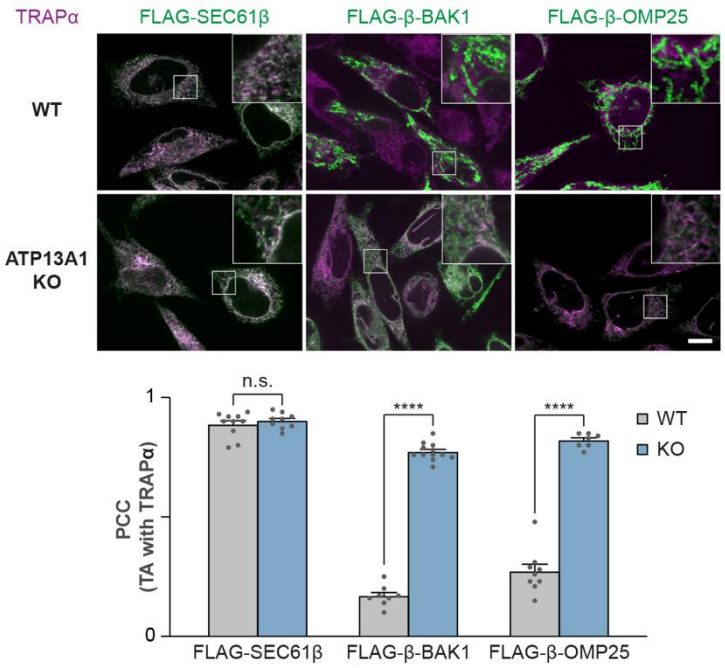

Fig. S6. TA protein localization to the ER.

Immunofluorescence (top) of the ER-targeted TA protein reporter FLAG-SEC61β (green), the mitochondrial TA protein reporters FLAG-β-BAK1 or FLAG-β-OMP25 (green), and the ER marker TRAPα (purple) in wildtype (WT) and ATP13A1 knockout (KO) Flp-In T-REx HeLa cells. Scale bar, 10 µm. Insets show high magnification views of boxed regions. Mean + s.e.m. and individual Pearson's colocalization coefficient (PCC) values (per cell) of the correlation of the indicated TA protein reporter with TRAPα signals in WT and ATP13A1 knockout (KO) cells are below. n.s. – not significant; **** $p<0.0001$.

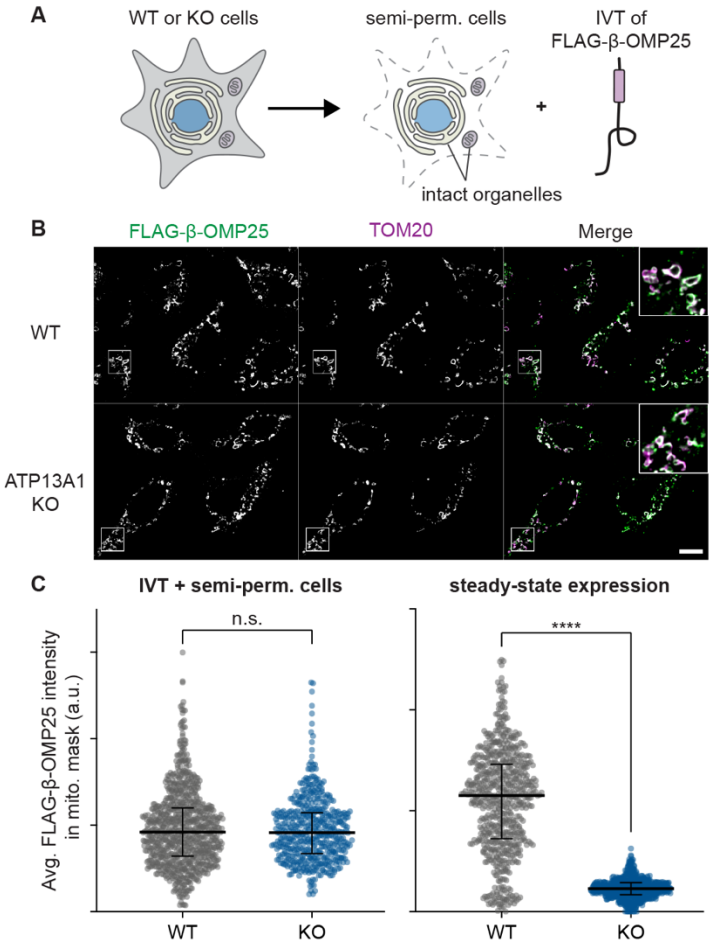

Fig. S7. TA protein targeting in semi-permeabilized cells.

(**A**) Scheme to assay initial TA protein targeting. Wildtype (WT) or ATP13A1 knockout (KO) Flp-In T-REx HeLa cells were semi-permeabilized (semi-perm.) with 200 µg/mL digitonin, which selectively solubilizes the plasma membrane without disrupting organellar membranes. Semi-perm. cells were incubated with *in vitro* translation (IVT) reactions of a FLAG-tagged model TA protein containing the mitochondrial OMP25 TM (FLAG-β-OMP25) for 15 min, washed to remove non-targeted FLAG-β-OMP25, and analyzed by immunofluorescence. (**B**) Immunofluorescence of experiments as in (A) of FLAG-β-OMP25 (green) and the mitochondrial marker TOM20 (purple). Scale bar, 10 µm. Insets show high magnification views of boxed regions. (**C**) Average background-subtracted FLAG-β-OMP25 immunofluorescence signal within mitochondrial regions defined by TOM20 signal were plotted to show the extent of mitochondrial localization of IVT FLAG-β-OMP25 in WT (gray) and ATP13A1 KO (blue) semi-perm. cells as in (B) (left), or of FLAG-β-OMP25 stably expressed in WT and KO cells as in Fig. 2D (right). Shown are median, interquartile range, and individual values for n = 831 (IVT + WT), 510 (IVT + KO), 676 (WT), and 686 (KO) measurements. n.s. – not significant; **** $p<0.0001$. Note that initial targeting of IVT FLAG-β-OMP25 to mitochondria is not impaired by ATP13A1 KO, even though FLAG-β-OMP25 is depleted from mitochondrial in ATP13A1 KO cells at steady state.

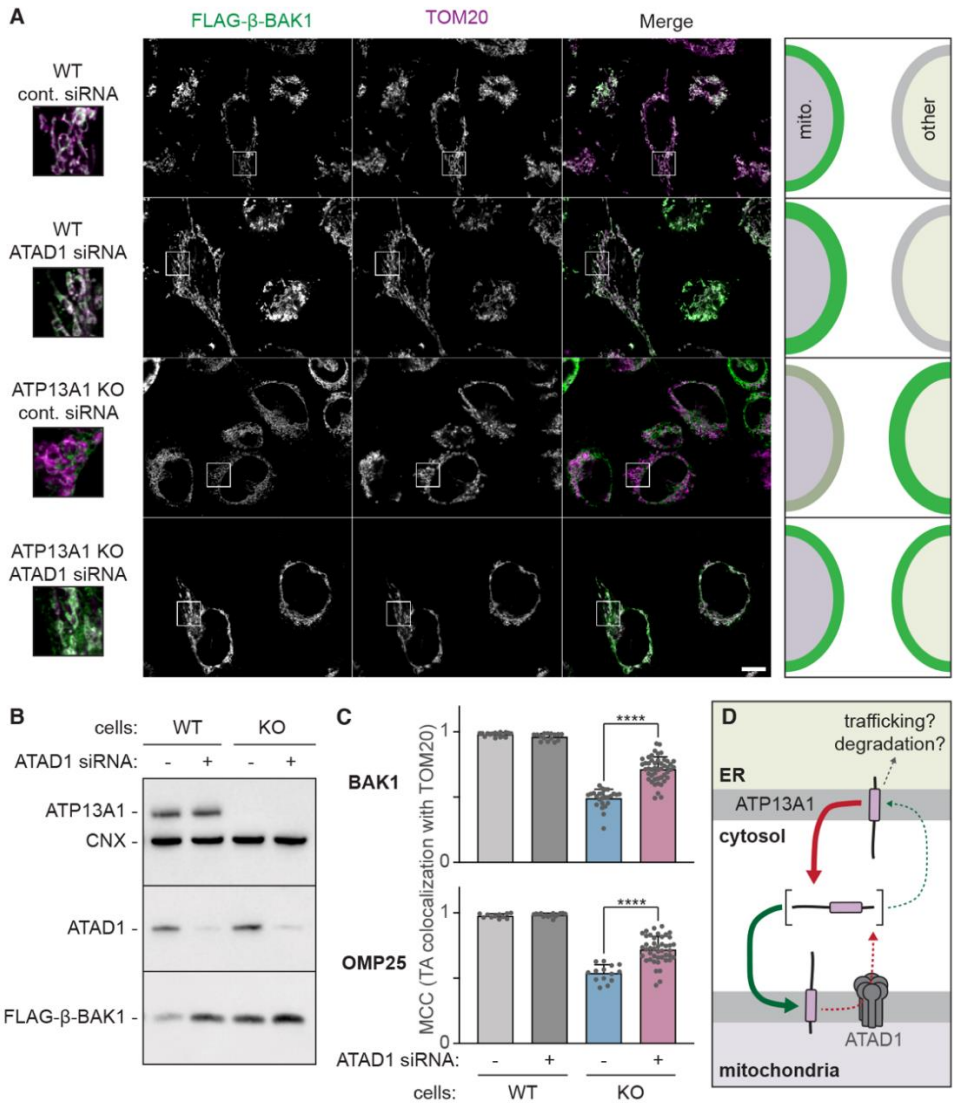

Fig. S8. Contributions of ATP13A1 and ATAD1 to TA protein localization.

(**A**) Immunofluorescence of FLAG-β-BAK1 (green) and the mitochondrial marker TOM20 (purple) in wildtype (WT) or ATP13A1 knockout (KO) Flp-In T-REx HeLa cells treated with control (cont.) or ATAD1-targeting siRNAs. Scale bar, 10 µm. High magnification views (left) and models of FLAG-β-BAK1 localization (green) to mitochondria (mito.) and the ER or other secretory pathway organelles (right) are shown. ATAD1 knockdown increases FLAG-β-BAK1 localization to mitochondria in ATP13A1 KO cells (bottom 2 rows). Note that we analyzed FLAG-β-BAK1 because it is not destabilized in ATP13A1 KO cells (see fig. S5). (**B**) Immunoblotting of cells from (A). CNX – calnexin. (**C**) Mean + s.e.m. and individual Manders' correlation coefficient (MCC) values of TA protein colocalization with TOM20 in the indicated cells expressing either the BAK1 (top) or OMP25 (bottom) reporter. **** $p<0.0001$. (**D**) Proposed model for how independent ATP13A1 and ATAD1 TM removal functions cooperate to determine TA protein localization at steady state. Normally, mitochondrial TA protein targeting to mitochondria and ATP13A1-mediated extraction from the ER are likely preferred. In ATP13A1 KO cells, misinserted mitochondrial TMs accumulate at the ER, where they may undergo further trafficking into the secretory pathway and lysosomal or ER-associated degradation. In this model, ATAD1-mediated extraction likely contributes to TA protein depletion from mitochondria at steady state in ATP13A1 KO cells.

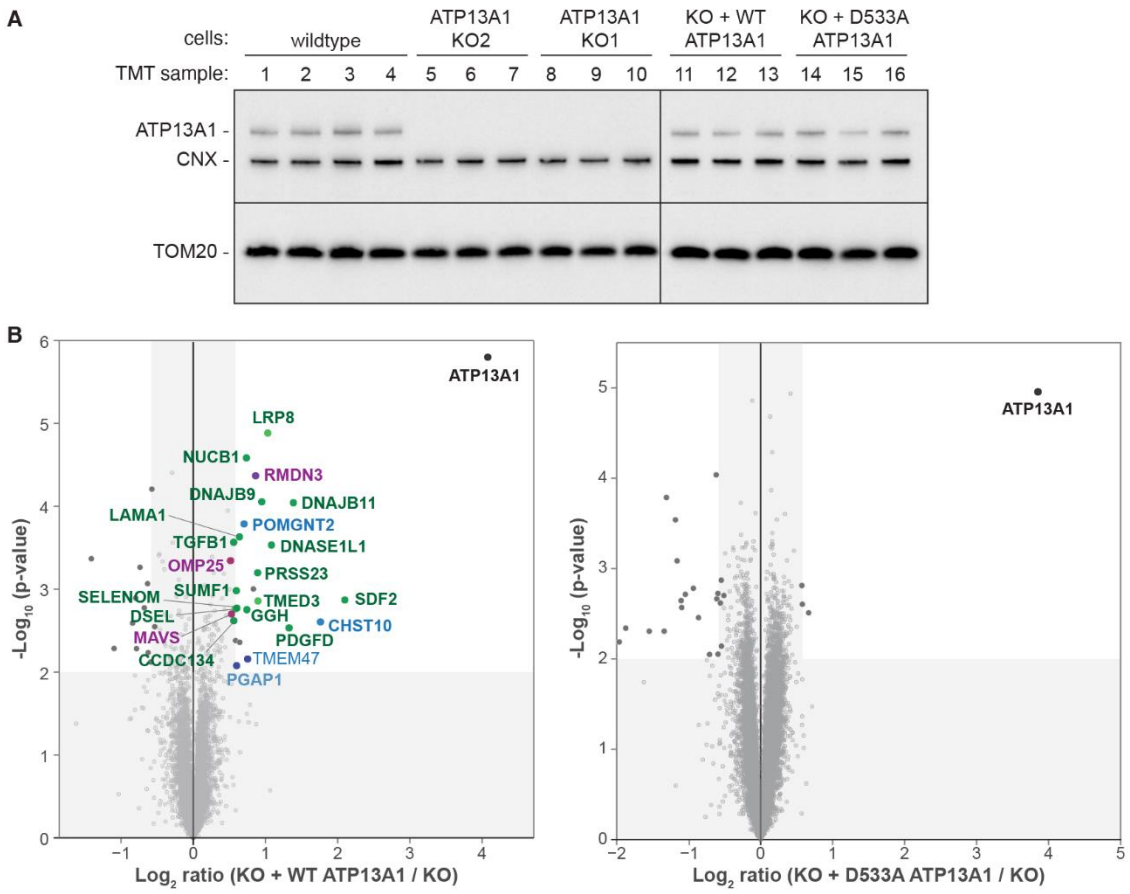

Fig. S9. Multiplexed quantitative proteomics of wildtype and D533A ATP13A1 cells.

(**A**) Wildtype (WT), two ATP13A1 knockout (KO), and ATP13A1 KO1 Flp-In T-REx HeLa cell lines with WT or D533A FLAG-tagged ATP13A1 stably integrated behind a doxycycline-inducible truncated CMV*d*1 promoter were cultured with 100 ng/mL doxycycline for 48 hr. Triplicate lysate samples of each cell line prepared for TMT-MS^3 were analyzed by SDS-PAGE and immunoblotting. CNX – calnexin. (**B**) Volcano plots showing relation of the P-value and $\log_2$ fold change enrichment of proteins in ATP13A1 KO1 cells stably re-expressing WT (left) or D533A (right) FLAG-tagged ATP13A1 relative to ATP13A1 KO1 cells. ATP13A1 (black dot) is the only protein whose expression is rescued in both WT and mutant rescue cells. Additional significant upregulated proteins are unique to re-expressing WT ATP13A1 and are predominantly mitochondrial (purple) or ER-targeted (green and blue) proteins. Proteins that also pass the significance threshold in Fig. 2F are bold. Colored dots correspond to the same classification as in Fig. 2F. In the context of our proposed function for P5A-ATPases, protein substrates will only be identified if they are (i) misinserted and require ATP13A1 function for correction and (ii) significantly destabilized without ATP13A. Considering the infrequency of mistakes during protein biosynthesis (e.g. targeting and topogenesis) and heterogeneity of potential downstream trafficking and degradative processes, additional P5A-ATPase-dependent proteins likely exist and remain to be identified.

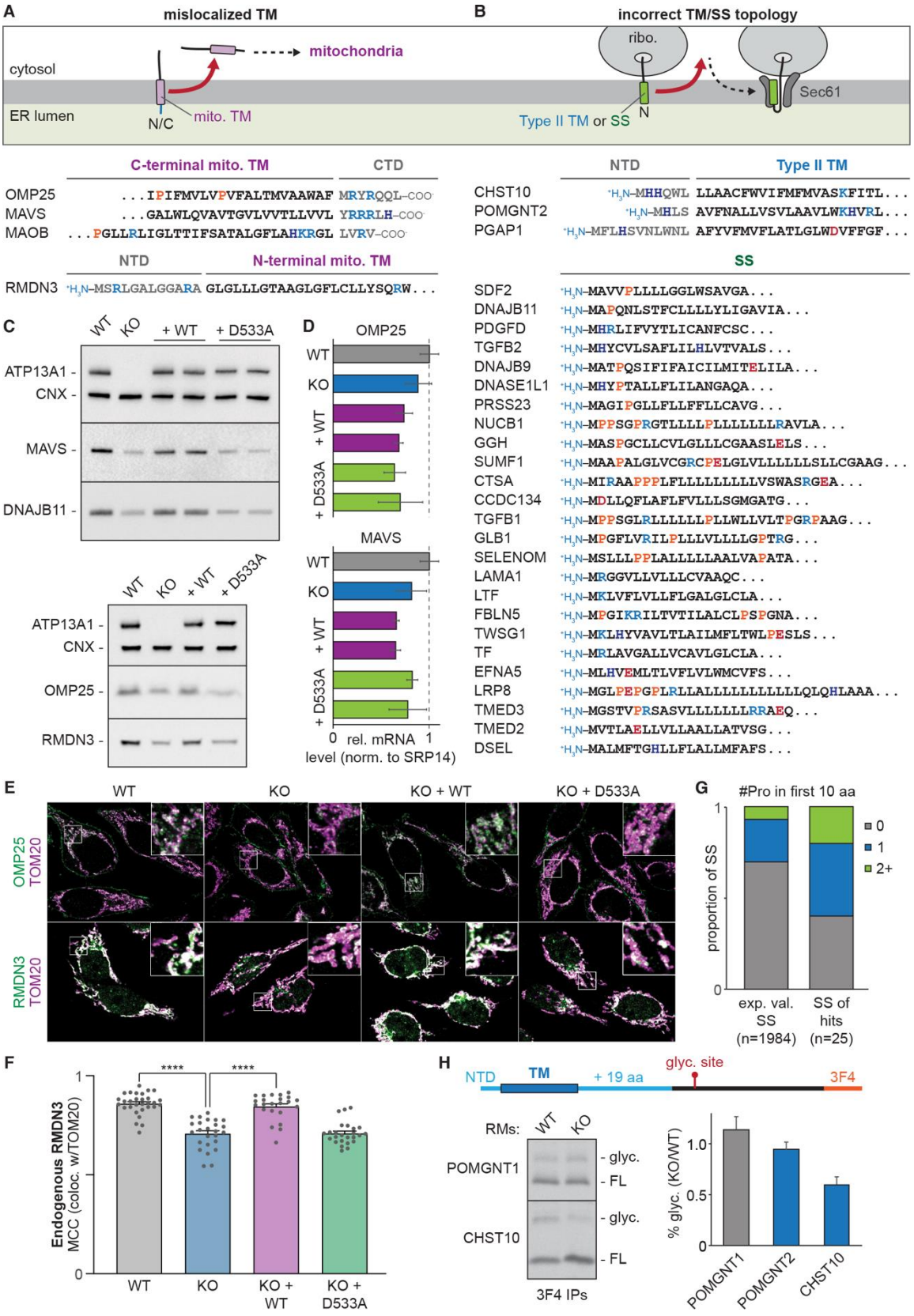

Fig. S10. ATP13A1-dependent proteins (see next page for caption).

Fig. S10. ATP13A1-dependent proteins.

(**A** and **B**) Proposed models for ATP13A1 dislocation (red arrow; top) and sequences (bottom) of protein candidates identified in Fig. 2F. ATP13A1 removes from the ER **(A)** mistargeted terminal mitochondrial (mito.) TMs and possibly **(B)** signal sequences (SS) and N-terminal type II TMs that insert in the wrong topology, which may provide additional opportunities for these hydrophobic helices to assume the correct N_{cyto}/C_{lumen} orientation at the Sec61 channel for productive protein translocation and topogenesis. CTD – C-terminal domain; NTD – N-terminal domain; SS – signal sequence. The positive charge of the N-terminus and helix dipole may contribute to P5A-ATPase recognition of putative clients with N-terminal hydrophobic helices. **(C)** Immunoblotting for the indicated proteins in wildtype (WT) and ATP13A1 knockout (KO) Flp-In T-REx HeLa cells without or with re-expression of WT or D533A FLAG-ATP13A1 behind the CMV*d*1 promoter as in fig. S9A. CNX – calnexin. **(D)** OMP25 and MAVS mRNA levels relative to SRP14 in the indicated cells normalized to WT cells. Shown are mean +/- s.d. for 3 replicates and 2 biological samples of rescue lines analyzed by quantitative real-time RT-PCR. Comparing these results with (C) and Fig. 2F show that changes in protein levels observed with ATP13A1 KO and rescue cells do not correlate with mRNA levels. ATP13A1 mRNA values are 1.0 +/- 0.06 (WT); 0.51 +/- 0.05 (KO); 0.9 +/- 0.06 and 0.86 +/- 0.08 (KO + WT); 0.75 +/- 0.05 and 0.79 +/- 0.19 (KO + D533A). **(E)** Immunofluorescence of endogenous OMP25 or RMDN3 (green) and TOM20 (purple) in the indicated cells. **(F)** Mean + s.e.m. and individual Manders' correlation coefficient (MCC) values of endogenous RMDN3 colocalization with TOM20 as in (D). **** $p<0.0001$. **(G)** Proportion of SS from an experimentally validated database or identified in Fig. 2F containing 0, 1, or 2 or more proline residues within the first 10 amino acids. ATP13A1-dependent SS appear enriched in prolines, which may influence topology. **(H)** *In vitro* insertion of type II TM reporters (top) containing the endogenous (blue) N-terminal domain (NTD), TM, and 19 amino acids of the indicated candidate followed by a glycosylation site (red) and a C-terminal 3F4 tag (orange). Insertion in the type II topology should result in glycosylation. Radiolabeled type II TM protein reporters were translated *in vitro* with WT or ATP13A1 KO rough microsomes (RMs). Denaturing immunoprecipitations (IPs) against the 3F4 tag and autoradiography show glycosylated (glyc.) and full-length (FL) populations (left). Mean + s.e.m of the ratio of glycosylated protein with KO vs. WT RMs are plotted for 3 independent experiments (right). POMGNT2 and CHST10 (blue) are significant hits in Fig. 2F. Increased glycosylation of the control protein POMGNT1 with ATP13A1 KO RMs is reproducible across multiple batches of RMs and awaits further investigation. Glycosylation of POMGNT2 and CHST10 is impaired by ATP13A1 KO, consistent with a dependence on ATP13A1 to efficiently achieve type II topology.

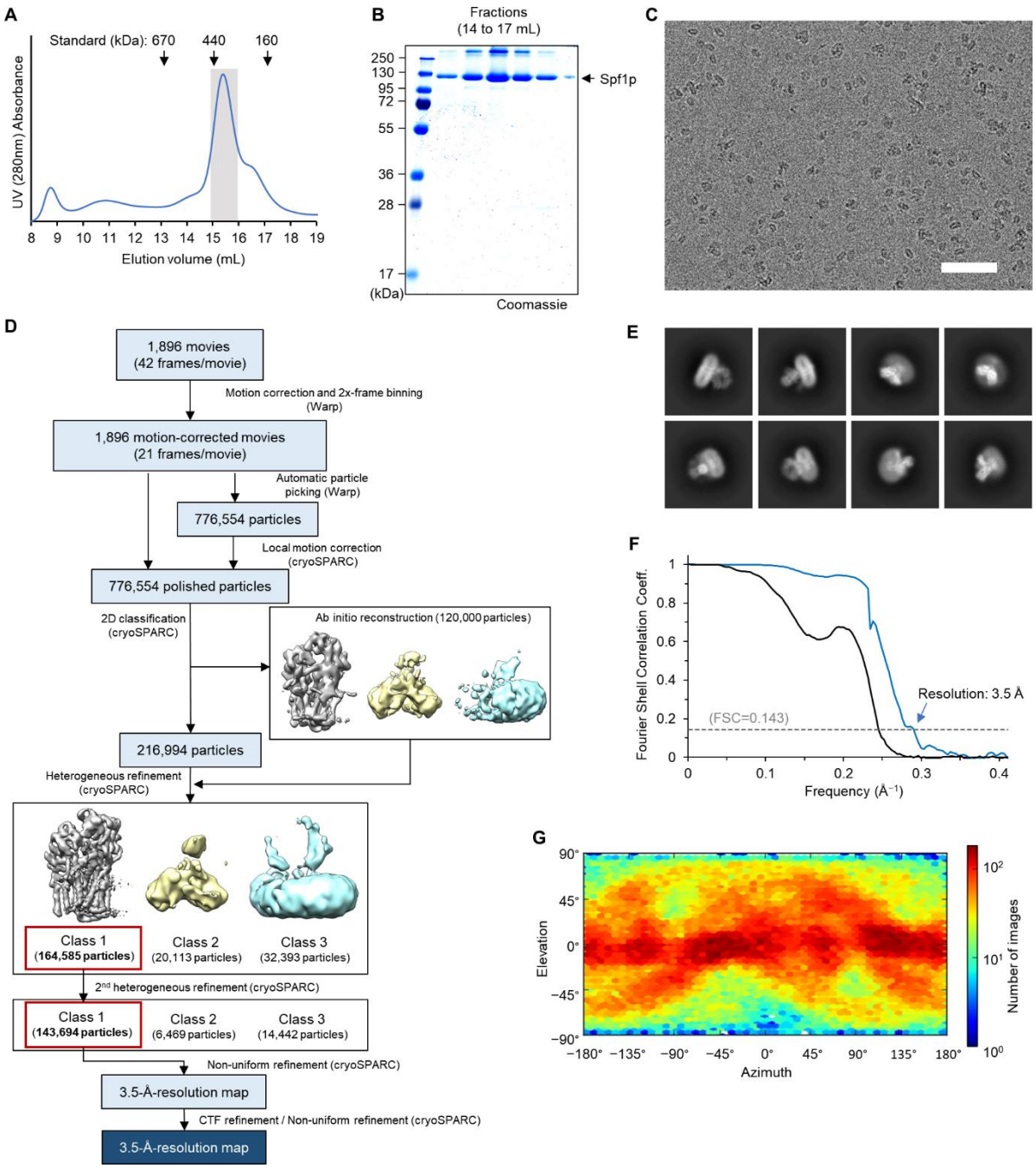

Fig. S11. Purification and cryo-EM analysis of *apo* Spf1 from *S. cerevisiae*.

(**A**) Superose 6 size-exclusion chromatography elusion profile of purified Spf1. The fractions marked with gray shade were used to prepare cryo-EM grids. (**B**) Coomassie-stained SDS gel of the Superose 6 fractions. (**C**) An example cryo-EM micrograph of *apo* Spf1. Scale bar, 50 nm. Only a quarter of the whole frame is shown. (**D**) A summary of the single particle image analysis procedure. (**E**) Selected 2D class averages. The box width is ~292 Å. (**F**) Fourier Shell Correlation (FSC) between the two half maps of the final 3D reconstruction. Black, with a spherical mask. Blue, with an automatic tight mask (noise-substitution corrected). (**G**) Distribution of particle orientations in the final 3D reconstruction.

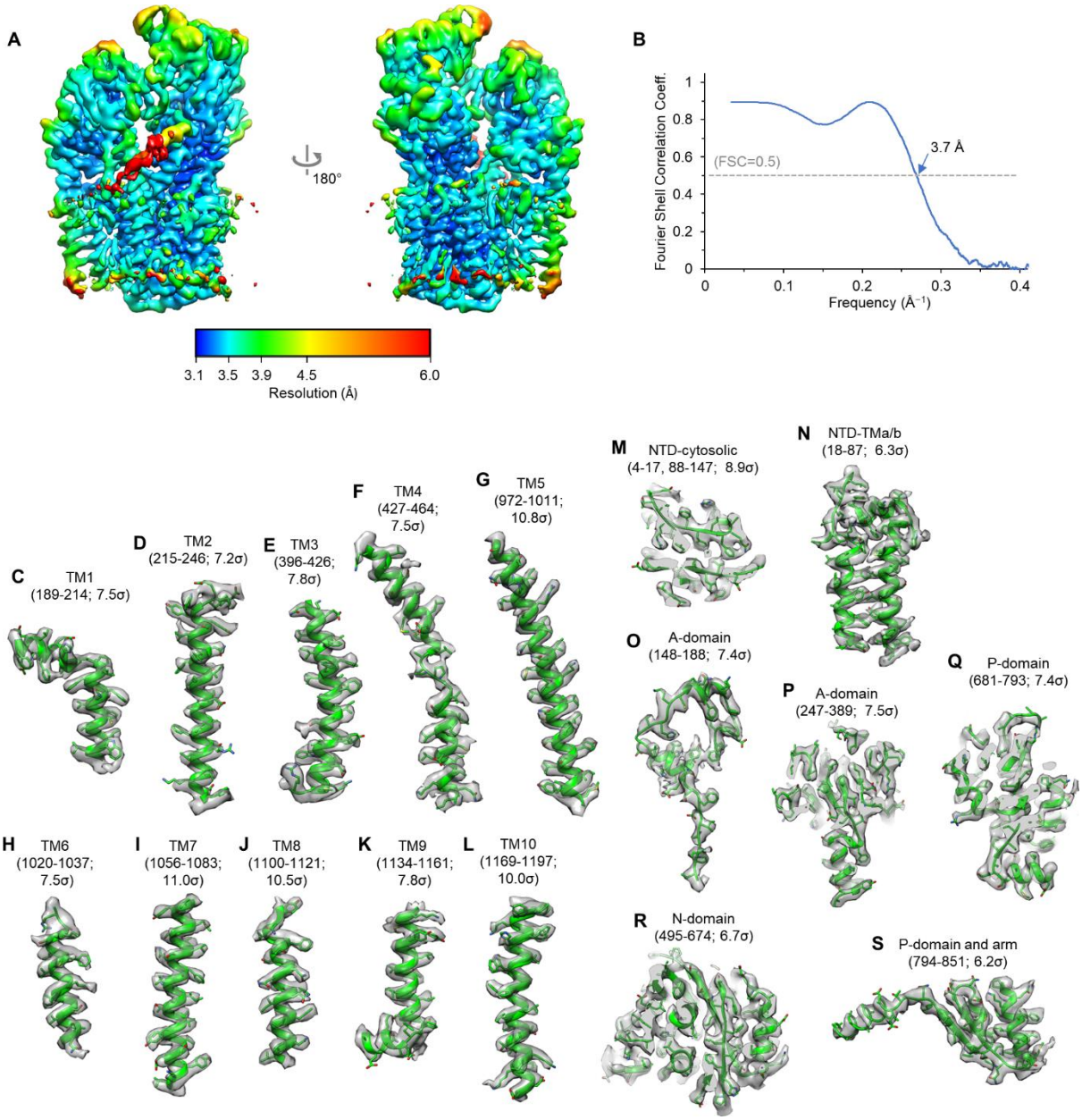

Fig. S12. Quality of the *apo* Spf1 cryo-EM map.

(**A**) Local resolution distribution indicated by a heat map. Left is a front view. Right is a back view. Shown is an unsharpened, lowpass-filtered (at 3.5 Å) map. (**B**) FSC between the unfiltered full map and atomic model. (**C**–**S**) Segmented EM densities and atomic model. Amino acid residue ranges and map contour levels (in sigma) are indicated. The panels M, P, Q, and R are cutaway views.

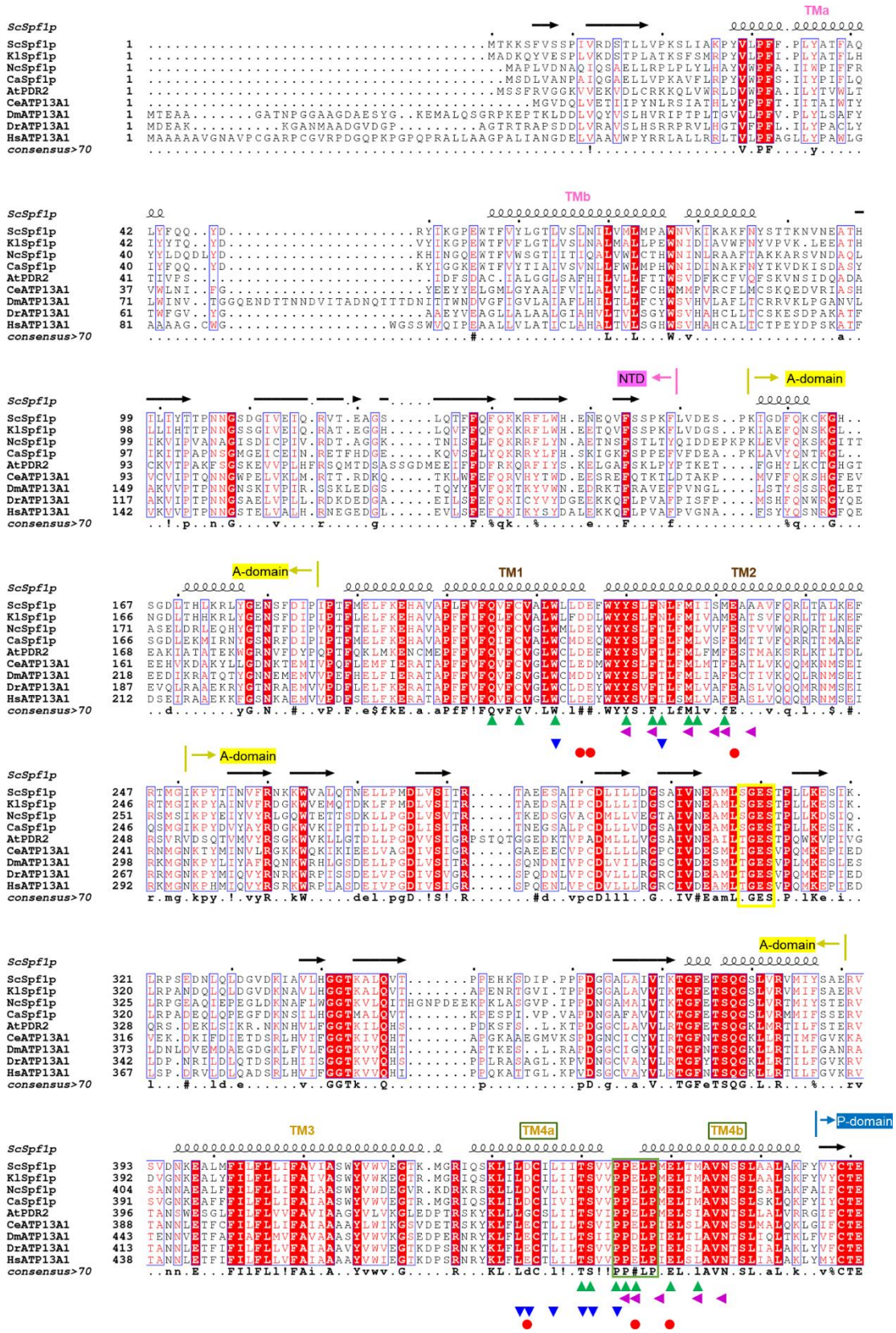

Fig. S13. Sequence alignment of Spf1/ATP13A1 (see next page for caption).

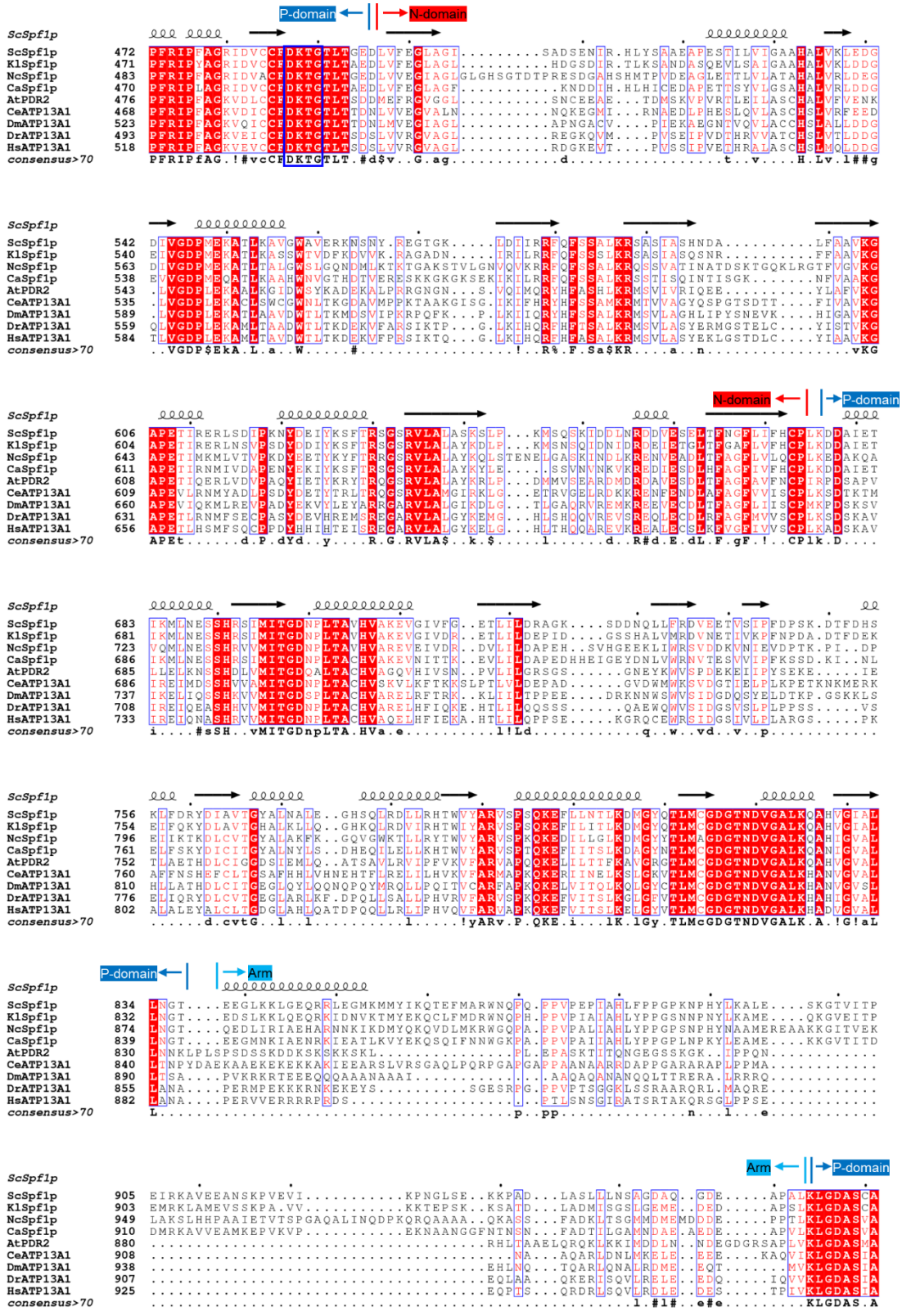

Fig. S13. Sequence alignment of Spf1/ATP13A1 (continued; see next page for caption).

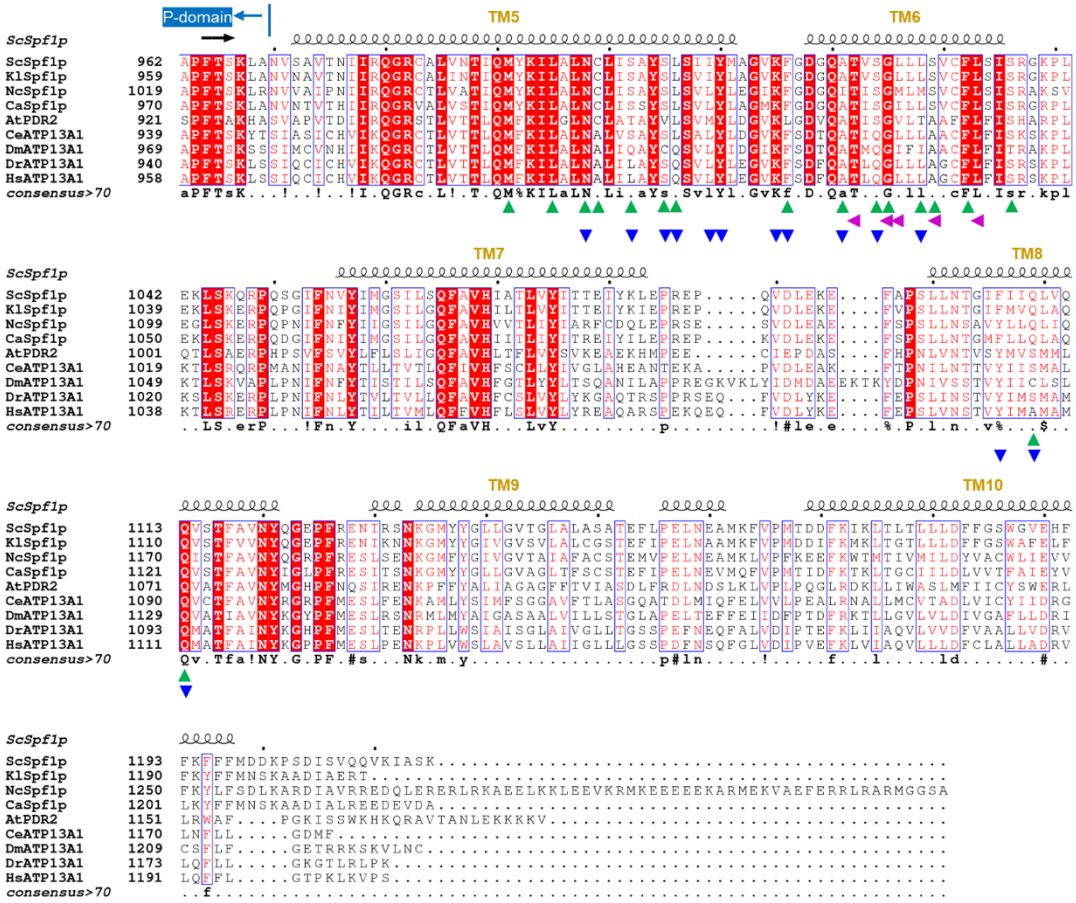

Fig. S13. Sequence alignment of Spf1/ATP13A1.

Sequence alignment of Spf1/ATP13A1 from selected species. Sc, *Saccharomyces cerevisiae* (UniProt accession number: P39986). Kl, *Kluyveromyces lactis* (Q6CM81). Nc, *Neurospora crassa* (Q7S1D7). Ca, *Candida albicans* (Q59Q34). At, *Arabidopsis thaliana* (Q9LT02), Ce, *Caenorhabditis elegans* (P90747). Dm, *Drosophila melanogaster* (Q9VKJ6). Dr, *Danio rerio* (F1R1X4). Hs, *Homo sapiens* (Q9HD20). Coils and black arrows, α-helices and β-stands based on the *Sc*Spf1 structure. Yellow box, the conserved (S/T)GES motif. Green box, the conserved PP(E/D)LP motif. Blue box, the conserved DKTG motif (phosphorylation site). Green and blue arrowheads, amino acids lining the substrate-binding pocket in the inward-open and outward-open conformation, respectively. Magenta arrowheads, amino acids interfacing with the substrate TM density. Red dots, acidic amino acids contributing to negative surface electrostatic potentials of the substrate-binding pockets (for the inward-open structures, D215, E232, D434, E446, and E450, and for the outward-open structures, D215, E216, D434, and E446; also see Fig 4C, figs. S15 C and D, and S16).

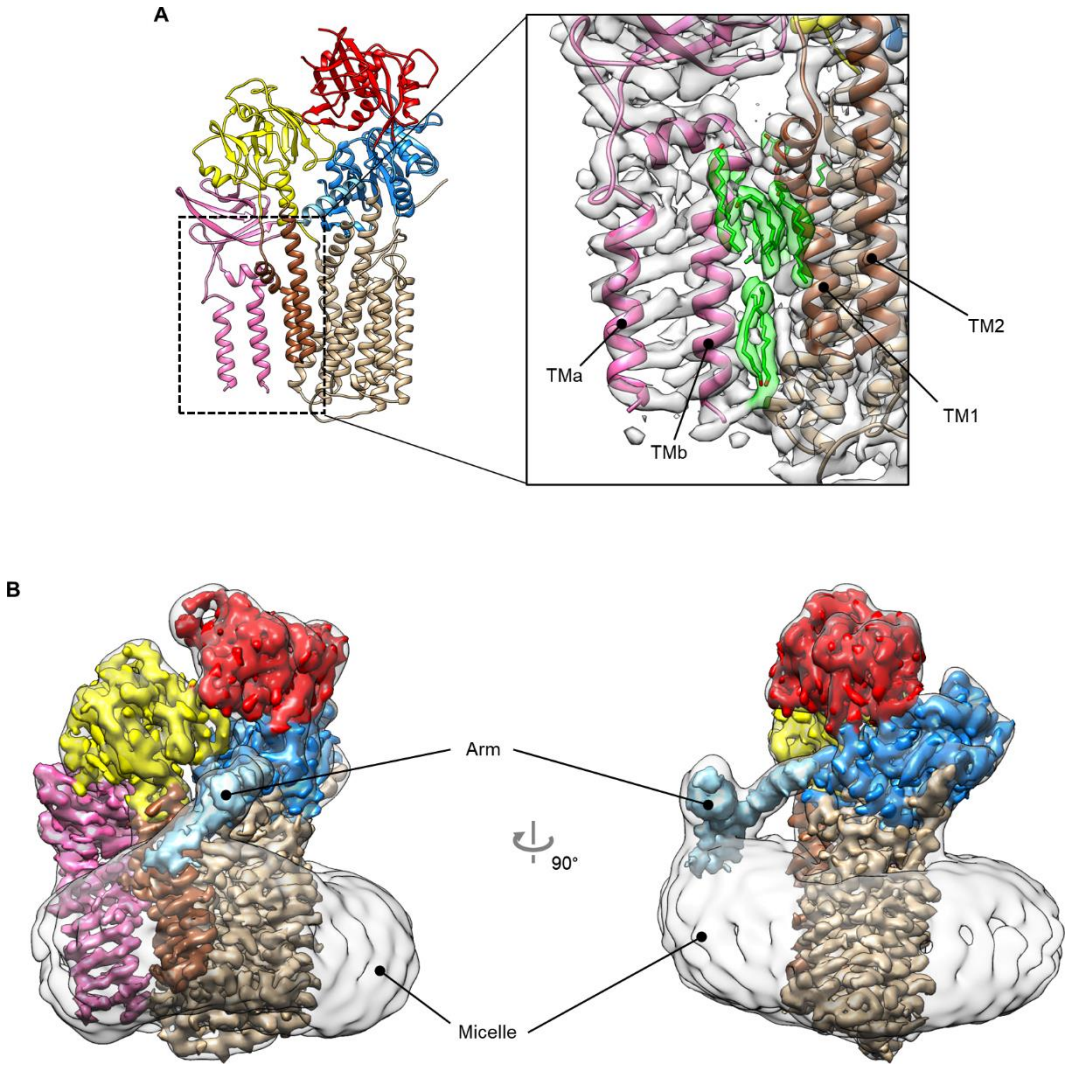

Fig. S14. N-terminal domain (NTD) and arm domain of Spf1.

(**A**) Detergent/lipid molecules in the interface of TMs a/b and TMs 1/2. Left panel is an overview (front view; as in Fig. 3B). Right panel is a close-up view into the interface between the NTD (magenta) and the T-domain (brown/tan). Densities and atomic models of aliphatic tails of detergent or lipid molecules are shown in green. (**B**) Interaction between the arm domain of Spf1 and the detergent micelle. As in Fig. 3A, but with an 8-Å-lowpass-filtered map (semi-transparent gray) to show the detergent micelle. The arm domain (light blue) is from a 5-Å-lowpass-filtered map. The color scheme is the same as in Fig. 3A. Left is a front view. Right is a side view. Note that in the region contacting the arm domain, the micelle is pulled upwards.

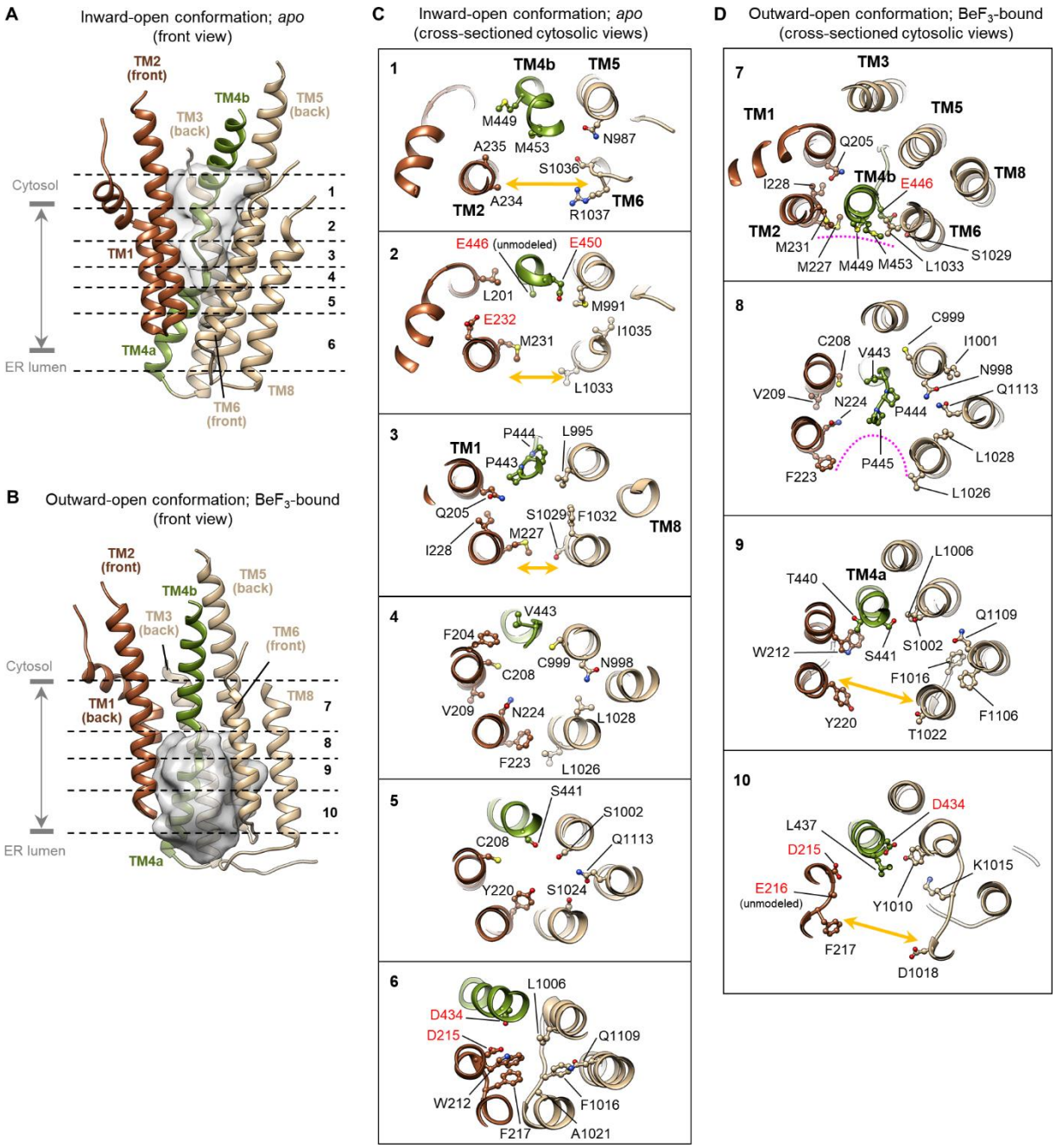

Fig. S15. The substrate-binding pocket of Spf1.

(**A**) The front view (left panel) of the inward-open substrate-binding pocket of Spf1 as in the left panel of Fig. 3D, but with TM8 additionally shown. Dashed lines indicate the boundaries of cross-sectioned views in C. (**B**) As in A, but with outward-open structure (BeF_3-bound structure; also see Fig. 4 and fig. S14). (**C**) Cross-sectioned views (from the cytosol) of the inward-open substrate-binding pocket of Spf1. The sidechains lining the cavity are shown in a ball-and-stick representation. The lateral opening to the membrane is indicated by orange arrows. Conserved acidic amino acids responsible for the negative electrostatic potential are indicated by red labels. (**D**) As in C, but with the outward-open structure. The magenta dotted line indicates the surface where the substrate TM binds based on the cryo-EM structure of substrate-bound Spf1.

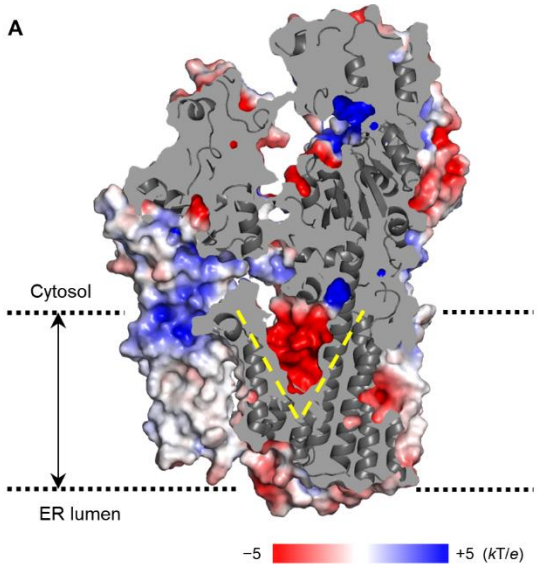

B

		D215, E216	E232	D434	E446, E450
P5A	*sc*Spf1	LWLL**DE**FWYY 220	MIISM**E**AAAVF 237	KLIL**D**CILIIT 440	VVPP**E**LPM**E**LTM 453
	*hs*ATP13A1	LWCL**DE**YWYY 265	MLVAF**E**ASLVQ 282	KLFL**E**CTLILT 480	VVPP**E**LPI**E**LSL 499
P5B	*hs*ATP13A2	LWLA**D**HYYWY 259	ISSISICLSLY 276	EIVIRALDLVT 466	VVPPALPAAMTV 479
	*hs*ATP13A3	LWST**DE**YYYY 234	MSIVSIVSSLY 251	VIII**E**SLDIIT 451	TVPPALPAAMTA 464
	*hs*ATP13A4	LWFS**ED**YKEY 225	MSIISISLTVY 242	EVVRKALDVIT 439	AVPPALPAALTT 452
	*hs*ATP13A5	LWLSQGYIEY 226	LTVISIVLSVY 243	DTVTMALILLT 439	TVPPVLPAALTI 452

Fig. S16. Electrostatic properties of the substrate-binding pocket of Spf1.

(**A**) Surface electrostatic of the *apo* (inward-open) Spf1 structure. Shown is a cut-away view (front view). The V-shaped cavity is indicated by yellow dashed lines. For the outward-open structure, see Fig. 3C. (**B**) Sequence alignment of regions containing acidic amino acids (in bold) that are responsible for negative electrostatic potentials of the Spf1 substrate-binding pockets. Only P5-ATPases are shown because the other P-type ATPase subfamilies display low sequence similarity in these regions. Gray highlights, positions with >50% sequence identity.

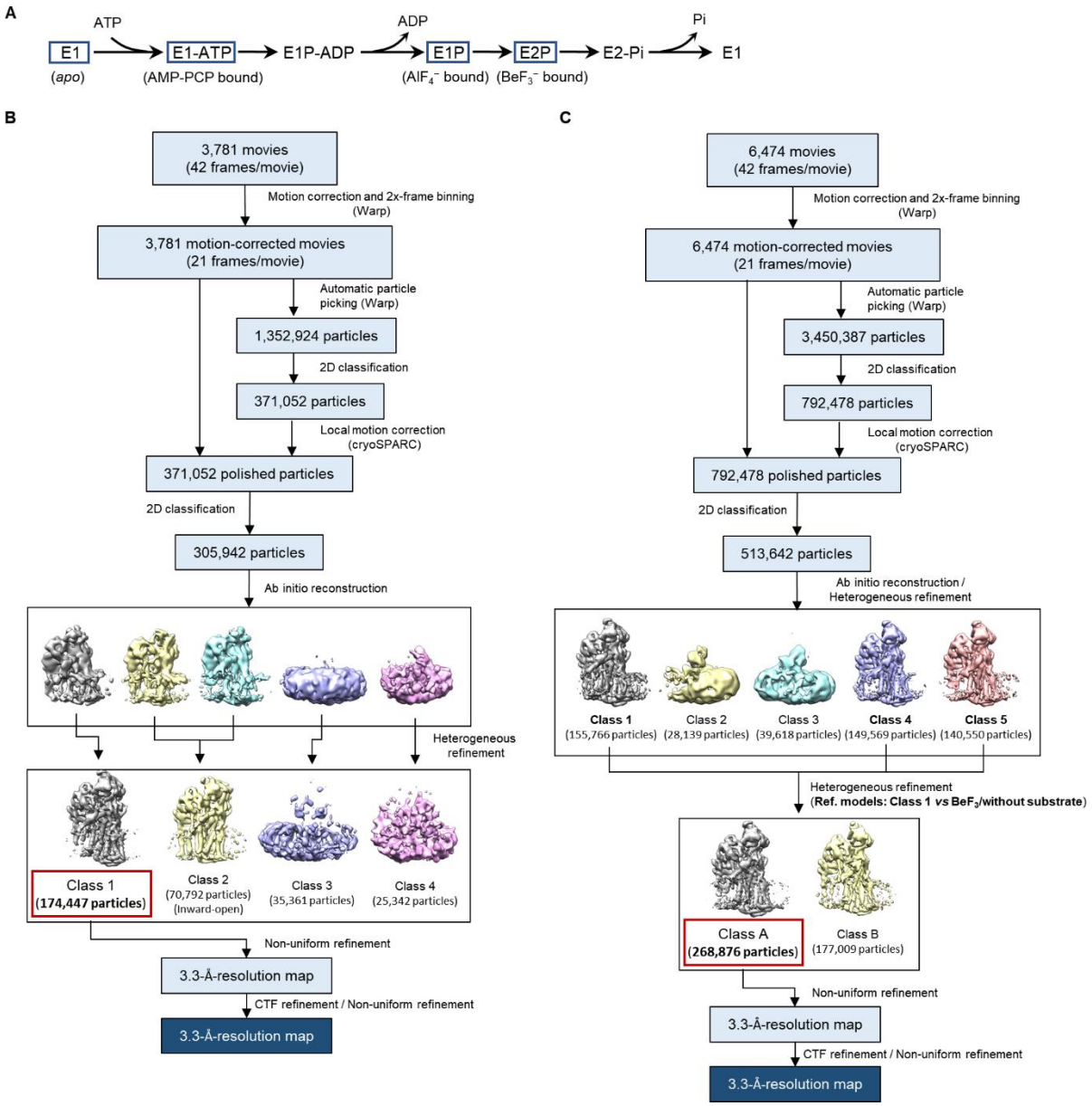

Fig. S17. Cryo-EM analysis of Spf1 complexed with nucleotide/phosphate analogs.

(**A**) Scheme of the Post-Albers cycle. Structures of the states in blue boxes were determined in this study. (**B** and **C**) Summaries of single particle analysis procedures used for BeF_3-bound (B) or BeF_3- and endogenous substrate-bound Spf1 (C).

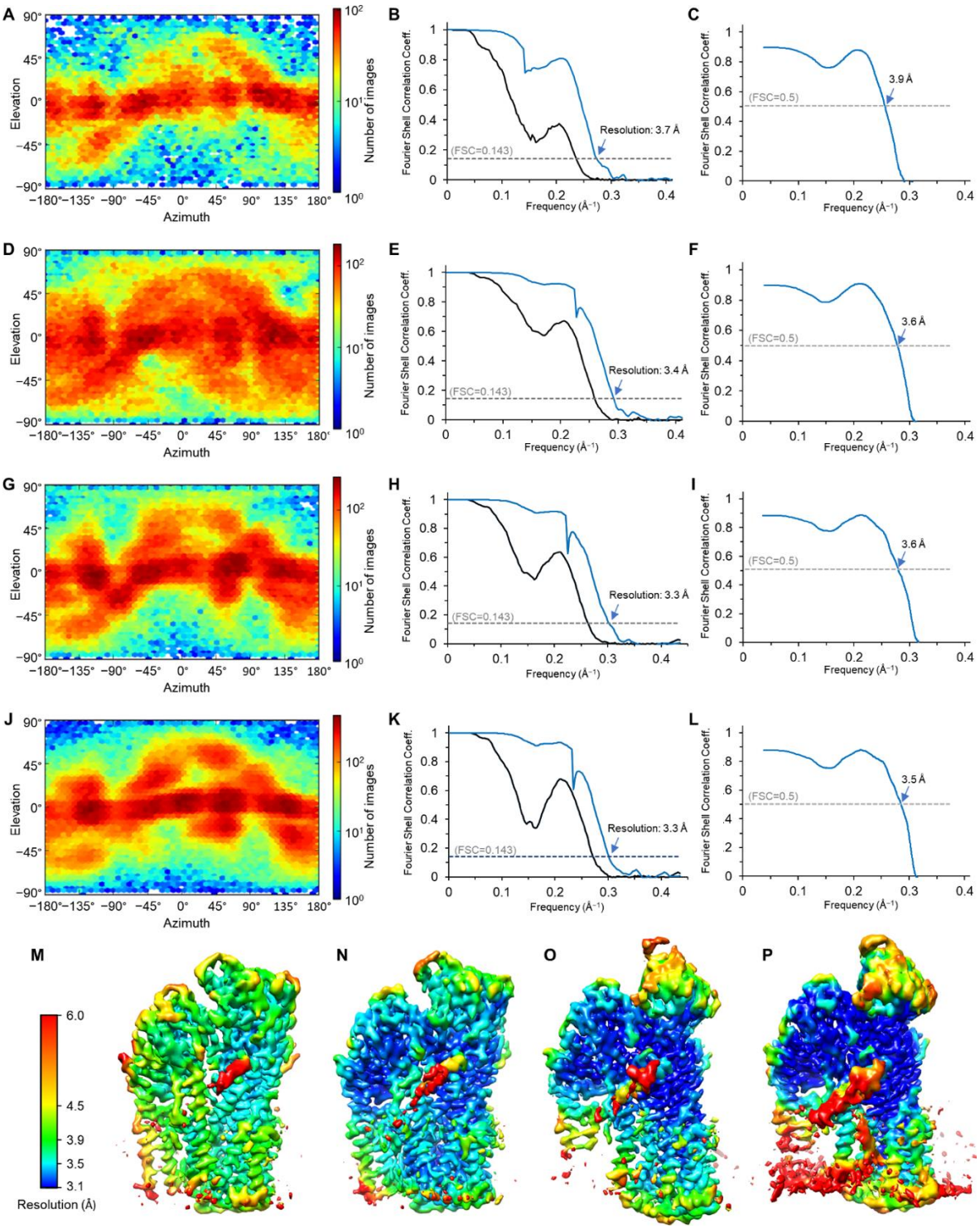

Fig. S18. Cryo-EM reconstruction statistics for nucleotide/phosphate analog-bound Spf1.

(**A–C**) Particle view orientation distribution (A), half-map FSC (B; blue, tight mask; black spherical mask), and masked map-model FSC (C) for AMP-PCP-bound Spf1. (**D**–**L**), As in A–C, but for Spf1 bound to AlF_4^- (D–F), BeF_3^- (G–I), and BeF_3^-/endogenous substrate (J–L). (**M**–**P**) Local resolution distributions of Spf1 reconstructions (shown with unsharpened, lowpass-filtered maps). (M) AMP-PCP-bound. (N) AlF_4-bound. (O) BeF_3-bound. (P) BeF_3- and endogenous substrate-bound.

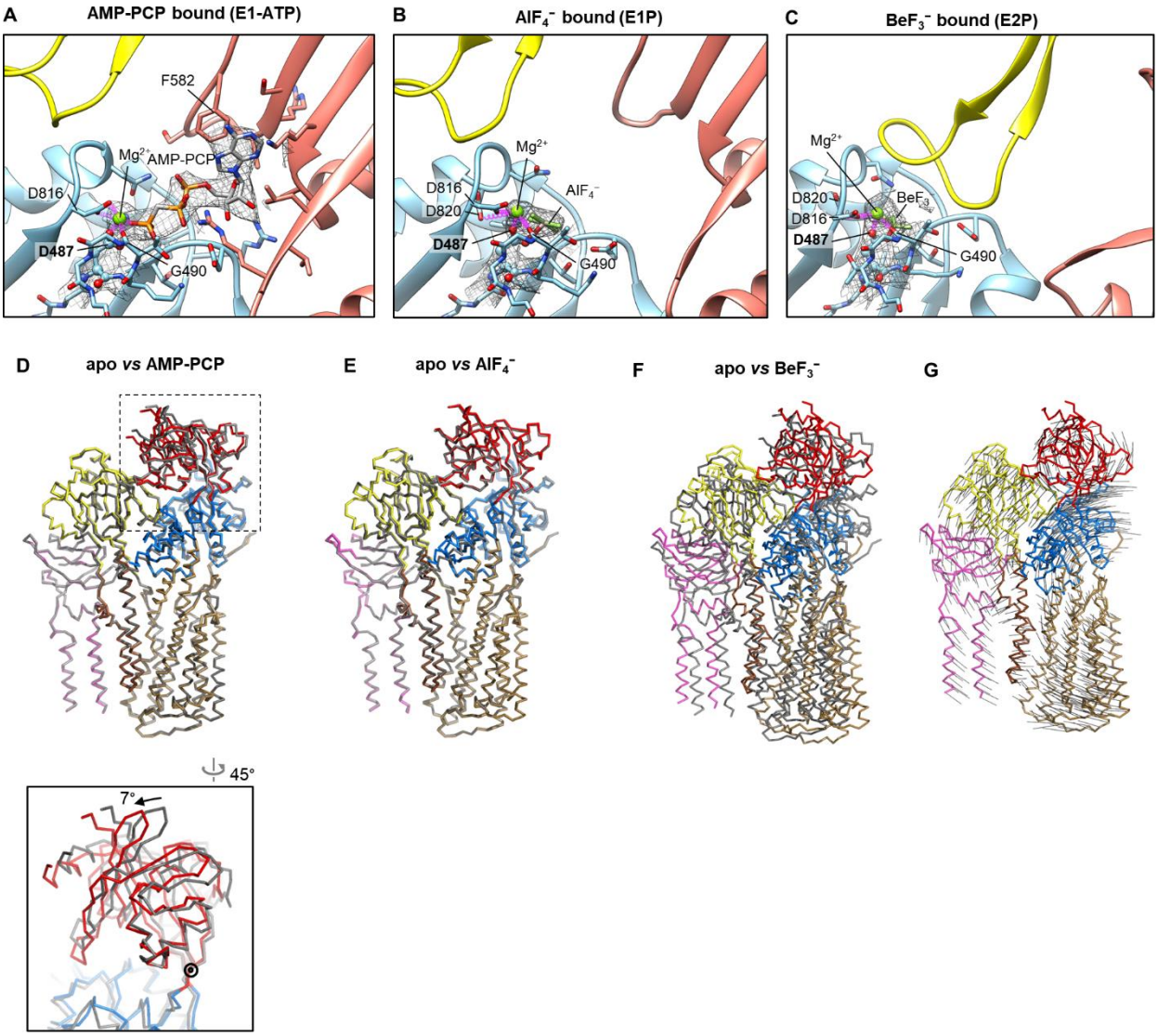

Fig. S19. Structures of Spf1 complexed with AMP-PCP, AlF_4^-, or BeF_3^-.

(**A**–**B**) Structures of the phosphorylation site of Spf1 bound to AMP-PCP (A), AlF_4^- (B), and BeF_3^- (C). Cryo-EM density of the bound ligands (including Mg^{2+}) and phosphorylation site (Asp^{487} of the DKTG motif and neighboring amino acids) are shown in mesh. Nonbonded interactions between the ligands and amino acids are indicated in magenta. Yellow, A-domain (SGES loop). Light blue, P-domain. Salmon, N-domain. (**D**) Structural comparison between *apo* Spf1 (gray) and Spf1 bound to AMP-PCP (in colors; the same color scheme as in Fig. 3). The area indicated with a dashed box is magnified in the lower panel to show rigid-body rotational motion of the N domain (the rotational center is indicated by a circle). (**E** and **F**) As in D, but comparisons between *apo* Spf1 and Spf1 bound to AlF_4^- (E) and BeF_3^- (F). (**G**) As in F, but showing the displacement of Cα (gray lines) atoms from the *apo* to BeF_3^- structures (the *apo* structure is not shown). Front views are shown.

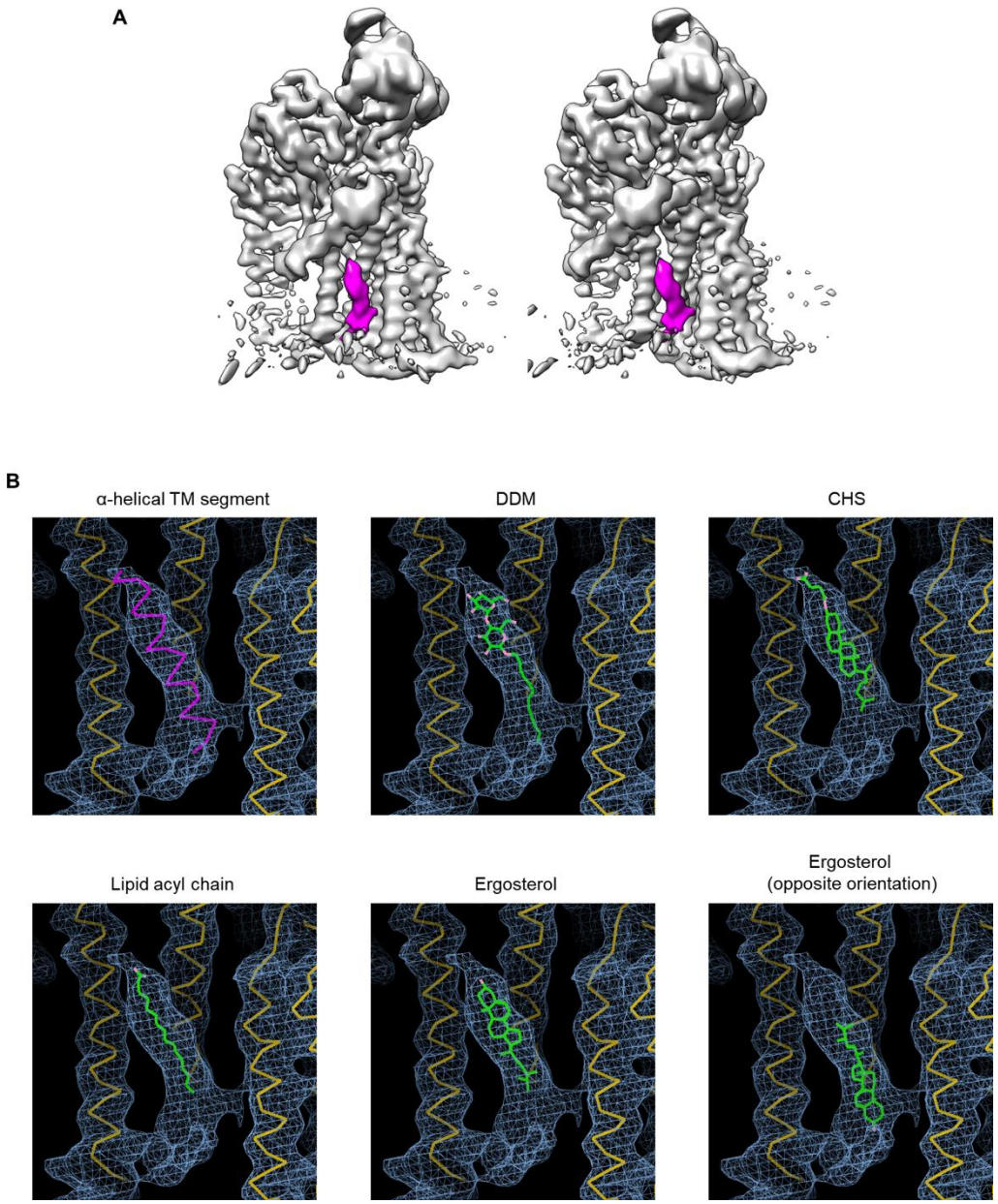

Fig. S20. The cryo-EM density of a putative substrate bound to the outward-open substrate pocket. (A) Stereo view of the uncropped cryo-EM map (at 7.4σ contour level) of the substrate-bound Spf1 (lowpass-filtered at 5 Å). The substrate density is in magenta. (B) The dimensions of the substrate density, 20-residue-long α-helical TM segment (magenta Cα trace), detergents, and lipids were compared by docking of the molecules into the density. The map was lowpass-filtered at 5 Å and shown at 7.3σ contour level. The Cα trace of Spf1 is shown in yellow. Palmitic acid (lower left panel) was used as an example of a lipid acyl chain. DDM, dodecyl maltoside. CHS, cholesteryl hemisuccinate.

Table S1. Cryo-EM data collection, refinement, and validation statistics

	Apo Spf1 (EMDB-22260) (PDB 6XMP)	AMP-PCP-bound (EMDB-22261) (PDB 6XMQ)	AlF_4-bound (EMDB-22262) (PDB 6XMS)	BeF_3-bound (EMDB-22263) (PDB 6XMT)	BeF_3/substrate-bound (EMDB-22264) (PDB 6XMU)
Data collection and processing					
Microscope	Arctica	Krios	Arctica	Krios	Krios
Detector	K3	GIF/K3	K3	GIF/K3	GIF/K3
Magnification					
Nominal	36,000x	64,000x	45,000x	64,000x	64,000x
Calibrated	43,856x	42,017x	55,556x	42,017x	42,017x
Voltage (kV)	200kV	300kV	200kV	300kV	300kV
Pixel size (Å)	1.14	1.19	0.90	1.19	1.19
Electron exposure (e–/Å^2)	50.0	49.1	63.0	49.1	49.1
Exposure rate (e/Å^2/sec)	9.16	10.6	15.3	10.6	10.6
Number of frames collected	42	42	42	42	42
Energy filter slit width (eV)	N/A	20	N/A	20	20
Defocus range (μm)	-0.8 to -2.8	-0.8 to -2.4	-0.7 to -2.0	-0.9 to -2.3	-0.8 to -2.5
Automation software	SerialEM	SerialEM	SerialEM	SerialEM	SerialEM
Micrographs used (no.)	1,896	1,420	2,234	3,781	6,474
Symmetry imposed	None (C1)	None (C1)	None (C1)	None (C1)	None (C1)
Initial particle images (no.)	776,554	454,468	470,200	1,352,924	3,450,387
Final particle images (no.)	143,694	55,920	144,878	174,447	268,876
Map resolution (Å)					
Unmasked (0.5 FSC)	7.4	9.4	7.5	8.1	8.1
Unmasked (0.143 FSC)	4.3	6.7	4.1	4.1	3.9
Masked (0.5 FSC)	4.0	4.1	3.8	3.7	3.7
Masked (0.143 FSC)	3.5	3.7	3.4	3.3	3.3
Local resolution range (Å)	3.1–13	3.2–17	3.0–12	2.9–15	2.8–15
Refinement					
Initial model used	*De novo*	*Apo* Spf1	*Apo* Spf1	*Apo* Spf1	BeF_3 Spf1
Refinement software	Phenix 1.16 (real_space_refine)	Phenix 1.16 (real_space_refine)	Phenix 1.16 (real_space_refine)	Phenix 1.16 (real_space_refine)	Phenix 1.16 (real_space_refine)
Model-to-map correlation					
CC(mask)	0.83	0.85	0.87	0.82	0.83
CC(main chain)	0.84	0.85	0.87	0.83	0.83
CC(side chain)	0.81	0.84	0.85	0.82	0.83
Model resolution (Å)	3.7	3.9	3.6	3.6	3.5
FSC threshold	0.5	0.5	0.5	0.5	0.5
Map sharpening *B* factor (Å^2)	-116.6	-61.3	-80.7	-79.3	-79.1
Model composition					
Non-hydrogen atoms	8,868	8,364	8,391	8,328	8,414
Protein residues	1,086	1,085	1,091	1,092	1,110
Ligands	12 (DDM)	2 (AMP-PCP, Mg^{2+})	2 (AlF_4^-, Mg^{2+})	2 (BeF_3^-, Mg^{2+})	2 (BeF_3^-, Mg^{2+})
Average B factors (Å^2)					
Protein	64	88	71	32	60
Ligands	51	65	55	10	26
R.m.s. deviations					
Bond lengths (Å)	0.005	0.004	0.006	0.003	0.003
Bond angles (°)	0.54	0.58	0.66	0.58	0.55
Ramachandran plot					
Favored (%)	97.03	96.29	95.30	95.38	95.81
Allowed (%)	2.96	3.71	4.70	4.53	4.19
Disallowed (%)	0.0	0.0	0.0	0.09	0.0
Validation					
MolProbity score	1.54	1.59	1.67	1.73	1.64
Clash score	6.71	6.14	6.18	7.36	6.33
Poor rotamers (%)	0.0	0.0	0.0	0.0	0.0
C-beta outlier (%)	0.0	0.0	0.0	0.0	0.0
CaBLAM outlier (%)	2.06	2.15	1.77	2.24	2.67
EMRinger score	1.55	1.28	1.86	2.40	2.22

Movie S1. Cryo-EM structure of apo Spf1.

This movie sequentially shows the cryo-EM reconstruction (density map) and atomic model (ribbon representation) of apo Spf1. The domains are colored as in Fig. 3. The putative substrate-binding pocket in the membrane domain is indicated by a yellow dashed line. The ATP-binding/phosphorylation site (empty in this structure) is indicated by a green dashed circle.

Movie S2. Cryo-EM structure of BeF_3-bound Spf1.

As in Movie S1, but with the structure of BeF_3-bound Spf1. We note that parts of TMa and TMb were not well visualized in the cryo-EM map because of conformational flexibility in this region. These regions were modeled as polyalanine helices based on the apo structure.

Movie S3. Conformational transition (morph) between the AlF_4-bound (E1P) and BeF_3-bound (E2P) state.

The structures of AlF_4-bound and BeF_3-bound Spf1 were aligned, and a morph was generated using PyMol. The movie sequentially shows the conformational transitions in ribbon and surface representations.

Data S1. TMT-MS data of UV-enriched interactions with mitochondrial TA(Bpa).

TMT-MS data values of 6 replicates each of reactions of recombinant TA(Bpa) with mitochondria-enriched yeast membrane fractions without and with UV irradiation (related to Fig. 1C)

Data S2. TMT-MS data of putative ATP13A1 clients.

TMT-MS data values of proteomic analysis of 3 replicates each of lysates isolated wildtype (WT), two ATP13A1 knockout (KO), and KO Flp-In T-Rex HeLa cells stably re-expressing WT or D533A FLAG-tagged ATP13A1 (related to Fig. 2F and fig. S9 and S10).